

Acta Technologica Agriculturae 2
Nitra, Slovaca Universitas Agriculturae Nitriae, 2020, pp. 53–59

EVALUATION OF CO AND NO_x EMISSIONS IN REAL-LIFE OPERATING CONDITIONS OF HERBACEOUS BIOMASS BRIQUETTES COMBUSTION

Jan MALAŤÁK^{1*}, Jan VELEBIL¹, Jiří BRADNA¹, Arkadiusz GENDEK², Barbora TAMELOVÁ¹

¹Czech University of Life Sciences Prague, Czech Republic

²Warsaw University of Life Sciences – SGGW, Warsaw, Poland

The issue of carbon monoxide and nitrogen oxides emissions into the atmosphere is very current. This article thus focuses on the assessment of elemental composition of selected herbal biomass species and emission concentrations during combustion in a commonly available grate combustion device for briquetted fuel. In tests, emission concentrations were evaluated in contrast to the oxygen concentration in flue gas and flue gas temperatures. Samples of camelina (*Camelina sativa*), giant miscanthus (*Miscanthus giganteus*), reed canary grass (*Phalaris arundinacea* L.) and sorghum (*Sorghum bicolor*) were used. Elementary and stoichiometric combustion analyses were conducted for these samples (LECO AC-600 semi-automatic calorimeter, CHN628 + S elemental analyser and LECO TGA-701 analyser). Analyses of C, H, N and S concentrations and calorific values showed that samples of briquetted herb biomass had insignificant differences and could be used for energy purposes without limitation. The limiting factor was the high amount of ash, which amounted to 6.59% of dry weight in reed canary grass briquette sample. Furthermore, a high percentage (1.91% wt.) of nitrogen was observed in reed canary grass briquettes. Such a high amount of nitrogen during combustion tests resulted in an increase in NO_x emission levels in flue gas of the *Phalaris arundinacea* L. sample, in which it reached the maximum concentration of 375.20 mg·m⁻³. The combustion tests showed that even under steady-state conditions, high concentrations of carbon monoxide could not be avoided for tested briquetted biofuels without active regulation of the combustion process.

Keywords: calorific value; elementary analysis; stoichiometry; coefficient of excess air; flue gas

Reduction of impacts of fossil fuel combustion includes their replacement by renewable energy sources. Particularly, it is wood or herbaceous biomass in the field of solid fuels (Oberberger et al., 2006; Dhaundiyal and Hanon, 2018). Especially for wood, further modifications are made to obtain more valuable materials, not only for energy purposes (Kučerová et al., 2016; Kučerová and Výbohová, 2018). Considering the herbaceous biomass, which does not offer as wide a possibility of treatment as wood, it is primarily direct combustion (Brunerová et al., 2017; Malaták et al., 2017). Biomass of plant origin contains a significant energy potential that varies with plant physiology (Hnilička et al., 2015). Impacts of the renewable energy fuel utilization lead to environmental improvements (Esteban et al., 2014).

When assessing the quality of the combustion process, the first indicators are the levels of carbon oxides in the flue gas (Bradna and Malaták, 2016). The maximum CO₂ concentrations are achieved at low coefficients of excess air (Johansson et al., 2004) together with the highest combustion temperature (Malaták et al., 2017). At the same time, other components of flue gas, such as sulphur and nitrogen oxides, must be taken into consideration. Their concentrations are always higher in herbaceous biomass than in wood (Brassard et al., 2014). Production of nitrogen oxides is dependent on combustion temperatures and the

amount of incoming combustion air (Díaz-Ramírez et al., 2014). Garcia-Maraver et al. (2014) confirmed the effects of higher nitrogen content in the fuel on increased emission concentrations.

Emissions production is influenced not only by the type of fuel (Zosima and Ochsenkiihn-Petropoulou, 2015) but also by the type of combustion technology (Malaták and Passian, 2011; Win et al., 2012). Above all, discontinuous fuel supply leads to increased concentrations of carbon monoxide and nitrogen oxides in comparison to continuous fuel supply (Juszczak, 2016).

In this paper, four herbaceous biomass fuels have been tested with a hypothesis that increasing the excess of combustion air would lead to a significant reduction in nitrogen oxide emissions caused by simultaneous decrease in flue gas temperatures. However, at the same time, carbon monoxide emissions have been expected to increase in volume. To test this hypothesis, samples were combusted under typical operating conditions of a grate fired combustion device while measuring the emission concentrations of nitrogen oxides and carbon monoxide; the flue gas temperature; and the coefficient of excess air. These measurements were supplemented by analyses of proximate and elemental compositions, as well as calorific values.

Contact address: Jan Malaták, Czech University of Life Sciences Prague, Faculty of Engineering, Department of Technological Equipment of Buildings, Kamýčká 129, 165 21 Prague, Czech Republic, e-mail: malatak@tf.czu.cz

Material and methods

Biomass materials

Four herbaceous biomass samples were selected. These were camelina straw (*Camelina sativa*, CS); giant miscanthus (*Miscanthus giganteus*, MG); reed canary grass (*Phalaris arundinacea* L., PA); and sorghum (*Sorghum bicolor*, SB).

CS, once grown over large areas in Europe, is an undemanding crop with a short growing season and no need for high-tech agricultural machinery. It grows well in most soils (Eynck and Falk, 2013). At 8% wt. moisture content, the net calorific value of straw is approx. 15.1 MJ·kg⁻¹. The sample came from a 2018 harvest.

MG is one of major energy crops. This plant, which requires favourable soil and climatic conditions, can show high yields of up to 28.19 t·ha⁻¹ of dry matter in the Czech Republic (Stražil, 1999). The harvest was carried out in 2018 in March and April.

PA is a plant native to the Czech Republic with an average yield of 10 t·ha⁻¹. Samples from the 2018 spring harvest were used. Spring harvest is recommended because the potassium, chlorine, nitrogen and sulphur contents tend to decrease during later harvests in contrast to early harvest dates (Platace et al., 2013).

SB is one of many energy crops grown in the Czech Republic. Usually, it is used as a substitute for maize (Amon et al., 2007). In the Czech Republic, the average yield is 16 t·ha⁻¹ of dry matter. Since SB is harvested only once a year, samples were collected in 2018.

Fuel analysis

Elemental analysis to determine the percentage of combustible matter components, such as carbon (C), hydrogen (H), nitrogen (N) and sulphur (S), were conducted nine times for each sample. A LECO CHN628 + S elemental analyser was used for this purpose. The detection method for C, H, S was infrared absorption; thermal conductivity cell was utilized to determine the N content.

LECO TGA-701 thermogravimetric analyser was used to determine the percentages of non-flammable substances, i.e. ash and total moisture content. Here, the measurements were repeated six times for each sample with an accuracy of ±0.02%. Another measured parameter was the gross calorific value. It was determined by combustion utilizing the isoperibol calorimeter LECO AC-600 in accordance with the DIN 14918 (2010). The net calorific value was specified via calculation utilizing the results of elemental and proximal analyses of individual samples. This relationship between gross calorific value Q_g (kJ·kg⁻¹) and net calorific value Q_n (kJ·kg⁻¹) is as follows:

$$Q_n = Q_g - (0.02442 \cdot 1,000) \cdot (W + 8.94 \cdot H) \quad (1)$$

where:

- W – water content in test sample (% wt.)
- 8.94 – coefficient for the conversion of hydrogen to water
- H – hydrogen content in test sample (% wt.)
- 0.02442 – value that corresponds to energy consumed in heating of 1% of water at 25 °C

Stoichiometric combustion calculations add to the characterisation of the samples. This was mainly the determination of the theoretical amount of combustion air; theoretical amount of dry flue gas; and theoretical concentration of carbon dioxide in dry flue gases. The method of calculation has been described by Malaťák et al. (2016). Stoichiometric calculations are necessary to compare the theoretical and actual combustion process. They exploit the results of the previous analyses. The results of the stoichiometric calculations were used to set the sample characteristics in the flue gas analyser, as well as to determine the excess air coefficient, which can be calculated as follows:

$$n = 1 + \left(\frac{CO_{2,max}}{CO_2} - 1 \right) \cdot \frac{V_{sp,min}}{L_{min}} \quad (2)$$

where:

- $CO_{2,max}$ – theoretical volumetric concentration of carbon dioxide in dry flue gases (% vol.)
- CO_2 – volumetric concentration of carbon dioxide in dry flue gases (% vol.)
- $V_{sp,min}$ – theoretical mass amount of dry flue gas (m³·kg⁻¹)
- L_{min} – theoretical amount of air for complete combustion (m³·kg⁻¹)

Combustion tests

Emission concentrations were measured using a combustion device with a fixed combustion grate with a manual fuel supply CALOR (WAMSLER, Ismaning, Germany). Similar devices are commonly used for household heating. This combustion plant was also selected for the ability to achieve a large range of operating conditions. The device nominal heat output is 12 kW and the standard fuel consumption is 3.5 kg·h⁻¹. During the combustion tests, mass flows of the samples into the combustion plant were recorded to maintain the rated thermal output. Throughout the combustion process, the nominal heat output was maintained for the combustion plant at 12 kW with an efficiency of 80%. The corresponding hourly input of briquetted samples was 3.45 kg·h⁻¹ for CS; 3.42 kg·h⁻¹ for MG; 3.54 kg·h⁻¹ for PA; and 3.62 kg·h⁻¹ for SB. For each fuel sample, combustion tests lasted for 6 hours and the fuel dosing interval was set to 30 minutes. The experimental data were acquired under stable combustion conditions at intervals of 15 minutes and each data point was averaged by the analyser values over one minute. Throughout the combustion process, the primary combustion air supply was controlled. This was monitored by the oxygen concentration in the flue gas.

The emission concentrations were measured using a Madur GA-60 flue gas analyser. During the measurements, the analyser monitored the ambient temperature; flue gas temperature; and concentrations of O₂, CO, NO and NO₂ in the flue gas. Before the measurement of each sample, the analyser was calibrated. The signals of the transducers were proportional to the volumetric concentration of the measured components in ppm. The concentrations of dry flue gas components were converted to normal conditions and concentrations in mg·m⁻³ at the reference oxygen

content of 13% in the flue gases. The results of emission measurements were processed utilizing the regression analysis in order to convey the dependence of carbon dioxide and nitrogen oxides on the coefficient of excess air and the flue gas temperature.

Results and discussion

The elemental analysis of all samples is shown in Table 1. The results are given both at the original moisture content and in a dry state. There were no statistically significant differences in the contents of combustible matter elements at significance level of 95% with the exception of N content in PA. In PA, the N at 1.91% wt. was higher in contrast to all other samples. Such a high amount of nitrogen can increase NO_x emission levels from combustion (Malaták and Bradna, 2017).

Percentages of non-flammable substances, such as ash and total moisture content shown in Table 1, indicate high contents of ash in the samples, especially in PA with 6.59% wt. of ash in dry matter. However, the ash contents are consistent with data on other herbaceous biomasses presented by other authors (Vassilev et al., 2010; Tao et al., 2012). Compared to wood biomass (Johansson et al., 2004), the ash content is generally higher in herbaceous biomass, especially in straws (Gürdil et al., 2009).

Very similar average gross calorific values were observed for CS and MG. The lowest average gross calorific value was

achieved for SB. This corresponds with the results of Vassilev et al. (2015).

The stoichiometric combustion calculations presented in Table 2 complement the fuel properties of the samples for evaluation of their combustion characteristics. Stoichiometric calculations use the average values for the original samples from Table 1. The results did not reveal any significant differences neither in the theoretical air consumption nor in the theoretical concentrations of the dry flue gas components between the materials. Larger differences were determined for CS in comparison to other samples. This material had the lowest combustion air consumption and the lowest dry flue gas production with the highest carbon dioxide content in the flue gas, the values of which reached 21.76% wt. – 21.37% vol.

The average emission concentrations are listed in Table 3. Statistically significant differences in average values in combustion tests were obtained between SB and MG briquettes. Combustion of SB achieved the highest average carbon monoxide emissions. When combusting the PA, the average emission concentrations of nitrogen oxides were at least twice as large as other briquette samples.

In all briquette samples, the emission concentration dependencies were similar as shown in Figs. 1–4. Emission concentrations of carbon monoxide increased with an increase in excess air ratio. The reason was lowering temperatures and premature cooling of combustion gases in the combustion chamber, as confirmed by Liu et al. (2010).

Table 1 Average values from proximate and elemental analysis

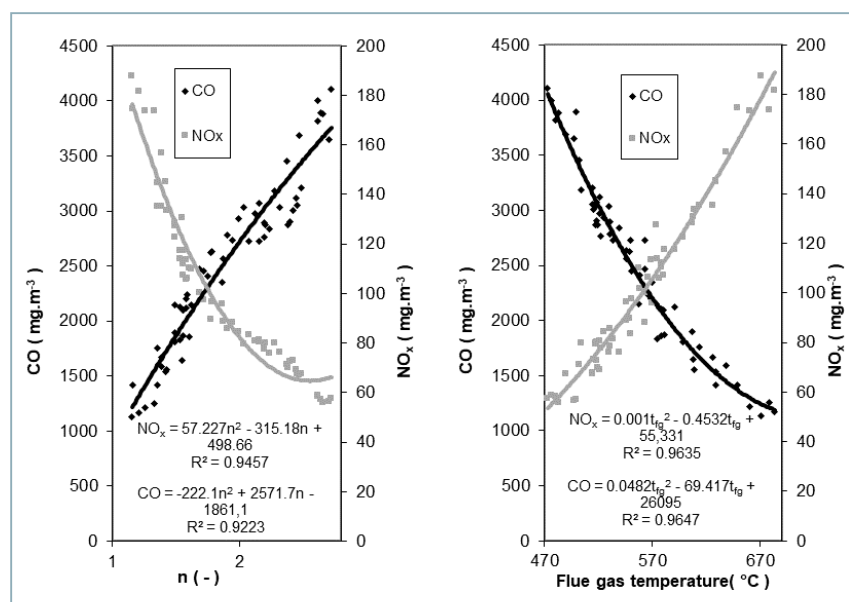
| Sample/Average values | Water content (% wt.) | Ash (% wt.) | Gross calorific value (MJ·kg ⁻¹) | Net calorific value (MJ·kg ⁻¹) | Carbon C (% wt.) | Hydrogen H (% wt.) | Nitrogen N (% wt.) | Sulphur S (% wt.) | Oxygen O (% wt.) |
|--|--------------------------|----------------|--|--|---------------------|-----------------------|-----------------------|----------------------|---------------------|
| | W | A | Q _s | Q _i | C | H | N | S | O |
| <i>Camelina sativa</i> original sample | 7.81 | 4.89 | 16.82 | 15.63 | 43.28 | 4.58 | 0.81 | 0.12 | 38.51 |
| <i>Camelina sativa</i> dry matter | – | 5.30 | 18.24 | 17.16 | 46.95 | 4.96 | 0.88 | 0.13 | 41.78 |
| <i>Miscanthus giganteus</i> original sample | 7.15 | 4.48 | 17.11 | 15.78 | 43.56 | 5.30 | 0.86 | 0.09 | 38.56 |
| <i>Miscanthus giganteus</i> dry matter | – | 4.82 | 18.43 | 17.18 | 46.91 | 5.71 | 0.93 | 0.10 | 41.53 |
| <i>Phalaris arundinacea</i> L. original sample | 6.29 | 6.18 | 16.59 | 15.25 | 42.11 | 5.45 | 1.79 | 0.10 | 38.08 |
| <i>Phalaris arundinacea</i> L. dry matter | – | 6.59 | 17.71 | 16.44 | 44.94 | 5.81 | 1.91 | 0.11 | 40.64 |
| <i>Sorghum bicolor</i> original sample | 6.52 | 5.72 | 16.21 | 14.90 | 42.58 | 5.28 | 0.58 | 0.11 | 39.21 |
| <i>Sorghum bicolor</i> dry matter | – | 6.12 | 17.34 | 16.11 | 45.55 | 5.65 | 0.62 | 0.12 | 41.94 |

Table 2 Results of stoichiometric combustion calculations

| Sample/Average values | Theoretical amount of air | | Theoretical amount of dry flue gases | | Theoretical concentration of carbon dioxide in dry flue gases | |
|--|------------------------------|----------------------------------|---|----------------------------------|--|--------|
| | kg·kg ⁻¹ | m ³ ·kg ⁻¹ | kg·kg ⁻¹ | m ³ ·kg ⁻¹ | % wt. | % vol. |
| <i>Camelina sativa</i> original sample | 4.90 | 3.77 | 7.29 | 3.76 | 21.76 | 21.37 |
| <i>Miscanthus giganteus</i> original sample | 5.18 | 3.99 | 7.51 | 3.93 | 21.26 | 20.57 |
| <i>Phalaris arundinacea</i> L. original sample | 5.08 | 3.91 | 7.40 | 3.85 | 20.87 | 20.28 |
| <i>Sorghum bicolor</i> original sample | 5.03 | 3.87 | 7.36 | 3.82 | 21.20 | 20.68 |

Table 3 Average values of flue gas temperature and the concentrations of components in dry flue gas in combustion tests

| | Flue gas temp. | O ₂ | CO ₂ | CO (O _{2r} = 13%) | NO _x (O _{2r} = 13%) |
|--|----------------|----------------|-----------------|----------------------------|---|
| | °C | % vol. | % vol. | mg·m ⁻³ | mg·m ⁻³ |
| <i>Camelina sativa</i> – original sample | | | | | |
| Average | 558.45 | 10.50 | 7.49 | 2,508.91 | 101.21 |
| Standard deviation | 52.85 | 2.31 | 2.19 | 773.31 | 34.42 |
| Max. | 683.00 | 13.81 | 14.10 | 4,107.00 | 187.70 |
| Min. | 472.80 | 5.50 | 5.20 | 1,133.00 | 55.80 |
| <i>Miscanthus giganteus</i> – original sample | | | | | |
| Average | 587.90 | 10.59 | 6.99 | 1,848.99 | 75.55 |
| Standard deviation | 57.14 | 1.70 | 1.99 | 1,193.45 | 14.65 |
| Max. | 705.00 | 13.08 | 12.00 | 4,572.00 | 111.32 |
| Min. | 489.80 | 6.29 | 4.10 | 343.00 | 55.33 |
| <i>Phalaris arundinacea</i> L. – original sample | | | | | |
| Average | 489.83 | 10.24 | 7.92 | 1,773.26 | 227.40 |
| Standard deviation | 0.10 | 0.17 | 0.18 | 0.33 | 0.20 |
| Max. | 655.00 | 13.33 | 15.20 | 2,757.00 | 375.20 |
| Min. | 423.90 | 5.48 | 6.20 | 442.00 | 167.20 |
| <i>Sorghum bicolor</i> – original sample | | | | | |
| Average | 499.69 | 12.41 | 4.85 | 2,680.05 | 91.25 |
| Standard deviation | 34.81 | 1.38 | 1.62 | 820.08 | 19.95 |
| Max. | 608.00 | 13.84 | 9.80 | 4,132.00 | 143.50 |
| Min. | 460.80 | 8.17 | 3.20 | 978.00 | 57.29 |

**Fig. 1** Emission concentration dependencies for *Camelina sativa*, values were converted to normal gas conditions and oxygen content 13% vol. in the flue gas

Emission concentrations of nitrogen oxides decreased with an increment in the excess air ratio. Similar trends for the observed emission concentrations were shown by Eskilsson et al. (2004) during combustion of pellets made of herbaceous biomass. Similar results were achieved by Strehler (2000); Houshfar et al. (2012); Černý et al. (2016) for fire wood pellets. In their case, the decreasing amount of combustion air reduced the amount of nitrogen oxides in the flue gas, but on the other hand, it also increased the unburnt carbon emissions. Since the emission concentrations are influenced by both the excess air coefficient and the flue gas temperature, these two parameters are plotted against each other in Fig. 5. It is clear from the graph that decreasing the value of the excess air coefficient increases the flue gas temperatures. Therefore, at the highest combustion temperature reached, the lowest value of the excess air coefficient was determined and vice versa. The high exhaust temperatures

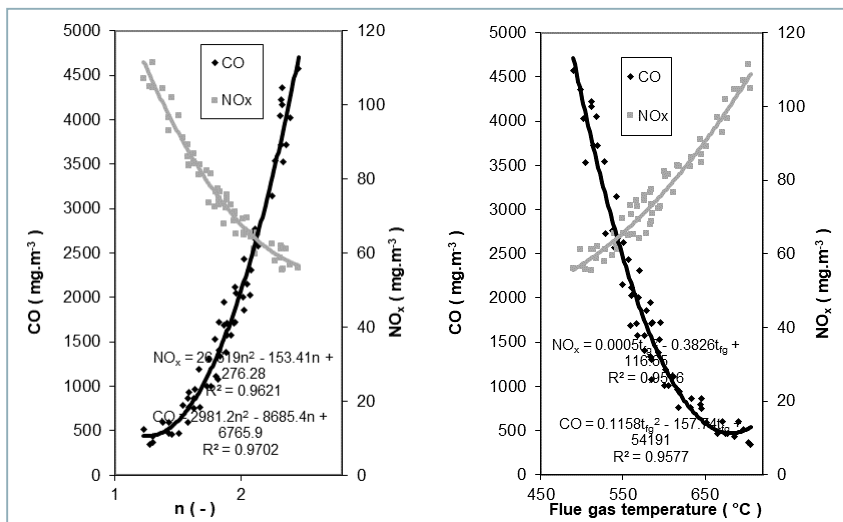


Fig. 2 Emission concentration dependencies for *Miscanthus giganteus*, values were converted to normal gas conditions and oxygen content 13% vol. in the flue gas

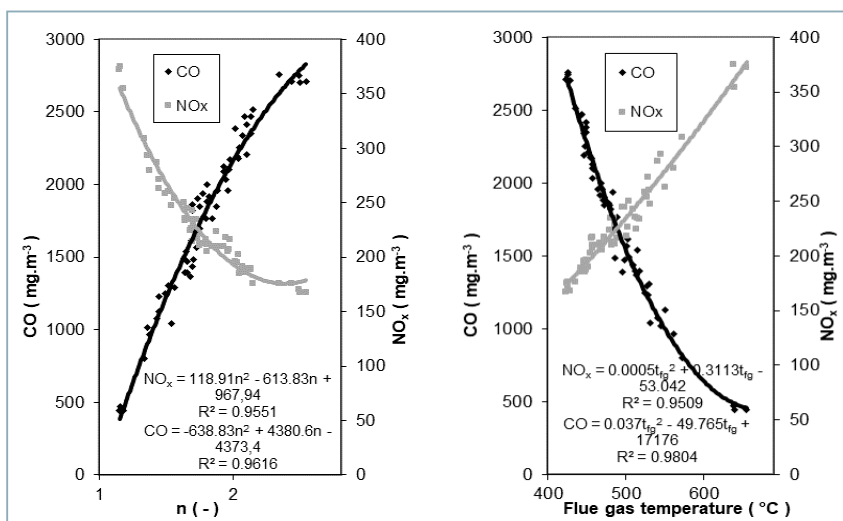


Fig. 3 Emission concentration dependencies for *Phalaris arundinacea* L., values were converted to normal gas conditions and oxygen content 13% vol. in the flue gas

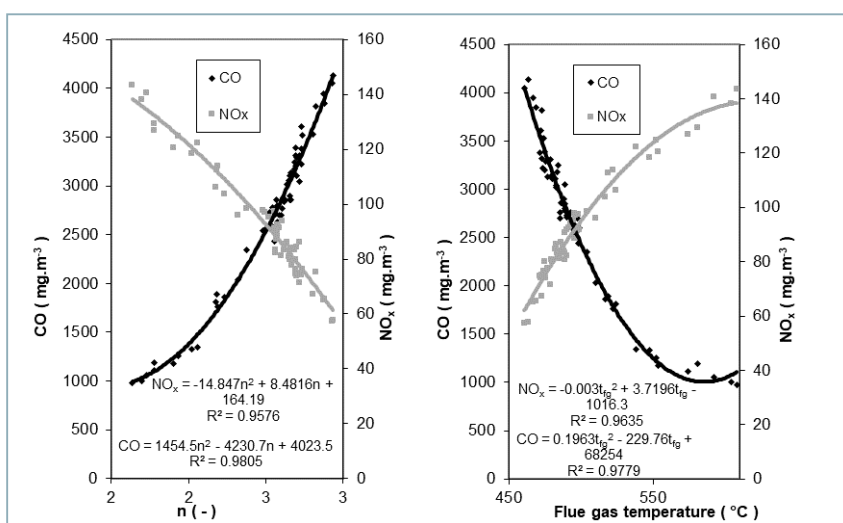


Fig. 4 Emission concentration dependencies for *Sorghum bicolor*, values were converted to normal gas conditions and oxygen content 13% vol. in the flue gas

during combustion tests were also achieved thanks to the high calorific values of the materials.

High concentrations of nitrogen oxides (375.20 mg.m⁻³) were found in combustion of PA at low excess air $n = 1.39$ and flue gas temperature 655 °C. This concentration exceeds the other materials several times over. The reasons for these high emissions are both high nitrogen content in the fuel, 1.79% wt., and high combustion temperature (Houshfar et al., 2012; Díaz-Ramírez et al., 2014; Kažimírová and Opáth, 2016). On the other hand, PA achieved the lowest carbon monoxide emission concentrations at low exhaust gas temperatures CO = (2,757.00 mg.m⁻³), whereas the other samples showed high emission concentrations above 4,000 mg.m⁻³. The emission measurements were processed by a regression statistical analysis to express the dependencies of carbon dioxide and nitrogen oxides on the coefficient of excess air and flue gas temperature. Figs. 1–4 show the graphs together with the regression equations. The correlation coefficient was always above 0.92 and mostly above 0.95.

Conclusion

This article is a response to stricter emission limits for combustion of briquette biomass in household combustion devices. The compositional, calorimetric and stoichiometric analyses of samples of herbaceous biomass briquettes characterise this type of fuel in many areas of its final use. Most important is their energy value, which is expressed in terms of the net calorific value and determines the thermal output of the combustion plant, as well as the production of gaseous emissions. Increasing the value of the excess air coefficient for combustion of briquettes resulted in a significant reduction in the emission levels of nitrogen oxides, as the flue gas temperature was reduced; however, carbon monoxide emissions were increased at the same time. It can be said that this general rule applies fully to both woody and herbaceous biomass samples despite the fact that elemental composition of pure wood differs mainly in terms of calorific value and ash content. The work also showed

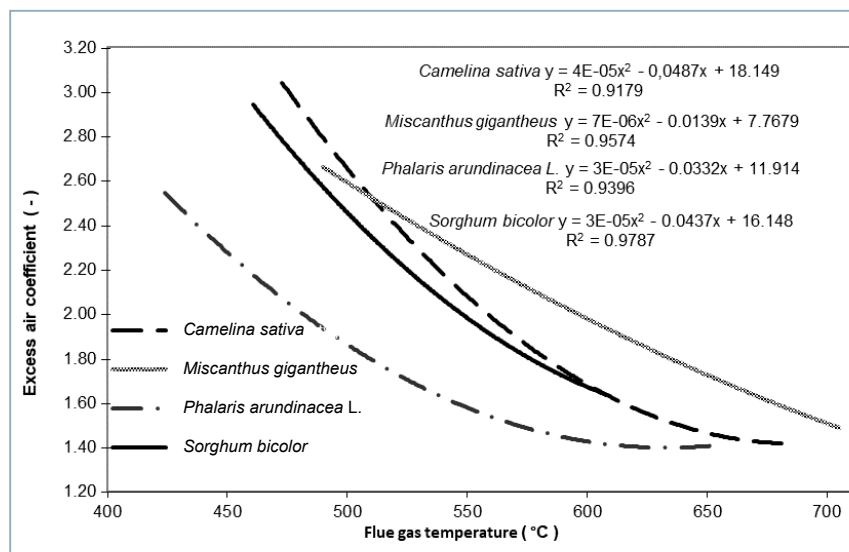


Fig. 5 Flue gas temperature dependency on the excess air coefficient for all materials

the influence of increased fuel nitrogen on the total emission concentration of nitrogen oxides in samples of *Phalaris arundinacea* L.

The results of the measurement of the emission concentrations confirm that the excess air coefficient is an important parameter for achieving the optimal combustion. The main factors include carbon monoxide and nitrogen oxides emissions, as well as the flue gas temperature, which is dependent on the coefficient of excess air. Particularly for *Miscanthus giganteus* briquettes, the highest concentrations of carbon monoxide were determined at the maximum excess air coefficient reached. Therefore, it makes sense even during combustion of these briquettes to regulate the combustion process using a lambda probe, which would guarantee the combustion under optimal conditions. Considering the combustion in the areas of optimal excess air coefficient, the CO and NO_x emission levels are produced with the lowest impact on the environment. By regulating the optimal amount of combustion air for this type of briquette biomass, heat losses can be avoided, thereby increasing the efficiency of briquette-fired combustion units.

Acknowledgements

This study was supported by the Internal Grant Agency of the Faculty of Engineering, Czech University of Life Science Prague, grant number: 2019: 31170/1312/3120.

References

- AMON, T. – AMON, B. – KRYVORUCHKO, V. – ZOLLITSCH, W. – MAYER, K. – GRUBER, L. 2007. Biogas production from maize and dairy cattle manure – Influence of biomass composition on the methane yield. In *Agriculture, Ecosystems and Environment*, vol. 118, no. 1–4, pp. 173–182.
- BRADNA, J. – MALATÁK, J. 2016. Flue gases thermal emission concentration during waste biomass combustion in small combustion device with manual fuel supply. In *Research in Agricultural Engineering*, vol. 62, no. 1, pp. 1–7.
- BRASSARD, P. – PALACIOS, J. H. – GODBOUT, S. – LAGACÉ, R. – LAROUCHE, J. P. – PELLETIER, F. 2014. Comparison of the gaseous and particulate matter emissions from the combustion of agricultural and forest biomasses. In *Bioresource Technology*, vol. 155, pp. 300–306.
- BRUNEROVÁ, A. – MALATÁK, J. – MÜLLER, M. – VALÁŠEK, P. – ROUBÍK, H. 2017. Tropical waste biomass potential for solid biofuels production. In *Agronomy Research*, vol. 15, no. 2, pp. 359–368.
- ČERNÝ, D. – MALATÁK, J. – BRADNA, J. 2016. Influence of biofuel moisture content on combustion and emission characteristics of stove. In *Agronomy Research*, vol. 14, no. 3, pp. 725–732.
- DHAUNDIYAL, A. – HANON, M. M. 2018. Calculation of kinetic parameters of the thermal decomposition of residual waste of coniferous species: *Cedrus deodara*. In *Acta Technologica Agriculturae*, vol. 21, no. 2, pp. 75–80.
- DÍAZ-RAMÍREZ, M. – SEBASTIÁN, F. – ROYO, J. – REZEAU, A. 2014. Influencing factors on NO_x emission level during grate conversion

of three pelletized energy crops. In *Applied Energy*, vol. 115, pp. 360–373.

DIN 14918: 2010. Solid biofuels – Determination of calorific value. Standard is the Czech version of the European Standard EN 14918: 2009. Czech Office for Standards, Metrology and Testing, 52.

ESKILSSON, D. – RÖNNBÄCK, M. – SAMUELSSON, J. – TULLIN, C. 2004. Optimisation of efficiency and emissions in pellet burners. In *Biomass and Bioenergy*, vol. 27, pp. 541–546.

ESTEBAN, B. – RIBA, J. R. – BAQUERO, G. – PUIG, R. – RIUS, A. 2014. Environmental assessment of small-scale production of wood chips as a fuel for residential heating boilers. In *Renewable Energy*, vol. 62, pp. 106–115.

EYNCK, C. – FALK, K. C. 2013. Camelina (*Camelina sativa*). In *Biofuel Crops: Production, Physiology and Genetics*, Saskatchewan S7N 0X2, Canada: CABI Publishing, pp. 369–391.

GARCIA-MARAVAR, A. – ZAMORANO, M. – FERNANDES, U. – RABAÇAL, M. – COSTA, M. 2014. Relationship between fuel quality and gaseous and particulate matter emissions in a domestic pellet-fired boiler. In *Fuel*, vol. 119, pp. 141–152.

GÜRDIL, G. A. K. – MALATÁK, J. – SELVI, K. C. – PINAR, Y. 2009. Biomass utilization for thermal energy. In *AMA, Agricultural Mechanization in Asia, Africa and Latin America*, vol. 40, no. 2, pp. 80–85.

HNILÍČKA, F. – HNILÍČKOVÁ, H. – HEJNÁK, V. 2015. Use of combustion methods for calorimetry in the applied physiology of plants. In *Journal of Thermal Analysis and Calorimetry*, vol. 120, no. 1, pp. 411–417.

HOUSHFAR, E. – LØVÅS, T. – SKREIBERG, Ø. 2012. Experimental investigation on NO_x reduction by primary measures in biomass combustion: Straw, peat, sewage sludge, forest residues and wood pellets. In *Energies*, vol. 5, no. 2, pp. 270–290.

JOHANSSON, L. S. – LECKNER, B. – GUSTAVSSON, L. – COOPER, D. – TULLIN, C. – POTTER, A. 2004. Emission characteristics of modern and old-type residential boilers fired with wood logs and wood pellets. In *Atmospheric Environment*, vol. 38, no. 25, pp. 4183–4195.

JUSZCZAK, M. 2016. Comparison of CO and NO_x concentrations from a 20 kW boiler for periodic and constant wood pellet supply. In *Environment Protection Engineering*, vol. 42, no. 3, pp. 95–107.

KAŽIMÍROVÁ, V. – OPÁTH, R. 2016. Biomass combustion emissions. In *Research in Agricultural Engineering*, vol. 62, pp. S61–S65.

KUČEROVÁ, V. – VÝBOHOVÁ, E. 2018. Release of saccharides during hot-water pretreatment of willow wood (*Salix alba* L.). In *Cellulose Chemistry and Technology*, vol. 52, no. 5–6, pp. 381–386.

- KUČEROVÁ, V. – VÝBOHOVÁ, E. – ČAŇOVÁ, I. – ĎURKOVIČ, J. 2016. The effects of both insoluble lignin and the macromolecular traits of cellulose on the content of saccharides within solids during hydrothermal pretreatment of hybrid poplar wood. In *Industrial Crops and Products*, vol. 91, pp. 22–31.
- LIU, H. – QIU, G. – SHAO, Y. – RIFFAT, S. B. 2010. Experimental investigation on flue gas emissions of a domestic biomass boiler under normal and idle combustion conditions. In *International Journal of Low-Carbon Technologies*, vol. 5, no. 2, pp. 88–95.
- MALATÁK, J. – BRADNA, J. – VELEBIL, J. 2016. Combustion of briquettes from oversize fraction of compost from wood waste and other biomass residues. In *Agronomy Research*, vol. 14, no. 2, pp. 525–532.
- MALATÁK, J. – BRADNA, J. 2017. Heating and emission properties of waste biomass in burner furnace. In *Research in Agricultural Engineering*, vol. 63, no. 1, pp. 16–22.
- MALATÁK, J. – BRADNA, J. – VELEBIL, J. 2017. The dependence of CO_x and NO_x emission concentrations on the excess air coefficient during combustion of selected agricultural briquetted by-products. In *Agronomy Research*, vol. 15, no. Special Issue 1, pp. 1084–1093.
- MALATÁK, J. – PASSIAN, L. 2011. Heat-emission analysis of small combustion equipments for biomass. In *Research in Agricultural Engineering*, vol. 57, no. 2, pp. 37–50.
- OBERNBERGER, I. – BRUNNER, T. – BÄRNTHALER, G. 2006. Chemical properties of solid biofuels – significance and impact. In *Biomass and Bioenergy*, vol. 30, no. 11, pp. 973–982.
- PLATAČE, R. – ADAMOVIČS, A. – GULBE, I. 2013. Evaluation of factors influencing calorific value of reed canary grass spring and autumn yield. In *Engineering for Rural Development 2013*. Latvia University of Agriculture, pp. 521–525. ISSN 16913043.
- STRAŠIL, Z. 1999. Production of above-ground biomass in *Miscanthus sinensis* in the Czech Republic. In *Rostlinna výroba*, vol. 45, no. 12, pp. 539–543.
- STREHLER, A. 2000. Technologies of wood combustion. In *Ecological Engineering*, vol. 16, pp. S25–S40.
- TAO, G. – LESTANDER, T. A. – GELADI, P. – XIONG, S. 2012. Biomass properties in association with plant species and assortments I: A synthesis based on literature data of energy properties. In *Renewable and Sustainable Energy Reviews*, vol. 16, no. 5, pp. 3481–3506.
- VASSILEV, S. V. – BAXTER, D. – ANDERSEN, L. K. – VASSILEVA, C. G. 2010. An overview of the chemical composition of biomass. In *Fuel*, vol. 89, no. 5, pp. 913–933.
- VASSILEV, S. V. – VASSILEVA, C. G. – VASSILEV, V. S. 2015. Advantages and disadvantages of composition and properties of biomass in comparison with coal: An overview. In *Fuel*, vol. 158, pp. 330–350.
- WIN, K. M. – PERSSON, T. – BALES, C. 2012. Particles and gaseous emissions from realistic operation of residential wood pellet heating systems. In *Atmospheric Environment*, vol. 59, pp. 320–327.
- ZOSIMA, A. T. – OCHSENKIIHN-PETROPOULOU, M. Th. 2015. Particulate matter emissions from combustion of different types of wood pellet. In *Fresenius Environmental Bulletin*, vol. 24, no. 1, pp. 146–156.



Acta Technologica Agriculturae 2
Nitra, Slovaca Universitas Agriculturae Nitriae, 2020, pp. 60–66

ENERGY REQUIREMENT OPTIMIZATION OF GREENHOUSE VEGETABLE PRODUCTION USING DATA ENVELOPMENT ANALYSIS (DEA) METHOD IN ALGERIA

Ahmed NOURANI^{1*}, Abdelaali BENCHEIKH²

¹Scientific and Technical Research Center on Arid Regions (CRSTRA), Biskra, Algeria

²University of Ahmed Draia Adrar, Algeria

Algeria has recently experienced an important agricultural development in terms of gardening in plastic greenhouses thanks to the favourable factors (climatic conditions, etc.). In order to optimize the energy requirements, data from 29 farmers were collected, who qualitatively represent the greenhouse vegetable producers from the most productive sub-provinces of Biskra region (south of Algeria). Considering the various parametric and non-parametric methods for energy consumption optimization, data envelopment analysis is the most common non-parametric method applied. Results showed that the mean radial technical efficiency assumptions of the samples under constant returns to scale and variable returns to scale models were 0.88 and 0.98, respectively. The 51.72% of decision-making units were efficient on the basis of the constant returns to scale model; 79.31% decision-making units were observed efficient on the basis of variable returns to scale model. Calculation of optimal energy requirements for vegetable greenhouse indicated that 108.50 GJ·ha⁻¹ can be saved on machinery (1.38 GJ·ha⁻¹); diesel fuel (4.68 GJ·ha⁻¹); infrastructure (9.35 GJ·ha⁻¹); fertilizers (17.08 GJ·ha⁻¹); farmyard manure (12.05 GJ·ha⁻¹); pesticides (3.93 GJ·ha⁻¹); and electricity (60.03 GJ·ha⁻¹).

Keywords: greenhouse cultivation; input–output analysis; Biskra; DEA; Algeria

During the last twenty years, Algeria showed a significant agricultural development caused by prosperous gardening in plastic greenhouses thanks to the favourable climatic conditions and the governmental policy (Nourani and Bencheikh, 2017). As results of this development, Biskra province became the most significant producer of early vegetables nationally (Allache et al., 2015); the area occupied by the greenhouses increased by 528.52% over the last 20 years (Belhadi et al., 2016). Greenhouses are constructed for the purpose of achieving the controlled environment suitable for crop production (Akpenpuun and Mijinyawa, 2018).

Agriculture is both a producer and consumer of energy (Bahrami et al., 2011). It utilizes large amounts of locally available non-commercial energies, such as seeds, manure, etc., as well as commercial energies in form of diesel fuel; electricity; fertilizers; irrigation water; etc. (Kizilaslan, 2009). Efficient exploitation of energies allows the achievement of increments in production and productivity and contributes to the economy, profitability and competitiveness of agriculture sustainability in rural living (Singh et al., 2002). Multiple authors have dealt with energy consumption optimization in greenhouses, e.g. for vegetable production (Firoozi et al., 2014), for cucumber production (Banaeian et al., 2012); however, there has not been published a study on energy input–output efficiency optimization of greenhouse vegetable production in MENA region. Furthermore, no papers published took into

account that infrastructure can be a considerable input in energy analyses.

With these observations in mind, this study is focused on the determination of the energy use efficiency, wasteful use of energy and selected energy requirements for greenhouse vegetable production in Biskra province, in the south of Algeria, in order to optimize the energy consumption.

Material and methods

Survey

According to Rekibi (2015), Biskra province is responsible for more than 32% of national production of protected crops, making it the most significant producer of early vegetables in Algeria. Therefore, this study was conducted in this region specifically for this reason. It took place in Biskra province during the 2014–2015 season and employed face-to-face personal interviews via questionnaires consisting of sections aimed at the economic characteristics, practices, and farm management. There were 29 farmers – qualitatively representing the producers of greenhouse vegetables in the most productive sub-provinces of Biskra – who participated in interviews. The most frequently produced vegetables in these sub-provinces include tomatoes; cucumbers; eggplants; and pepper.

Contact address: Ahmed Nourani, Scientific and Technical Research Center on Arid Regions (CRSTRA), Biskra, Algeria
e-mail: nourani83@gmail.com

Energy pattern

Agricultural energy requirements can be divided into two groups: direct (human labour; diesel fuel; water for irrigation; etc.) and indirect (seeds; fertilizers; farmyard manure; chemicals; machinery; infrastructure; etc.). On the basis of the energy equivalents of inputs and outputs (Table 1), metabolisable energy was calculated.

In order to analyse the energy flow, energy ratio (*energy use efficiency, ER*); *net energy (NE)*; *energy productivity (EP)*; and specific energy indices were calculated as follows:

$$\text{output - input ratio (ER)} = \frac{\text{energy output (MJ} \cdot \text{ha}^{-1})}{\text{energy input (MJ} \cdot \text{ha}^{-1})} \quad (1)$$

$$\text{energy productivity (EP)} = \frac{\text{total output (kg} \cdot \text{ha}^{-1})}{\text{energy input (MJ} \cdot \text{ha}^{-1})} \quad (2)$$

$$\text{net energy (NE)} = \text{energy output (MJ} \cdot \text{ha}^{-1}) - \text{energy input (MJ} \cdot \text{ha}^{-1}) \quad (3)$$

$$\text{specific energy} = \frac{\text{energy input (MJ} \cdot \text{ha}^{-1})}{\text{vegetable output (kg} \cdot \text{ha}^{-1})} \quad (4)$$

Table 1 Energy equivalents of inputs and outputs in greenhouse vegetable production

| Energy source | Unit | Energy equivalent (Mj·unit ⁻¹) | Reference |
|------------------------------------|--------------------|--|---------------------------|
| Inputs | | | |
| Human labour | h | 1.96 | Singh et al. (2002) |
| Machinery | h | 62.7 | Singh et al. (2002) |
| Diesel fuel | l | 45.4 | Bojacá et al. (2012) |
| Infrastructure | | | |
| - Steel | kg | 33 | Medina et al. (2006) |
| - Polyethylene | | 9.9 | Medina et al. (2006) |
| - Synthetic fibre | | 1.2 | Medina et al. (2006) |
| - PVC | | 11.6 | Medina et al. (2006) |
| Fertilizers | | | |
| - N | kg | 60.6 | Ozkan et al. (2004) |
| - P ₂ O ₅ | | 11.1 | Ozkan et al. (2004) |
| - K ₂ O | | 6.7 | Ozkan et al. (2004) |
| Farmyard manure | kg | 0.3 | Bojacá et al. (2012) |
| Pesticides | | | |
| - Fungicides | kg | 216 | Mohammadi and Omid (2010) |
| - Insecticides | | 101.2 | Mohammadi and Omid (2010) |
| Plant materials | | | |
| - Plantlets | unit | 0.2 | Bojacá et al. (2012) |
| Water for irrigation | m ³ | 0.63 | Bojacá et al. (2012) |
| Electricity | kW·h ⁻¹ | 3.6 | Ozkan et al. (2004) |
| Output | | | |
| Tomato, cucumber, eggplant, pepper | kg | 0.8 | Ozkan et al. (2004) |

Data envelopment analysis (DEA)

In terms of the various parametric and non-parametric methods for the energy consumption optimization, DEA is the most common method applied. Since its introduction, the DEA method has shown an exponential success: Emrouznejad et al. (2008) identified more than 4,000 published research articles on the DEA method in scientific journals or reference books. According to Huguenin (2013), this method was developed in order to evaluate the efficiency of a US federal program of resource allocation to schools ("Program Follow Through").

The DEA method makes it possible to evaluate the performance of the organizations (i.e. decision-making units – DMUs) that transform resources (inputs) into benefits (outputs). Its detailed description can be found in Banaeian et al. (2012).

Two basic models are utilized in DEA, each leading to the identification of a different efficiency frontier. The first model assumes that organizations evolve in a situation of constant returns to scale (CRS). According to this model, it is appropriate for all organizations to reach their optimal size (Charnes et al., 1978). The second model assumes that organizations evolve in a situation of variable returns to scale (VRS). In terms of this model, it is appropriate when organizations do not operate at their optimal size (Banker et al., 1984).

In order to select the inputs for DEA approach, a linear regression analysis for determination of effective energy inputs on yield was performed. The function used was of Cobb-Douglas production function form expressed as follows (Singh et al., 2004; Hatirli et al., 2006; Mohammadi and Omid, 2010; Banaeian et al., 2012):

$$Y_i = \alpha_0 + \sum_{j=1}^7 \alpha_j (x_{ij}) + e_i; \quad i = 1, 2, 3, \dots, 29 \quad (5)$$

where:

Y_i – i_{th} greenhouse yield

x_{ij} – vector of energy inputs used in the production process (x_{i1} – human labour, x_{i2} – machinery, x_{i3} – diesel fuel, x_{i4} – infrastructure, x_{i5} – fertilizer, x_{i6} – pesticide, x_{i7} – farmyard manure, x_{i8} – plantlets, x_{i9} – water for irrigation, x_{i10} – electricity)

α_0 – constant term
 α_j – coefficient of energy inputs which are estimated from the model

This function and its variations have been used by multiple authors (Singh et al., 2004; Hatirli et al., 2006; Mohammadi and Omid, 2010; Banaeian et al., 2012) to examine the relationship between input energy and yield.

In this study, input-oriented DEA seems more appropriate, given that it is more reasonable to argue that a farmer has more control over inputs rather than outputs in the agricultural sector (Nabavi-Pelesaraei et al., 2014).

Technical efficiency (TE)

Technical efficiency is a global measure of a DMU performance. The TE can be defined as follows (Nabavi-Pelesaraei et al., 2014):

$$TE_j = \frac{u_1 y_{1j} + u_2 y_{2j} \dots u_n y_{nj}}{v_1 x_{1j} + v_2 x_{2j} \dots v_m x_{mj}} = \frac{\sum_{r=1}^n u_r y_{rj}}{\sum_{s=1}^m v_s x_{sj}} \tag{6}$$

where:

- u_r – weight given to output n
- y_r – amount of output n
- v_s – weight given to input n
- x_s – amount of input n
- r – number of outputs ($r = 1, 2, \dots, n$)
- s – number of inputs ($s = 1, 2, \dots, m$)
- j – j^{th} of DMUs ($j = 1, 2, \dots, k$)

To solve the Eq. 1, following linear programming (LP) was formulated:

$$\begin{aligned} \text{Maximize: } \theta &= \sum_{r=1}^n u_r y_j \\ \text{Subjected to } &\sum_{r=1}^n u_r y_j - \sum_{s=1}^m v_s x_{sj} \leq 0 \\ &\sum_{s=1}^m v_s x_{sj} = 1 \\ &u_r \geq 0, v_s \geq 0, \wedge \end{aligned} \tag{7}$$

where:

- θ – technical efficiency

Model (3) is known as the input-oriented CRS DEA model – it assumes constant returns to scale (CRS) (Nabavi-Pelesaraei et al., 2014).

Scale efficiency (SE)

The SE relates to the most efficient scale of operations in the sense of maximizing the average productivity (Firoozi et al., 2014). Furthermore, scale efficiency represents the potential productivity gain from achieving the optimal size of a DMU (Reyhani-Farashah et al., 2013). The relationship between technical and pure technical efficiency scores can be described by the next formula (Mousavi-Avval et al., 2011):

$$\text{scale efficiency} = \frac{\text{technical efficiency}}{\text{pure technical efficiency}} \tag{8}$$

Considering the analysis of efficient and inefficient DMUs, the energy-saving target ratio (ESTR) index can be used, which represents the inefficiency level for each DMU with respect to the energy consumption (Nourani and Bencheikh, 2017). The formula for it is as follows (Firoozi et al., 2014):

$$ESTR_j = \frac{\text{energy saving target}_j}{\text{actual energy input}_j} \tag{9}$$

The aim is to save energy by overall reduction in inputs without decreasing the outputs (j - j^{th} DMU).

The majority of calculation was performed by means of the free application Win4Deap 2, version 2.1.

Results and discussion

Data were collected from 29 protected vegetable producers in Biskra province. The average size of a local greenhouse is approx. 2.1 ha with a range from 0.25 up to 12.75 ha. Observed greenhouses were made of plastic and had metallic structure. Furthermore, the data showed that majority of greenhouses utilized drip irrigation and approx. 73% of farms were privately owned and 27% rented.

The survey was actually conducted with a higher number of farmers – 65 – since there are two essential drawbacks of deterministic frontier models: both non-parametric and parametric models are very sensitive to outliers and extreme values; and noisy data is not allowed (Pahlavan et al., 2011). Therefore, higher number of farmers was selected in order to assure homogeneity on the basis of a specific area character.

By means of Eq. 1, $R^2 = 0.92$ was given by regression analysis of performance. All significant inputs, such as human labour; plantlets; etc., were taken into account; and analysis adopted the significant inputs and assumed seven input variables: infrastructure; fertilizers; farmyard

Table 2 Statics description of adopted inputs and output (Mj·ha⁻¹)

| | Machinery | Diesel fuel | Infrastructure | Fertilizers | Farmyard manure | Pesticide | Electricity | Yield |
|-------------|-----------|-------------|----------------|-------------|-----------------|------------|-------------|------------|
| Max. | 3,762 | 36,178.12 | 341,728.22 | 252,036 | 27,720 | 101,020.73 | 281,842.10 | 200,000 |
| Min. | 627 | 425.62 | 7,801.08 | 1,873.52 | 2,700 | 1,386 | 1,043.85 | 50,000 |
| Mean | 1,729.65 | 5,107.5 | 22,008.94 | 26,990.68 | 13,379.58 | 12,164.44 | 84,654.37 | 113,724.13 |
| SD | 742.39 | 7,414.62 | 61,502.86 | 46,145.70 | 6,725.31 | 20,590.45 | 70,952.94 | 36,756.82 |

manure; electricity; diesel fuel; pesticides; and machinery energy, which represent major energy inputs having impact on vegetable yield in the studied greenhouses, with 91% of total energy used. These are given in Table 2 with descriptive statistics for 29 vegetable producers. According to Cooper et al. (2001), the number of DMUs should be at least three times the total number of input and output factors taken into account when using the DEA model (Banaeian et al., 2012); therefore, this study works with a number of greenhouses that is three times the number of selected eight input-output variables for the performance model.

Technical, pure technical and scale efficiency of greenhouses

Table 3 describes the results acquired by means of input-oriented DEA. The mean radial TEs of the samples under CRS and VRS assumptions were 0.88 and 0.98, respectively. Moreover, 51.72% of DMUs (15 units) were observed efficient on the basis of CRS model; whereas, on the basis of VCR model, score of the pure TE was shown by 79.31% of DMUs (23 units). This implies that, in average, vegetable greenhouses can reduce their inputs by 12% (2%) and still maintain the identical output level – increasing of the greenhouse TE actually results in lower input usage,

Table 3 Results of the technical efficiency scores (technical, pure, and scale) and returns to scale

| DMU | Machinery | Diesel fuel | Infrastructure | Fertilizers | Farmyard manure | Pesticides | Electricity | Technical efficiency | | Scale efficiency | RTS |
|-----|-----------|-------------|----------------|-------------|-----------------|------------|-------------|----------------------|-------|------------------|-----|
| | | | | | | | | CRS | VRS | | |
| 1 | 1,254 | 11,350 | 10,441.916 | 75,340.40 | 18,168 | 12,459.360 | 14,092.105 | 1 | 1 | 1 | |
| 2 | 3,030.5 | 36,178.125 | 9,556.495 | 63,917.96 | 16,818 | 18,556.128 | 2,947.368 | 1 | 1 | 1 | |
| 3 | 2,508 | 14,896.875 | 10,289.178 | 9,968.16 | 4,800 | 1,764.720 | 10,736.842 | 1 | 1 | 1 | |
| 4 | 1,254 | 2,270 | 9,854.416 | 1,873.52 | 13,650 | 2,891.928 | 58,717.105 | 1 | 1 | 1 | |
| 5 | 1,463 | 851.25 | 12,727.083 | 16,576.72 | 8,400 | 6,128.760 | 93,947.368 | 0.825 | 1 | 0.825 | IRS |
| 6 | 1,463 | 16,315.625 | 10,246.330 | 33,302.32 | 8,550 | 11,760.30 | 10,892.449 | 0.918 | 1 | 0.918 | IRS |
| 7 | 1,254 | 1,418.75 | 10,292.416 | 26,807.72 | 22,230 | 5,969.250 | 156,578.95 | 0.726 | 0.924 | 0.786 | IRS |
| 8 | 3,135 | 5,675 | 10,596.916 | 10,747.68 | 16,800 | 3,841.354 | 36,013.158 | 1 | 1 | 1 | |
| 9 | 1,045 | 7,093.75 | 10,512.416 | 15,587.32 | 11,076 | 2,500.050 | 125,263.16 | 0.964 | 1 | 0.964 | IRS |
| 10 | 627 | 2,128.125 | 11,211.083 | 13,345.80 | 6,816 | 1,386.000 | 50,105.263 | 1 | 1 | 1 | |
| 11 | 1,881 | 2,128.125 | 11,040.416 | 13,320.64 | 8,400 | 2,023.152 | 156,578.94 | 1 | 1 | 1 | |
| 12 | 3,762 | 7,803.125 | 10,424.416 | 19,341.92 | 22,800 | 10,602.576 | 10,248.804 | 0.83 | 0.941 | 0.882 | IRS |
| 13 | 2,821.5 | 8,512.5 | 9,085.083 | 11,212.08 | 14,820 | 3,973.050 | 1,043.860 | 1 | 1 | 1 | |
| 14 | 1,881 | 9,931.25 | 10,300.988 | 3,403.76 | 22,230 | 5,996.160 | 10,736.842 | 1 | 1 | 1 | |
| 15 | 2,090 | 2,837.5 | 341,728.221 | 252,036.00 | 2,700 | 4,272.000 | 54,802.632 | 0.639 | 1 | 0.639 | IRS |
| 16 | 1,881 | 1,702.5 | 7,801.083 | 12,439.20 | 15,270 | 11,579.814 | 78,289.474 | 0.82 | 1 | 0.82 | IRS |
| 17 | 1,672 | 1,418.75 | 10,160.416 | 27,224.08 | 4,200 | 3,966.480 | 187,894.73 | 1 | 1 | 1 | |
| 18 | 1,672 | 1,418.75 | 10,820.416 | 26,136.52 | 4,200 | 3,257.280 | 75,157.895 | 1 | 1 | 1 | |
| 19 | 1,463 | 2,837.5 | 10,906.416 | 5,535.44 | 16,800 | 101,020.73 | 281,842.10 | 0.453 | 0.878 | 0.516 | IRS |
| 20 | 1,254 | 1,702.5 | 11,455.750 | 4,346.96 | 8,550 | 2,516.580 | 67,850.877 | 1 | 1 | 1 | |
| 21 | 1,985.5 | 1,418.75 | 10,112.416 | 18,032.00 | 2,940 | 14,253.278 | 56,368.421 | 0.591 | 1 | 0.591 | IRS |
| 22 | 1,881 | 709.375 | 11,432.416 | 20,359.00 | 22,230 | 46,751.400 | 250,526.31 | 0.67 | 0.854 | 0.785 | IRS |
| 23 | 1,254 | 993.125 | 10,678.131 | 18,431.40 | 17,100 | 1,729.740 | 89,473.684 | 1 | 1 | 1 | |
| 24 | 627 | 425.625 | 13,082.416 | 14,296.72 | 27,720 | 2,460.530 | 93,947.368 | 1 | 1 | 1 | |
| 25 | 1,567.5 | 993.125 | 13,012.988 | 9,481.60 | 18,900 | 48,045.600 | 89,473.684 | 0.663 | 0.989 | 0.670 | IRS |
| 26 | 1,881 | 1,276.875 | 10,575.528 | 5,912.74 | 9,810 | 7,297.476 | 93,947.368 | 0.808 | 1 | 0.808 | IRS |
| 27 | 1,254 | 851.25 | 12,164.416 | 13,343.20 | 15,750 | 4,879.392 | 125,263.16 | 0.668 | 0.99 | 0.675 | IRS |
| 28 | 731.5 | 2,270 | 9,875.166 | 21,634.64 | 12,600 | 2,632.320 | 46,973.684 | 1 | 1 | 1 | |
| 29 | 1,567.5 | 709.375 | 7,874.416 | 18,774.40 | 13,680 | 8,253.600 | 125,263.16 | 0.838 | 1 | 0.838 | IRS |

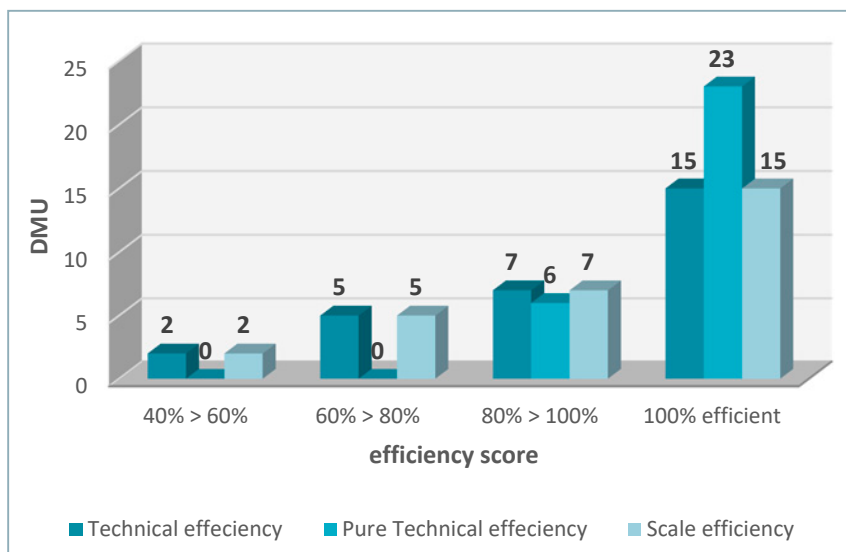


Fig. 1 Efficiency score distribution

production costs and higher profits, which is a motivation for producers to adopt new methods and technology (Firoozi et al., 2014).

Employing the Eq. 8, it is obvious that the scale efficiency equals to 1 for the units that had a score equal to 1 in CRS and VRS models. The efficiency score distribution of VRS and CRS models is shown in Fig. 1. Clearly, these results suggest that the difference between efficient and inefficient farmers was caused by differences in consumption of inputs in vegetable greenhouse production.

Consequently, farmers should adopt the consumption model of the efficient farmers. As shown in Fig. 1, 7 units were in the range 0.8–1 on the basis of CRS model, while VRS model results indicate that 6 units were equal to unity.

According to the results obtained, the DMUs designated with numbers 1, 2, 3, 4, 8, 10, 11, 13, 14, 17, 18, 20, 23, 24 and 28 are efficient and apply good practices. Due to same reason, CRS applied and scale efficiency equals to one, indicating that these farms are functioning at the most productive

scale size. The last table column – return to scale (RTS) – shows that all efficient DMUs (on the basis of TE) are functioning at constant return to scale (CRS), whereas the inefficient units are functioning at increasing return to scale (IRS), suggesting that there is need for significant adjustments in terms of yield and/or agricultural management. The IRS indicates that an increase in output was achieved by an increase in input resources, which was higher than proportionate. The scale efficiency (SE) reached the value of 0.88 in average, indicating that with efficient input utilization, the inefficient farmers can save some energy from the various input sources without any changes in agricultural practices. There were no units functioning at decreasing return to scale (DRS). Nabavi-Pelesaraei et al. (2016) investigated the wheat production energy efficiency with similar results.

Energy savings from different energy inputs

Table 4 illustrates the optimal energy requirements and energy savings in greenhouse vegetable production on the basis of the CRS model. In addition to this, a contribution to the savings in energy is also provided.

As shown in Table 4, the calculations of the optimal energy

Table 4 Optimal energy requirements and energy savings for vegetable greenhouse production

| Input | Optimal energy requirement (MJ·ha ⁻¹) | Saving energy (MJ·ha ⁻¹) | Saving energy (%) | Contribution to the savings in energy (%) |
|-----------------|---|--------------------------------------|-------------------|---|
| Machinery | 1,379.93 | 349.73 | 20.22% | 1.27% |
| Diesel fuel | 4,680.45 | 427.05 | 8.36% | 4.31% |
| Infrastructure | 9,348.70 | 12,660.24 | 57.52% | 8.62% |
| Fertilizers | 17,080.71 | 9,909.98 | 36.72% | 15.74% |
| Farmyard manure | 12,050.57 | 1,329.02 | 9.93% | 11.11% |
| Pesticides | 3,931.96 | 8,232.49 | 67.68% | 3.62% |
| Electricity | 60,033.21 | 24,621.16 | 29.08% | 55.33% |
| Total energy | 108,505.53 | 57,529.66 | 34.65% | 100.00% |

Table 5 Improvement of energy indices for vegetable greenhouse production

| Indices | Unit | Actual quantity | Optimal quantity | Difference (%) |
|---------------------|---------------------|-----------------|------------------|----------------|
| Energy ration | – | 49% | 72% | 31.94 |
| Energy productivity | kg·MJ ⁻¹ | 0.618162046 | 0.89941929 | 31.46 |
| Net energy | MJ·ha ⁻¹ | -92,992.09115 | -35,462.42738 | 61.86 |
| Specific energy | MJ·kg ⁻¹ | 1.6176988 | 1.1118285 | 31.67 |

requirements for vegetable greenhouse production suggest that 108.50 GJ·ha⁻¹ in total can be saved in terms of machinery (1.38 GJ·ha⁻¹); diesel fuel (4.68 GJ·ha⁻¹); infrastructure (9.35 GJ·ha⁻¹); fertilizers (17.08 GJ·ha⁻¹); farmyard manure (12.05 GJ·ha⁻¹); pesticides (3.93 GJ·ha⁻¹) and electricity (60.03 GJ·ha⁻¹). Consequently approx. 35% of total input energy in average can be saved if the farmers follow the recommendations provided in this study and maintain the current output level of greenhouse vegetable yield. Utilizing the similar methods, Firoozi et al. (2014) reported that, on average, 26.82% of the total input energy employed in greenhouse cucumber production in Iran can be saved.

Improvements of energy indices

Table 5 recapitulates the energy indices of actual and optimal quantities. The calculation demonstrates that the energy use efficiency is equal to 1.61 and 1.11 for actual and optimal quantities, respectively, with 0.51 of difference leading to an improvement of 31.67%. Furthermore, by converting the current energy use index to target energy use index, the energy ration, energy productivity and net energy can be improved approx. by 31.94%, 31.46%, 19.82% and 19.80%, respectively.

Nabavi-Pelesaraei et al. (2014) reported that the percentage of difference between target and optimal was approx. 24% for rice production.

Conclusions

This work is focused on optimization of the energy input-output for the protected crop production in Biskra province (South of Algeria) by means of the DEA approach. For this reason, a survey with 29 farmers was conducted.

Analysis adopted the significant inputs and assumed seven input variables: infrastructure; fertilizers; farmyard manure; electricity; diesel fuel; pesticides; and machinery energy – representing 91% of total energy used, as well as major energy inputs having significant impact on vegetable yield in the studied greenhouses.

The total energy necessary for protected crop production is 183.17 GJ per hectare. The 51.72% of DMUs (15 units) was observed efficient on the basis of CRS model; the pure technical efficiency score equalled to 1 in terms of 79.31% of DMUs (23 units) on the basis of VRS model, indicating their efficiency.

The calculation demonstrates that the energy use efficiency is equal to 1.61 and 1.11 for actual and optimal units, respectively, with 0.51 of difference leading to an improvement of 31.67%.

As recommendations, the following propositions can enhance the control over energy flow in protected vegetable production, as well as to allow the farmers to improve their financial situation; namely, providing farmers with training by a qualified person focused on improvement in their agricultural practices and enhancement of management over their inputs. Farmers should also improve the integrated pest management (IPM) by adoption of new methods for dealing with pests. In addition to these, awareness sessions for farmers regarding the effects of greenhouse gases on future generation should be elaborated.

Acknowledgement

This research was financially supported by the Scientific and Technical Research Centre for Arid Areas (CRSTRA), Biskra, Algeria. Gratitude is expressed to the agricultural specialists for their help in this work. Special thanks are extended to the farmers contributed in this survey.

References

- ALLACHE, F. – BOUTA, Y. – DEMNATI, F. 2015. Population development of the tomato moth *Tuta absoluta* (Lepidoptera: Gelechiidae) in greenhouse tomato in Biskra, Algeria. In Journal of Crop Protection, vol. 4, no. 4, pp. 509–517.
- AKPENPUUN, T. D. – MIJINYAWA, Y. 2018. Evaluation of a greenhouse under tropical conditions using Irish potato (*solanum tuberosum*) as the test crop. In Acta Technologica Agriculturae, vol. 21, no. 2, pp. 56–62.
- BAHRAMI, H. – TAKI, M. – MONJEZIM, N. 2011. Optimization of energy consumption for wheat production in Iran using data envelopment analysis (DEA) technique. In African Journal of Agricultural Research, vol. 6, no. 27, pp. 5978–5986.
- BANAEIAN, N. – OMID, M. – AHMADI, H. 2012. Greenhouse strawberry production in Iran, efficient or inefficient in energy. In Energy Efficiency, no. 5, pp. 201–209.
- BANKER, R. D. – CHARNES, A. – COOPER, W. W. 1984. Some models for estimating technical and scale inefficiencies in data envelopment analysis. In Management Science, vol. 30, no. 9, pp. 1078–1092.
- BELHADI, A. – MEHENNI, M. – REGUIEG, L. – YEKHLEF, H. 2016. Plasticulture contribution to agricultural dynamism in the Ziban region (Biskra). In Revue Agriculture, special issue 1, pp. 93–99.
- BOJACÁ, C. R. – CASILIMAS, H. A. – GIL, R. – SCHREVEVS, E. 2012. Extending the input-output energy balance methodology in agriculture through cluster analysis. In Energy, vol. 47, no. 1, pp. 465–470.
- CHARNES, A. – COOPER, W. W. – RHODES, E. 1978. Measuring the efficiency of decision making units. In European Journal of Operational Research, vol. 1978, no. 2, pp. 429–444.
- COOPER, W. W. – LI, S. – SEIFORD, L. M. – TONE, K. – THRALL, R. M. – ZHU, J. 2001. Sensitivity and stability analysis in DEA: Some recent developments. In Journal of Productivity Analysis, vol. 15, no. 3, pp. 217–246.
- EMROUZNEJAD, A. – PARKER, B. R. – TAVARES, G. 2008. Evaluation of research in efficiency and productivity: A survey and analysis of the first 30 years of scholarly literature in DEA. In Socio-Economic Planning Sciences, vol. 42, no. 3, pp. 151–157.
- FIROOZI, S. – SHEIKHDAVOODI, M. J. – FARANI, S. M. 2014. Optimizing energy consumption efficiency for greenhouse cucumber production using the DEA (data envelopment analysis) approach in Markazi Province of Iran. In International Journal of Agricultural Technology, vol. 10, no. 3, pp. 543–558.
- HATIRLI, S. A. – OZKAN, B. – FERT, C. 2006. Energy inputs and crop yield relationship in greenhouse tomato production. In Renewable Energy, vol. 31, no. 4, pp. 427–438.
- HUGUENIN, J. M. 2013. Data Envelopment Analysis (DEA). A pedagogical guide for decision makers in the public sector. IDHEAP, Lausanne, France, 90 pp. ISBN 978-2-940390-56-4.
- KIZILASLAN, H. 2009. Input-output energy analysis of cherries production in Tokat Province of Turkey. In Applied Energy, vol. 86, no. 7, pp. 1354–1358.
- MEDINA, A. A. – COOMAN, C. A. – PARRADO-SCHREVEVS, E. 2006. Evaluation of Energy Use and Some Environmental Impacts for Greenhouse Tomato Production in the High Altitude Tropics.

- Netherlands University of Wageningen, pp. 415–422. ISBN 9789066056091.
- MOHAMMADI, A – OMID, M. 2010. Economical analysis and relation between energy inputs and yield of greenhouse cucumber production in Iran. In *Applied Energy*, vol. 2010, no. 87, pp. 191–196.
- MOUSAVI-AVVAL, S. H. – RAFIEE, S. – JAFARI, A. – MOHAMMADI, A. 2011. Optimization of energy consumption for soybean production using Data Envelopment Analysis (DEA) approach. In *Applied Energy*, vol. 88, no. 11, pp. 3765–3772.
- NABAVI-PELESARAEI, A. – ABDI, R. – RAFIEE, S. – TAROMI, K. 2014. Applying data envelopment analysis approach to improve energy efficiency and reduce greenhouse gas emission of rice production. In *Engineering in Agriculture, Environment and Food*, vol. 5, no. 2, pp. 207–218.
- NABAVI-PELESARAEI, A. – HOSSEINZADEH-BANDBAFHA, H. – QASEMI-KORDKHEILI KOUCHAKI-PENCHAH, P. H. – RIAHI-DORCHEH, F. 2016. Applying optimization techniques to improve of energy efficiency and GHG (greenhouse gas) emissions of wheat production. In *Energy*, vol. 16, no. 103, pp. 672–678.
- NOURANI, A. – BENCHEIKH, A. 2017. Energy balance analysis and mechanization index for greenhouse vegetable production in southern of Algeria. An overview of Biskra province. In *INMATEH – Agricultural Engineering*, vol. 51, no. 1, pp. 1–8.
- OZKAN, B. – KURKLU, A. – AKCAOZ, H. 2004. An input–output energy analysis in greenhouse vegetable production: A case study for Antalya region of Turkey. In *Biomass Bioenergy*, vol. 29, no. 1, pp. 89–95.
- PAHLAVAN, R. – OMID, M. – AKRAM, A. 2011. Energy use efficiency in greenhouse tomato production in Iran. In *Energy*, vol. 36, no. 12, pp. 6714–6719.
- REYHANI-FARASHAH, H. – TABATABAEIFAR, S. A. – RAJABIPOUR, A. – SEFEEDPARI, P. 2013. Energy efficiency analysis of white button mushroom producers in Alburz Province of Iran: A data envelopment analysis approach. In *Open Journal of Energy Efficiency*, vol. 2, pp. 65–74.
- REKIBI, F. 2015. Competitive analysis for tomato cultivation under greenhouse, case of study: Biskra province. Msc. Thesis. Mohamed Kheider University, Biskra. (In French: Analyse compétitive de la filière tomate sous serre. Cas de la Wilaya de Biskra)
- SINGH, H. – MISHRA, D. – NAHAR, N. M. 2002. Energy use pattern in production agriculture of a typical village in arid zone India – Part I. In *Energy Conversion and Management*, vol. 43, no. 16, pp. 2275–86.
- SINGH, H. – MISHRA, D. – NAHAR, N. M. 2004. Energy use pattern in production agriculture of a typical village in arid zone India – Part III. In *Energy Conversion and Management*, vol. 45, no. 15–16, pp. 2453–2472.



Acta Technologica Agriculturae 2
Nitra, Slovaca Universitas Agriculturae Nitriae, 2020, pp. 67–72

INNOVATIVE HUSK-CRETE BUILDING MATERIALS FROM RICE CHAFF AND MODIFIED CEMENT MORTARS

Banjo AKINYEMI^{1*}, Temidayo E. OMONIYI², Olugbenga ELEMILE¹, Oluwafemi AROWOFILA¹

¹Structures and Environment Unit, Landmark University Omuaran, Kwara, Nigeria

²University of Ibadan, Oyo, Nigeria

The study considers the use of rice chaffs (husks) as an aggregate in a composite cement matrix system. Cement mortars were modified using styrene butadiene rubber polymer for strengthening. The goal is to develop a lightweight building material with good thermal insulation properties out of agricultural waste. The compressive strength, split tensile strength and flexural strength were experimentally evaluated. Further analyses of the samples were carried out by means of scanning electron microscope and energy dispersive spectroscopy. The key results obtained were presented and analysed with the performance of the proposed husk-crete building material showing adequate properties essential for a lightweight structural material with possible applications for non-structural purposes.

Keywords: rice husk; wastes; improvement; particle reinforcement; properties

Presently, there is a global awareness about the need to reduce the utilisation of building materials with high energy consumption because of their ecosystem damaging effects. There have been published detailed reports on their perceived contribution to climate change, greenhouse gas emission increase and devastating effects on the environment (Ürge-Vorsatz and Novikova, 2008). Focus has shifted to the utilization of wastes from agricultural processes on the basis of their environment friendly nature, renewability and recyclability traits (Akinyemi et al., 2019a). Furthermore, materials made of such wastes provide good indoor air quality and thermal comfort for humans; thereby they had become sought-after for different building purposes (Lima et al., 2016). There are numerous studies on utilization of plants or vegetables as reinforcement in both cementitious and non-cementitious applications in order to improve flexural strength; post-crack load resistance capability; impact toughness; increase bending strength; provide good thermal insulation; lower the thermal conductivity; etc. (Mueller, 2004; Sair et al., 2018). Such plants include hemp; bagasse; bamboo; coconut coir; corncob; and rice ashes and husks (Modani and Vyawahare, 2013; Akinyemi and Omoniyi, 2018a, Akinyemi and Omoniyi, 2018b, and Akinyemi et al., 2019b). Worldwide production of rice stands at over 800 million tonnes with majority of it coming from Asia; however, developing nations have lately also increased their production level (Onyango, 2014; Matías, 2019). The husk is a by-product of rice processing and takes up to 20% of the rice grain total volume. It is usually burnt and used as fuel or sent to landfills where it shows negative impact on the environment (Liu et al., 2013). However, there have been concerted efforts to acknowledge different

methods for recycling and reutilization of these wastes through their gainful inclusion to the building environment, reducing thus their negative impact on the eco-system. Rice husk is frequently utilized as thermal insulator in plastic composites, as well as in lightweight cement-based building materials (Choi et al., 2006; Salas et al., 1986). Numerous studies have already been conducted on the use of rice husk ashes as replacement for cement. Majority of these experiments showed that very low mechanical strengths were obtained using it as an aggregate in the mixture design. The study by Yuzer et al. (2013) showed that the compressive strength varied from 0.7 to 2.5 MPa; Chabannes et al. (2014) reported that optimum average compressive strength after 60 days was 0.33 MPa. Sutas et al. (2012) reported similar results: compressive strength varied from 0.5 to 5.5 MPa. Investigations on other plant materials used as aggregates in concrete showed similar results with low mechanical strength performances: from 0.4 to 1.22 MPa and from 0.26 to 0.80 MPa for wood crete and 0.5 MPa for hemp crete (Aigbomian and Fan, 2014; Arnaud and Gourlay, 2012). These results do not meet the minimal requirements for the materials to be designated as lightweight structural material based on the ACI classification; therefore, a supplementary supportive structure is required. In majority of aforementioned studies, these weaknesses in mechanical strength were taken into account and potential solutions were proposed; these include surface modification of fibres through alkaline solution; acidic treatment; hot water treatment; coating, dry/wet cycles; mechanical (pulping); thermal treatment (pyrolysis); etc. All these treatments would reduce the lignin, cellulose and hemicellulose in the fibres by disrupting the hydrogen

Contact address: Banjo Akinyemi, Structures and Environment Unit, Landmark University Omuaran, Department of Agricultural and Biosystems Engineering, Kwara, Nigeria, e-mail: bantonbows@gmail.com

bonds within the internal network (Benyahia et al., 2013). Subsequently, there is an increase in surface roughness of the fibre, which is necessary for proper bonding and strength development at the interface of the fibre-matrix (Prompunjai and Sridach, 2010). It is also feasible to improve the cement mortar through polymer modification, which would result in synchronised action alongside the alkaline treatment of the fibres in order to improve the ultimate strength of the composites. The use of polymer modification has been studied with excellent results reported in terms of enhancement of the mechanical strength of plant fibre-reinforced cement mortar and concrete (Yan et al., 2016; Ismail et al., 2008). Therefore, this study attempts to develop a husk-crete, which is a composite building material made of rice chaffs (husks) and polymer modified cement mortars. It is expected to conform to the compressive strength given by the ACI standard for lightweight structural material and show excellent thermal properties.

Material and methods

Rice husk waste preparation and treatment

The rice husk (RH) was sourced from a milling factory in Ekiti State (Nigeria) and dried to 2.5% moisture content (db) after exposure to the ambient surrounding for one week. The RH was sieved at 1.5 mm in order to remove unwanted materials and debris, which could affect the mixture properties. It has an average husk particle ranging from 0.77 to 1.3 mm. It was immersed in the diluted sodium hydroxide solution (5% conc.) for 2 hours. The mixture was decanted and washed in tap water to remove the leached-out chemicals and debris. Thereafter, the RH was dried in a ventilated oven at 50 °C for 2 hours before it was allowed to cool at the ambient temperature at 23 °C.

Cement and polymer additives

Type 1 Portland cement by Dangote Cement Ltd was used. The styrene butadiene rubber (SBR) polymer emulsion with 50% solid polymer content; pH of 9.2; and viscosity of 38–159 mPa·s⁻¹ (supplied by Advanced Concrete Technologies Ltd) was used to modify the cement mortar.

Mixture proportion and husk-crete sample preparation

Required quantities of cement and sand with ratio of 1 : 3 were measured and mixed thoroughly for approx. 3 minutes.

The RH volume varied (1 and 1.5% of the aggregates) while the SBR polymer of 10 and 15% (w/w) was used to modify the mixture (Table 1). The control sample (mixture A) contained 1.5% of RH on the basis of previous investigation (Banjo and Micheal, 2016) and was used for comparison purposes. Half of the necessary water was used to dilute the SBR emulsion for proper mixing with the aggregates and mixing was being performed manually for 2 minutes until homogenous colour and appearance were attained. Thereafter, the remaining water was blended together with the rest of constituents for another 3 minutes in order to produce slurry. Additional water was added until the desired slurry consistency was achieved. The mortar was cast in two types of moulds with dimensions 200 × 50 × 5 mm and 50 × 150 mm for mechanical tests.

Test methods

Flexural strength was observed by testing six specimens with dimensions 200 mm (length) × 50 mm (breadth) × 5 mm (width) after curing in water for 7, 14 and 28 days at a loading rate of 1.5 mm·min⁻¹ in compliance with the ASTM D1037 (2012) standard. Split tensile tests were conducted by testing six cylindrical samples according to the BS EN 12390-6 (2009) at a loading rate of 1.2 kN·secs⁻¹ after similar curing ages. The compressive strength was calculated on the basis of relationship between split tensile strength and compressive strength as shown in Eq. 1:

$$F_t = 0.3(F_c) \frac{2}{3} \text{ (MPa)} \quad (1)$$

where:

- F_t – split tensile strength
- F_c – compressive strength

SEM and EDS analyses were performed using Jeol-7600F equipment for micrograph observation, as well as elemental compositions of the fractured samples.

Results and discussion

Compressive strength

As expected, the compressive strength of control sample (mixture A at 1.5% RH) showed the worst performance. Generally, the observed trend in the husk-crete was that, at

Table 1 Experimental mixture design for husk-crete

| Components | Mixture design | | | | |
|--------------|-------------------|-------------------|-------------------|-------------------|-------------------|
| | A | B | C | D | E |
| Cement | 3 | 3 | 3 | 3 | 3 |
| Sand | 9 | 9 | 9 | 9 | 9 |
| Treated RH | 0.14 ^c | 0.10 ^a | 0.10 ^a | 0.14 ^a | 0.14 ^a |
| SBR polymer | – | 0.30 ^b | 0.45 ^b | 0.30 ^b | 0.45 ^b |
| Water:cement | 0.40 ^d | 0.35 ^d | 0.30 ^d | 0.35 ^d | 0.30 ^d |

a – weight of treated RH (kg), b – weight of 0.3% SBR polymer (kg), c – 1.5% RH was used as control (kg), d – water to cement ratios (ml)

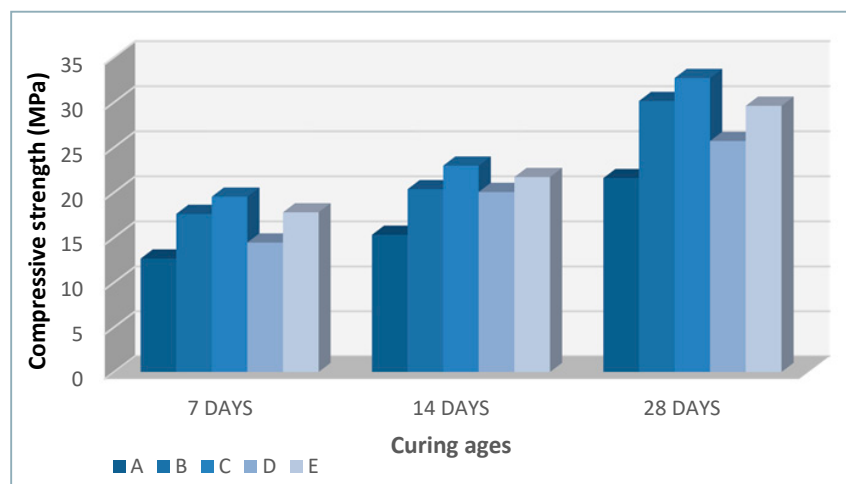
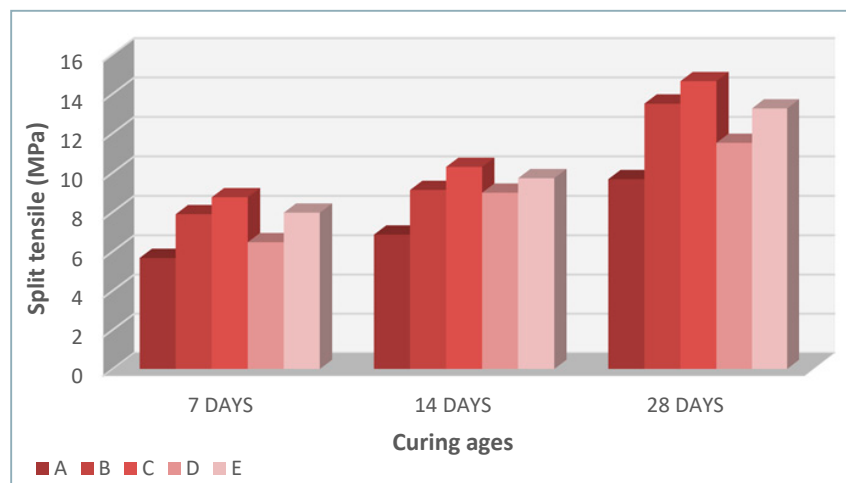
Table 2 ACI classification of lightweight concrete (Sari and Pasamehmetoglu, 2005)

| Properties | Lightweight concrete classifications | | |
|---|--------------------------------------|-------------|-------------|
| | low | moderate | structural |
| Unit weight ($\text{kg}\cdot\text{m}^{-3}$) | <1,000 | 1,000–1,500 | 1,500–2,000 |
| Compressive strength (MPa) | 0.70–2.00 | 2.00–15.00 | 16.00–42.00 |

any given fibre content, there was an incremental increase in compressive strength in the polymer dosage, e.g. in mixtures B and C with 1% RH aggregate and varying 10 and 15% SBR contents, there were increases in strength of 11, 12 and 9% after 7, 14 and 28 days, respectively. Furthermore, comparing mixtures D and E, increases of 7, 8 and 15% in compressive strength at 1.5% RH aggregate inclusion and varied SBR proportions were observed. The mechanism responsible for this improvement is the latex films within the SBR polymer, which develop into a polymeric arrangement in the internal

structure of the cement composite. It also transformed the transition zone at the interface between the RH and the cement particles, which resulted in the improved compressive strength (Shadmani et al., 2018). The abundant presence of latex in the spaces within the microstructure caused improved workability and compressive strength of the concrete composites. However, the effects of increasing RH content on the husk-crete material showed a decline in the compressive strength as reductions in the values were recorded across the curing regimes. In contrast to mixture B, at 10% SBR

dosage and 1 and 1.5% RH quantities, reductions of 22, 1.5 and 17% for mixture D after the curing ages were observed. A similar trend of reduction in the compressive strength with the RH aggregate increase from 1 to 1.5% at a given 15% SBR inclusion across the curing periods was observed as well. This showed that the porosity increased with increment in the rice husk content, which was accompanied by low strength performance of the husk-crete (Chabannes et al., 2015). The compressive strength of the husk-crete material depends on either the physical or chemical bonds, or combination of both bonds between the rice husk particles and cement. The chemical linkage is based on the interactions between the hydrogen bonds, which may form between husk particles, or possibly between the cement matrix and the husk particles. Physical connection can take place during the cement hydration phase, when C-S-H gels and other crystals are developed, interconnecting each with the rest (Pehanich et al., 2004). According to the ACI classification of lightweight concrete, the husk-crete material can be classified under category 3 as a lightweight structural material, since its compressive strength was within the specified minimum range of 16 MPa (Table 2).

**Fig. 1** Compressive strength of husk-crete material**Fig. 2** Split tensile strength of husk-crete material

Split tensile strength

The split tensile strength of the husk-crete material is shown in Fig. 2. A similar trend was observed in compressive strength, with strength improving by addition of both rice husk particles and polymers into the mixture. All samples showed better performance than the reference mixture in terms of the resistance to splitting forces. Considering the mixtures with 1% fibre content at varying polymer contents, the optimal split resistance was obtained at 14.64 MPa for sample C after 28 days. In the same vein, with 1.5% fibre inclusion and 10 and 15% polymer contents, mixture E showed

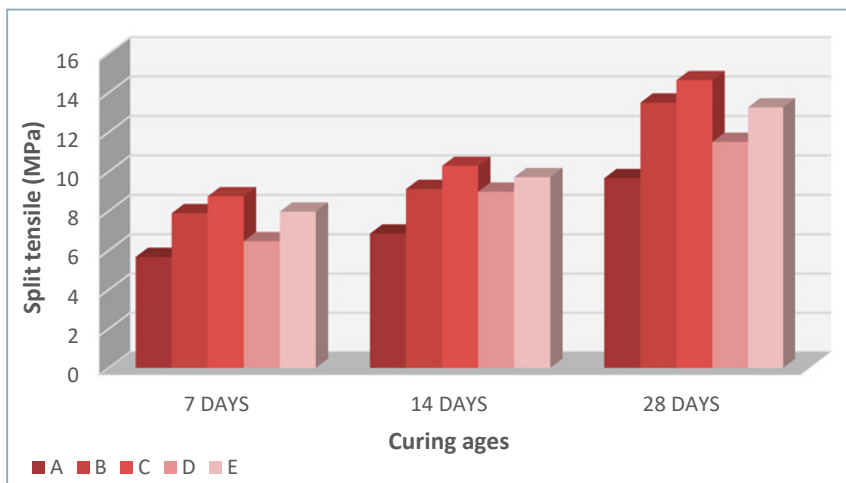


Fig. 3 Flexural strength performance of husk-brick samples

optimal split resistance of 13.26 MPa after 28 days of curing. This implies that the maximum rice husk content as an aggregate is 1%, a decrease in split strength takes place after exceeding this amount. However, it is noticeable that the use of SBR polymer in modification of the cement matrix led to significant enhancement of the husk-crete resistance to splitting forces. It was observed that the material showed higher resistance to tensile forces than polymer mortars because of its improved strength. This is thanks to an improved microstructure formed during the interaction and inter-connection between the cement hydration products and latex (Huang et al., 2010).

Flexural strength

Flexural strength performance of the husk-crete material is shown in Fig. 3.

It is obvious that inclusion of rice husk particles improved its flexural strength. Optimal resistance to bending was obtained in the mixture consisting of 1.5% husk particles coupled with the higher dose of SBR polymer with aging of 28 days. Similarly, an increase in flexural performance of earthen material stabilised with plant fibres varying at 2.5 and 5% (w/w) was reported by Villamizar et al. (2012). To support this observation as well, investigation on flexural strength of earthen material reinforced by vegetable fibre (Millogo et al., 2014) proved that, for each increase in fibre content, a resultant increase in flexural strength would take place until the optimal fibre content would be reached. Thereafter, a decline in the bending strength performance would take place. Consequently, the flexural performance results of this study are

in line with previous investigations indicating that, in majority of cases, an increase in flexural strength should be expected when reinforcing the material with plant-based aggregates. It is also necessary to emphasize that it is possible that the bond between the cement hydration products coupled with the SBR polymer latex films can be more efficient in terms of bonding with external convex structure of the rice husk particle. The flexural strength performance could also be influenced by the mechanical inter-connectivity mechanism, in which the cement matrix flows in its liquid form into the cell lumens and pores on the roughened surface of the fibre (due to alkaline treatment). Thereafter, it crystallized to develop into cement plugs, which eventually improved the strength by interlocking the fibre and matrix together (Nozahic et al., 2012).

Scanning electron microscope (SEM) and energy dispersive spectroscopy (EDS) analysis

SEM micrographs of selected mixtures made of the husk-crete material are shown in Fig. 4 (a–c). The reference mixture (sample A) showed a good distribution of conical projections of the rice husk particles at regular intervals on the surface of composites. It is possible to observe abundant presence of pores and voids on the surface (Fig. 4c) with a higher magnification. These were responsible for the weak strength shown by this mixture during the mechanical tests. Compact interfaces free of pores due

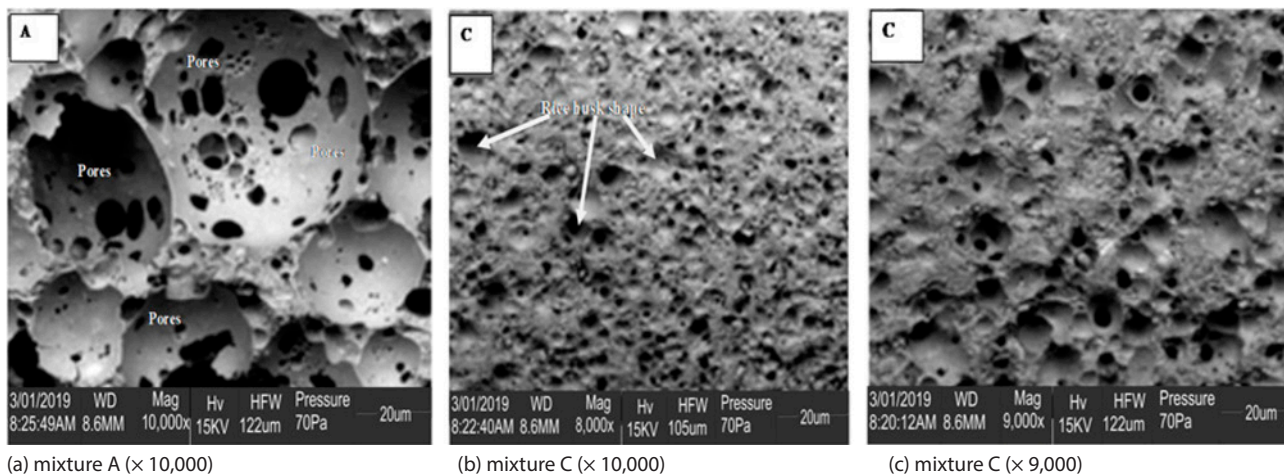


Fig. 3 SEM micrograph of husk-crete lightweight material

Table 3 Elemental analysis of samples

| | Elements (%) | | | | | |
|-----------|--------------|-------|------|-------|-------|------|
| | C | O | Fe | Ca | Si | Mg |
| Mixture C | 4.10 | 36.33 | 4.25 | 45.25 | 8.40 | 1.44 |
| Mixture A | 5.50 | 35.30 | 6.10 | 40.20 | 11.55 | 1.20 |

to the filling of the voids on the fibre-matrix interface with the reaction of the cement hydrate products and latex film polymers was observed for sample C. EDS analysis was conducted on selected regions of the samples tested and the results are displayed in Table 3. All samples consisted of silicon; carbon; calcium; oxygen; and iron with traces of magnesium. It is, however, clear that sodium was not discovered in any of the samples; this attests to the efficacy of the alkaline treatment of RH in removing it. The Ca/Si ratios were also responsible for the formation of calcium silicate hydrate (C-S-H) at the composite surface. The SBR polymer emulsion also improved the fibre-pozzolan bonding situations, aided the pozzolanic chemical reactions and boosted the process of cement hydration (Plank and Gretz, 2008).

Conclusions

The study presented outlined the utilization possibilities of rice chaffs (husks) as an aggregate in developing a lightweight structural building material with good thermal insulation properties. Compressive strength tests showed that increasing of rice husk content in the husk-crete material resulted in a decline across the curing regimes. However, increasing the dosage of the SBR improved the resistance of the husk-crete material to compressive forces. Flexural strength performance results indicated improvements in strength as the proportion of the husk aggregates increased. It is also interesting to note that this strength is possibly caused by the bond between the cement hydration products coupled with the SBR polymer latex films having more effectiveness in bonding with the external convex structure of the rice husk particle. With the help of SEM/EDS, the study was able to show that treatment of rice husk with alkali chemicals and use of polymer additive for strengthening the cement mortar assisted in improving the bond at the interface between the husk particles and the cement matrix. Therefore, its use can be recommended for the purposes of reinforcement in development of lightweight building materials. Further studies on the durability of such materials under various environmental conditions should be carried out as well.

References

- AIGBOMIAN, E. P. – FAN, M. 2014. Development of wood-crete from treated sawdust. In *Construction and Building Materials*, vol. 52, pp. 353–360.
- AKINYEMI, B. A. – OMONIYI, T. E. 2018a. Effect of moisture on thermal properties of acrylic polymer modified mortar reinforced with alkali treated bamboo fibres. In *Journal of the Indian Academy of Wood Science*, vol. 15, no. 1, pp. 45–51.
- AKINYEMI, B. – OMONIYI, T. 2018b. Properties of latex polymer modified mortars reinforced with waste bamboo fibers from construction waste. In *Buildings*, vol. 8, no. 11, pp. 149.
- AKINYEMI, B.A. – OKONKWO, C.E. – ALHASSAN, E.A. – AJIBOYE M. 2019a. Durability and strength properties of particle boards from polystyrene-wood wastes. *Journal of Material Cycles and Waste Management*. <https://doi.org/10.1007/s10163-019-00905-6>
- AKINYEMI, B. A. – BAMIDELE, A. – JOEL, E. 2019b. Response of coir fibre reinforced cement composites to water repellent chemical additive and microwave accelerated curing. In *Cellulose*, vol. 26, no. 8, pp. 4987–4999.
- ARNAUD, L. – GOURLAY, E. 2012. Experimental study of parameters influencing mechanical properties of hemp concretes. In *Construction and Building Materials*, vol. 28, no. 1, pp. 50–56.
- ASTM D1037. 2012. Standard test methods for evaluating properties of wood-base fibre and particle panel materials.
- BANJO, A. – MICHEAL, O. 2016. Prospects of coir fibre as reinforcement in termite mound clay material. In *Acta Technologica Agriculturae*, vol. 19, no. 3, pp. 57–62.
- BENYAHIA, A. – MERROUCHE, A. – ROKBI, M. – KOUADRI, Z. 2013. Study of the alkali treatment effect on the mechanical behavior of the composite unsaturated polyester-Alfa fibers. In *Mechanics and Industry*, vol. 15, no. 1, pp. 69–73.
- BRITISH STANDARDS INSTITUTE. 2009. BS EN 12390–6: 2009. Testing hardened concrete Part 6: Tensile splitting strength of test specimens.
- CHABANNES, M. – BÉNÉZET, J. C. – CLERC, L. – GARCIA-DIAZ, E. 2014. Use of raw rice husk as natural aggregate in a lightweight insulating concrete: An innovative application. In *Construction and Building Materials*, vol. 70, pp. 428–438.
- CHABANNES, M. – GARCIA-DIAZ, E. – CLERC, L. – BÉNÉZET, J. C. 2015. Studying the hardening and mechanical performances of rice husk and hemp-based building materials cured under natural and accelerated carbonation. In *Construction and Building Materials*, vol. 94, pp. 105–115.
- CHOI, N. W. – MORI, I. – OHAMA, Y. 2006. Development of rice husks-plastics composites for building materials. In *Waste Management*, vol. 26, no. 2, pp. 189–194.
- HUANG, B. – WU, H. – SHU, X. – BURDETTE, E. G. 2010. Laboratory evaluation of permeability and strength of polymer-modified pervious concrete. In *Construction and Building Materials* vol. 24, pp. 818–823.
- ISMAIL, M. R. – YOUSSEF, H. A. – ALI, M. A. – ZAHRAN, A. H. – AFIFI, M. S. 2008. Utilization of emulsion polymer for preparing bagasse fibers polymer-cement composites. In *Journal of Applied Polymer Science*, vol. 107, no. 3, pp. 1900–1910.
- LIMA, J. – FARIA, P. – SANTOS SILVA, A. 2016. Earthen plasters based on illitic soils from Barrocal region of Algarve: contributions for building performance and sustainability. In *Key Engineering Materials*, vol. 678, pp. 64–77.
- LIU, N. – HUO, K. – McDOWELL, M. T. – ZHAO, J. – CUI, Y. 2013. Rice husks as a sustainable source of nanostructured silicon for high performance Li-ion battery anodes. In *Scientific Reports*, vol. 3.
- MATÍAS, J. – CRUZ, V. – GARCÍA, A. – GONZÁLEZ, D. 2019. Evaluation of rice straw yield, fibre composition and collection under

- Mediterranean conditions. In *Acta Technologica Agriculturae*, vol. 22, no. 2, pp. 43–47.
- MILLOGO, Y. – MOREL, J. C. – AUBERT, J. E. – GHAVAMI, K. 2014. Experimental analysis of Pressed Adobe Blocks reinforced with Hibiscus cannabinus fibers. In *Construction and Building Materials*, vol. 52, pp. 71–78.
- MODANI, P. O. – VYAWAHARE, M. R. 2013. Utilization of bagasse ash as a partial replacement of fine aggregate in concrete. In *Procedia Engineering*, vol. 51, pp. 25–29.
- MUELLER, D. H. 2004. Improving the impact strength of natural fiber reinforced composites by specifically designed material and process parameters. In *International Nonwovens Journal*, vol. 4, pp. 1558925004os–1300405.
- NOZAHIC, V. – AMZIANE, S. – TORRENT, G. – SAÏDI, K. – DE BAYNAST, H. 2012. Design of green concrete made of plant-derived aggregates and a pumice-lime binder. In *Cement and Concrete Composites*, vol. 34, no. 2, pp. 231–241.
- ONYANGO, A. O. 2014. Exploring options for improving rice production to reduce hunger and poverty in Kenya. In *World Environment*, vol. 4, no. 4, pp. 172–179.
- PEHANICH, J. L. – BLANKENHORN, P. R. – SILSBEE, M. R. 2004. Wood fiber surface treatment level effects on selected mechanical properties of wood fiber-cement composites. In *Cement and Concrete Research*, vol. 34, no. 1, pp. 59–65.
- PLANK, J. – GRETZ, M. 2008. Study on the interaction between anionic and cationic latex particles and Portland cement. In *Colloids and Surfaces A: Physicochemical and Engineering Aspects*, vol. 330, no. 2–3, pp. 227–233.
- PROMPUNJAI, A. – SRIDACH, W. 2010. Preparation and some mechanical properties of composite materials made from sawdust, cassava starch and natural rubber latex. In *International Journal of Materials and Metallurgical Engineering*, vol. 4, no. 12, pp. 773–776.
- SAIR, S. – OUSHABI, A. – KAMMOUNI, A. – TANANE, O. – ABOUD, Y. – EL BOUARI, A. 2018. Mechanical and thermal conductivity properties of hemp fiber reinforced polyurethane composites. In *Case Studies in Construction Materials*, vol. 8, pp. 203–212.
- SALAS, J. – ALVAREZ, M. – VERAS, J. 1986. Lightweight insulating concretes with rice husk. In *International Journal of Cement Composites and Lightweight Concrete*, vol. 8, no. 3, pp. 171–180.
- SARI, D. – PASAMEHMETOGLU, A. G. 2005. The effects of gradation and admixture on the pumice lightweight aggregate concrete. In *Cement and Concrete Research*, vol. 35, no. 5, pp. 936–942.
- SHADMANI, A. – TAHMOURESI, B. – SARADAR, A. – MOHSENI, E. 2018. Durability and microstructure properties of SBR-modified concrete containing recycled asphalt pavement. In *Construction and Building Materials*, vol. 185, pp. 380–390.
- SUTAS, J. – MANA, A. – PITAK, L. 2012. Effect of rice husk and rice husk ash to properties of material. In *Procedia Engineering*, vol. 32, pp. 1061–1067.
- ÜRGE-VORSATZ, D. – NOVIKOVA, A. 2008. Potentials and costs of carbon dioxide mitigation in the world's buildings. In *Energy Policy*, vol. 36, no. 2, pp. 642–661.
- VILLAMIZAR, M. C. N. – ARAQUE, V. S. – REYES, C. A. R. – SILVA, R. S. 2012. Effect of the addition of coal-ash and cassava peels on the engineering properties of compressed earth blocks. In *Construction and Building Materials*, vol. 36, pp. 276–286.
- YAN, L. – CHOUW, N. – HUANG, L. – KASAL, B. 2016. Effect of alkali treatment on microstructure and mechanical properties of coir fibres, coir fibre reinforced-polymer composites and reinforced-cementitious composites. In *Construction and Building Materials*, vol. 112, pp. 168–182.
- YUZER, N. – CINAR, Z. – AKOZ, F. – BIRICIK, H. – GURKAN, Y. Y. – KABAY, N. – KIZILKANAT, A. B. 2013. Influence of raw rice husk addition on structure and properties of concrete. In *Construction and Building Materials*, vol. 44, pp. 54–62.



Acta Technologica Agriculturae 2
Nitra, Slovaca Universitas Agriculturae Nitriae, 2020, pp. 73–80

APPLICATION OF PERCOLATION THEORY IN THERMOKINETICS

Alok DHAUNDIYAL^{1*}, Suraj BHAN SINGH²

¹Szent István University, Gödöllő, Hungary

²Govind Ballabh Pant University of Agriculture and Technology, Pantnagar, Uttarakhand, India

The present paper focuses on the infiltration of random fluid particles through a porous wall. The thermogravimetric curve is assumed to be a non-eroded interface so that the random fluid particle can pass through the discrete boundary of it. The node on the thermogravimetric plane is denoted by the three-dimensional lattice, which has unit thickness. The Lattice Boltzmann method is implemented to determine the variation of the remaining mass fraction (X) with respect to time. The kinetic model is correlated with the Lattice Boltzmann method to determine the kinetic parameters. The practical situation of Moka coffee maker is applied to determining the kinetic parameters.

Keywords: kinetic model; Lattice Boltzmann method; percolation; kinetic parameters; thermogravimetry

This paper is based on the assumptions that the discontinuity of a curve can be treated as a passage for a fluid element to pass out of the three-dimensional thermogravimetric plane and the rate of change of displacement corresponds to the variation of remaining mass fraction. The displacement of a fluid element with respect to the time can be represented through a mass distribution function associated with velocity and flow density. In this article, a physical model of percolation of coffee is correlated with the chemical kinetic model. Temperature and time are assumed to be related to the three-dimensional node of a fluid particle. Percolation concept comprises two stages: ingress of fluid elements through the inlet and passing through a porous medium with the help of body force or a low-pressure gradient. Furthermore, it wets the porous medium and expels the air. The body force or existence of a low-pressure gradient makes the small particles of porous interface detach from larger grains, and they drain away with the fluid. As a result of erosion, they can either deposit on other grains, or get sedimented. A Lattice Boltzmann method (LBM) is implemented to determine the mass flow rate of the hypothetical fluid element through the porous plane. The basic Lattice Boltzmann D3Q19 (three-dimensional and 19 velocities) (Habich et al., 2011) model is used to simulate percolation of the fluid elements across the plane. The boundary of the porous wall is assumed to be non-eroded, which means it will not dissolve or lose sub-particle in the hypothetical fluid. The broad perspective of LBM covers the simulation of fluid flow. It solves the Boltzmann equation for a discrete lattice and assists in recovering of the Navier-Stokes equation by reducing the Mach number. Although the LBM has compressibility effect, it can be reduced to the incompressible fluid if dilatational viscosity is negligible.

The method can be applied to the simulation of flow in porous media (Kutay et al., 2006), colloidal suspensions (Harting et al., 2008), liquid-gas phase transitions, multi-component flow (Huang et al., 2011; Nekovee et al., 2000), and spinodal decomposition (Giupponi et al., 2006). Besides the microscopic application, the LBM may have a wide scope in the macroscopic issues of gasification and pyrolysis. The paper focuses on the implementation of percolation theory to simulate the remaining mass fraction of hardwood and correlate it with a multi-reaction model in order to evaluate the relevant kinetic parameters with the help of the inverse solution. Unlike the Monte Carlo method (Dhaundiyal et al., 2019), the concept of percolation is based on the dynamic nature of fluid nodes. Overlapping of random fluid particles and nonhomogeneous concentration of fluid and void space impart a significant error while measuring the area bounded by the TG curves. Therefore, it must be tackled in such a manner so that the error encountered whilst evaluating kinetic parameters can be minimised.

Material and methods

The Lattice Boltzmann method for fluid simulation

The LBM is used to solve the Boltzmann equation (Eq. 1) for a discrete system. It defines the dynamic behaviour of a gas in a microscopic system. The collision of gas particles with velocity v_i is highly stochastic and, hence, it exchanges momentum among themselves. The total momentum and energy of the system are conserved for the ideal collision. Role of the Boltzmann equation is to determine the velocity of a particle as a probability function of position and time, $f(k, t)$.

Contact address: Alok Dhaundiyal, Szent István University, Institute of Process Engineering, Gödöllő 2100, Hungary

$$v \cdot \nabla_k f + F \cdot \nabla_p f + \frac{df}{dt} = \Omega(f(k,t)) \tag{1}$$

where:

- f – external body force or mass distribution function
- ∇_k, ∇_p – gradient in position and momentum space respectively
- $\Omega(f)$ – collision operator

The collision operation relationship (Eq. 2) with the equilibrium distribution and relaxation time τ is proposed by Bhatnagar, Gross and Krook (BGK dynamics) (Bhatnagar et al., 1954).

$$\hat{\Omega}(f) = -\left(\frac{f_i - f_i^{eq}}{\tau}\right) \tag{2}$$

Here, the equilibrium value f^{eq} is obtained by discretising the Boltzmann distribution (Eq. 3). The expression is limited up to the second order (Li et al., 2013; Guo et al., 2006).

$$f_i^{eq}(\rho, v) = w_i \rho \left[1 + \frac{c_i \cdot v}{(c_s)^2} + \left(\frac{c_i \cdot v}{(c_s)^2}\right)^2 - \frac{v^2}{2c_s^2} \right] \tag{3}$$

where $w_i = \begin{cases} \frac{1}{3}, & i=0 \\ \frac{1}{18}, & i=1, \dots, 6 \\ \frac{1}{36}, & i=7, 8, \dots, 18 \end{cases}$ denotes the lattice weights,

and $c_s = \frac{1}{\sqrt{3}}$ is the lattice speed of sound for D3Q19. The equilibrium distribution function for a fluid model depends on the local density $\rho(k, t)$ and the velocity field $v(k, t)$. The LBM discretises the probability density function f in space and time. The equilibrium distribution f^{eq} depends on the

lattice type used for the fluid simulation. But the most popular and widely used for 3D lattice fluid simulation is D3Q19 (Hecht and Harting, 2010), where each node has 19 links. The other three-dimensional lattice models used in fluid simulation are D3Q15 and D3Q27. The D3Q27 has the highest computational effort, whereas the D3Q15 has the least stability among the 3D models. Apart from 3D lattice models, for 2D simulation, D2Q9, which consists of 9 discrete velocity directions, is used for two-dimensional fluid flow. For each lattice site, 19 distribution functions ($f_i(k, t)$) are used. Each lattice has assigned a lattice velocity C_i vector. The subscript i denotes the i^{th} column of lattice matrix J . The six velocity directions along the cartesian co-ordinate and the one stationary velocity at the centre is expressed in Eq. 4.

$$J = \begin{bmatrix} 1 & -1 & 0 & 0 & 0 & 0 & 1 & 1 & 1 & 1 & -1 & -1 & -1 & -1 & 0 & 0 & 0 & 0 & 0 \\ 0 & 0 & 1 & -1 & 0 & 0 & 1 & -1 & 0 & 0 & 1 & -1 & 0 & 0 & 1 & 1 & -1 & -1 & 0 \\ 0 & 0 & 0 & 0 & 1 & -1 & 0 & 0 & 4 & -1 & 0 & 0 & 1 & -1 & 1 & -1 & 1 & -1 & 0 \end{bmatrix} \tag{4}$$

The geometry of 3D lattice D3Q19 is illustrated in Fig.1. The local density (Eq. 5) at a lattice point can be derived by summing the mass distribution function f :

$$\rho(k,t) = \sum_{i=0}^{18} f_i(k,t) \tag{5}$$

The local streaming velocity $v(k, t)$ can be obtained from the following expression (Eq. 6):

$$v(k,t) = \frac{\sum_{i=0}^{18} C_i \cdot f_i(k,t)}{\rho(k,t)} \tag{6}$$

The single-particle distribution for any lattice model at lattice node k is given by the Boltzmann equation (Eq. 7) for time evolving mass distribution function $f(k, t)$:

$$f(k + C_i, t + 1) = f_i(k, t) + \Omega(f(k, t)) \tag{7}$$

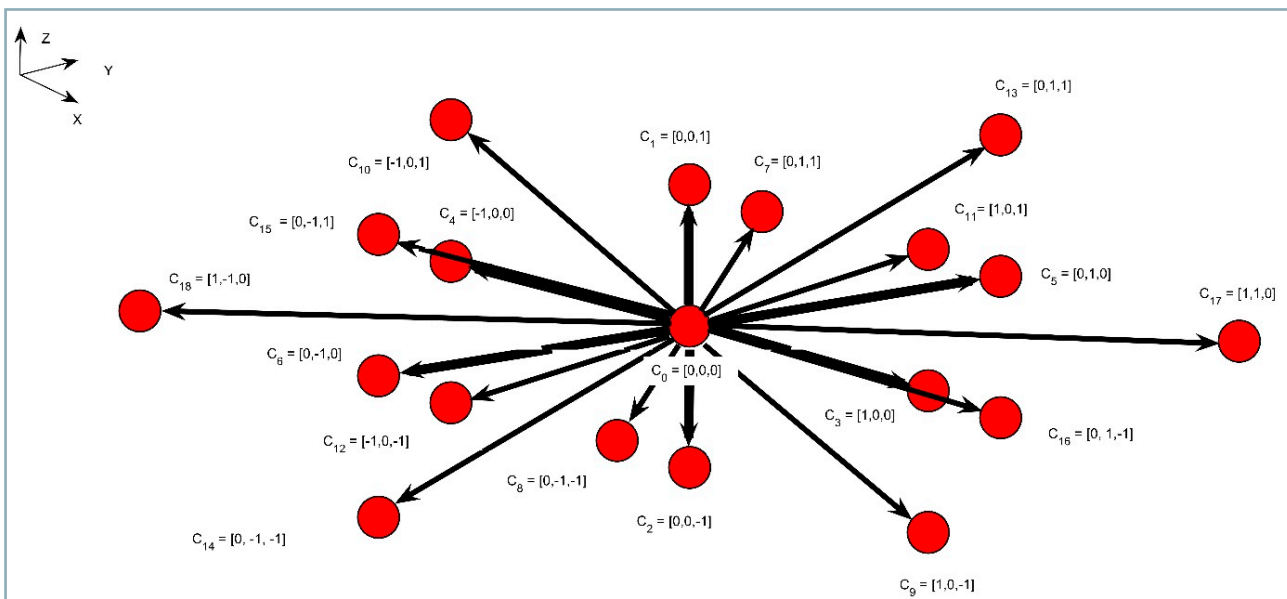


Fig. 1 Geometry of the D3Q19 with distinct lattice velocities ($C_i, i = 0, 1, 2, \dots, 18$)

There are also several assumptions related to the LBM that must be known before applying it to the macroscopic scale. Some of them are: external forces are neglected; movement of the particles take place only along the lattice vectors; the single relaxation time approximation for BGK; modelling of the fluid by numerous cells having the same type; updating the cells at each time step; and storage of the number of particles that move along each of the lattice vector particle distribution functions. However, there are also MRT (multiple-relaxation time) approximations. For the given issue, the air trapped at discontinuity must be displaced by a hypothetical fluid node so that the fluid flow properties can be correlated to the rate of change of the remaining mass fraction, which, in a physical system, is a vertical height of the TG plane. Such a system transforms the issue into two-fluid model. In the current scenario, the orange balls represent the fluid elements and the white dots on the TG plane represent the air void (Fig. 6). It is assumed that the plane is non-fluidizable, thus the behaviour of fluid along the plane predicts the same behaviour as the remaining mass fraction. The indicator function ζ is used to determine whether air void is replaced by a fluid node or not.

$$\zeta(k) = \begin{cases} 1, & \beta(k, t) \geq 1, \\ 0, & \beta(k, t) \leq 0, \\ 0.5(\sin(\pi(\beta(k, t) - 0.5)) + 1), & 0 < \beta(k, t) < 1 \end{cases} \quad (8)$$

$$\text{Here } \beta(k, t) = \sum_{i=0}^{18} \beta_i(k, t).$$

The indicator function $\zeta(k) = 1$ if the fluid node replaces the air void, else $\zeta(k) = 0$. On the TG plane boundary ($0 < \beta(k, t) < 1$), the indicator function has the sinusoidal behaviour (Eq. 8). So, similarly, for air void, the equation of collision step can be represented by Eq. (9):

$$\beta(k + C_r, t + 1) + \eta_\beta(\beta_i(k, t) - \beta_i^{eq}(k, t)) = \beta_i(k, t) \quad (9)$$

where:

η_β – relaxation parameter

$\beta_i^{eq}(k, t)$ – equilibrium function, which can be given by the following expression:

$$\beta_i^{eq}(k, t) = \frac{\beta_i(k, t) f_i(k, t)}{\rho} \quad (10)$$

The parameter $\eta(k, t)$ helps in determining diffusivity of momentum between various layers of fluid and at each time step, it depends upon the value of indicator function $\zeta(k)$:

$$\eta(k, t) = \zeta(k) \eta_f(k, t) + (1 - \zeta(k)) \eta_a(k, t) \quad (11)$$

where:

η_f, η_a – relaxation parameters for hypothetical fluid and air respectively

The rate of change of mass fraction of fluid along the plane is:

$$\frac{dx}{dt} = \frac{\int_s [\rho(k, t) v(k, t) \hat{n}] ds}{1,642,346.626\rho_f} \approx \frac{\sum_{k=1}^N \rho(k, t) v(k, t) \delta s}{1,642,346.626\rho_f} \quad (12)$$

where:

\hat{n} – unit vector normal to the surface area of TG plane

N – number of fluid particles settle on the TG plane

Integrating Eq. 12 with respect to 't', we have

$$X_f \approx \frac{\left(\sum_{k=1}^N \rho(k, t) v(k, t) \delta s \right) \delta t}{1,642,346.626\rho_f} \quad (X_f - \text{mass fraction of fluid on the plane}).$$

$$\text{Here, } v = \left(v_x^2 + v_y^2 + v_z^2 \right)^{\frac{1}{2}}.$$

$$\rho v_x = f_1 + f_7 + f_8 + f_9 + f_{10} - (f_2 + f_{11} + f_{12} + f_{13} + f_{14}) \quad (13)$$

$$\rho v_y = f_3 + f_7 + f_{11} + f_{15} + f_{16} - (f_4 + f_8 + f_{12} + f_{17} + f_{18}) \quad (14)$$

$$\rho v_z = f_5 + f_9 + f_{13} + f_{15} + f_{17} - (f_6 + f_{10} + f_{14} + f_{16} + f_{18}) \quad (15)$$

Multi-reaction model for hardwood pyrolysis

For correlating of the fluid flow with the thermogravimetric behaviour of hardwood, an interface is required to derive the relevant parameters related to the pyrolysis of biomass. Distributed Activation Energy Model (DAEM) is adopted to find the inverse solution of the given issue. To obtain a realistic solution, it is necessary to know the parameters that affect the model solution. Comprehensive information on various parameters of the non-isothermal n^{th} order is reported by Brown (1988). The basic assumptions and their derivations can be found in Dhaundiyal and Tewari (2017); Dhaundiyal and Singh (2019); Burnham (2017). The non-isothermal n^{th} DAEM are as follow:

the first order reaction:

$$X = \int_0^\infty \exp\left(\int_0^t -A \exp\left(-\frac{E}{RT}\right) dt\right) f(E) dE \quad (16)$$

the n^{th} order:

$$X_n = \int_0^\infty \left\{ 1 - (1-n) \int_0^t A \exp\left(-\frac{E}{RT}\right) dt \right\}^{\left(\frac{1}{1-n}\right)} f(E) dE \quad (17)$$

where:

E – activation energy

A – pre-exponential factor

R – ideal gas constant

n – reaction order

t – time

X – remaining mass fraction of releasing volatiles

$f(E)$ – density function of activation energies, which is usually represented by the stochastic models

Many stochastic models have been used to determine the relevant kinetic parameters, but the most reliable model is Rayleigh distribution and Gaussian distribution (Dhaundiyal and Tewari, 2017; Dhaundiyal and Singh, 2020; Dhaundiyal and Toth, 2020). The redundant distribution parameters cause over-fitting of model, which is difficult to interpret within the desirous range; therefore, the study is focussed on the simplest form of density function, i.e. the Gaussian distribution, which was primarily used in coal

pyrolysis (Serio et al., 1987) and later became very popular in the DAEM for modelling thermochemical processes (Galgano and Blasi, 2003). The Eqs. 12 and 13 have no analytical solution; therefore, it is required to approximate the double integral form of remaining mass fraction variation with time and temperature. The Laplace integral method (Dhaundiyal et al., 2019; Dhaundiyal and Toth, 2019) is used to obtain the approximation for double exponential term and double integral form. The basic notion behind using the Laplace integral method is to transform both the functions into a single dimensionless variable so that it becomes easier to tackle the multi-variable problem. To approximate multi-reaction model, the activation energy is rescaled by using the scaling factor y , whereas the corresponding energy correction factor (y) for the double exponential term is denoted by y_s and y_w . The subscript 's' and 'w' denotes the mean and step width of the activation energy. It implies the activation energy varies around mean values with step size of y_w .

$$y = \frac{E}{E_0}$$

where:

E_0 – the mean value of activation energy

Eq. 16 can be rewritten as a combination of two functions:

$$X = \int_0^\infty H(T, t) \cdot f(y) dy$$

where:

$H(T, t) = \exp\left(\int_0^t -A \exp\left(-\frac{E}{RT}\right) dt\right)$ – double exponential term

$f(y) = \frac{1}{E_0} \sqrt{\frac{\Psi}{\pi}} \exp(\Psi(y-1)^2)$ – Gaussian distribution function

of scale factor ' y ' · $\Psi = \frac{E_0^2}{2\sigma^2}$ is the constant parameter

σ^2 – variance of the distribution function

The function $H(T, t)$ can be approximated as:

$$H(T, t) = \exp\left(\frac{-ARTt}{E} \exp\left(\frac{-E}{RT}\right)\right) \text{ as } \frac{E}{R} \rightarrow \infty \quad (18)$$

The exponent of exponential term $\left(\frac{-ARTt}{E} \exp\left(\frac{-E}{RT}\right)\right)$

exp in Eq. 13 can be rewritten as:

$$H(T, t) = \exp\left(-\exp\left(\frac{E_s - E}{E_w}\right)\right) \quad (19)$$

Since the exponent of exponential term behaves like a step function where E varies around the mean value E_s with step size of E_w , it is necessary to determine the behaviour of E around neighbourhood of E_s . The significance of double exponential function $H(T, t)$ can be understood by varying the value of E . The function is nearly one for all the values E greater than E_s , whereas the function approaches zero for the values of E lower than E_s . In other words, the contribution of double exponential term in the DAEM can be known only if the boundaries of activation energy domain are defined.

$$\text{Let } S(E) = \left(\frac{E_s - E}{E_w}\right).$$

Apply Taylor series expansion on $S(E)$ around $E = E_s$.

$$S(E) = S(E_s) + (E - E_s) S'(E_s) + \dots \quad (20)$$

The boundary conditions at $E = E_s$ are $S(E_s) = 0$ and $S'(E_s) = -\frac{1}{E_w}$.

After solving Eqs. 18; 19; and 20, we get:

$$E_s = RT \cdot W(A \cdot t) \text{ and } E_w = \frac{E_s}{E_s + RT}$$

where:

$W(A \cdot t)$ – the Lambert W function

Thus, the Eq. 16 becomes:

$$X = \int_0^\infty \exp\left(-\exp\left(\frac{y_s - y}{y_w}\right)\right) \cdot \sqrt{\frac{\Psi}{\pi}} \exp(\Psi(y-1)^2) dy \quad (21)$$

Applying Laplace asymptotic method to Eq. 21, we will get:

$$X_{n=1} \sim \frac{\exp(-\Psi(y_e - 1)(y_e + 2y_w - 1))}{\sqrt{1 + \left(\frac{y_e - 1}{y_w}\right)^2}} \quad (22)$$

where:

y_e – location where the integrand (Eq. 21) has a maximum value:

$$y_e = 1 + y_w \cdot W\left(\frac{1}{2\Psi y_w^2} \exp\left(\frac{y_s - 1}{y_w}\right)\right)$$

Similarly, for the n^{th} order, we have:

$$X_{n \neq 1} \sim 1 - \frac{1}{\sqrt{2\Psi}} \left[\exp(-y(y_{e,n} - 1)(2y_s - y_{e,n} - 1)) + \frac{n}{2} \exp(-y(y_{e,n} - 1)(2y_s - y_{e,n} - 1)) \right] \quad (23)$$

where:

$$y_{e,n} = 1 - \frac{1}{2\Psi y_w}$$

Eqs. 22 and 23 are the required expressions.

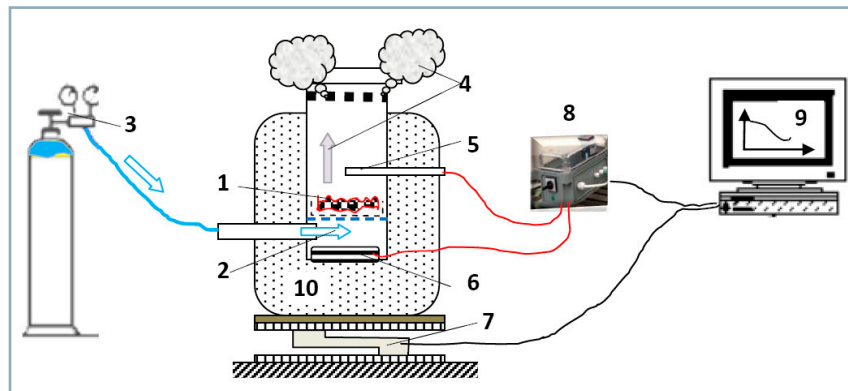
Experimental setup

A pilot size reactor has been used to test the hardwood chip (G50). The raw material, hardwood (Acacia), has been gathered in Pest county of Hungary. The processed raw material has been obtained by shredding the billet of wood. The properties of thermodynamic system – pressure and temperature – have been measured using pressure and temperature sensors placed inside the main chamber. Temperature sensor has been located 80 mm from the

Table 1 Ultimate analysis of hardwood (Acacia) (dry basis)

| C (%) | H (%) | N (%) | O (%) | S (%) | Ash (%) | Cl (%) | Energy density (GJ·m ⁻³) | N.C.V (MJ·kg ⁻¹) |
|-------|-------|-------|--------|-------|---------|--------|--------------------------------------|------------------------------|
| 50.03 | 5.849 | 0.075 | 42.947 | 0.061 | 1.037 | 0.02 | 10.88 | 18.70 |

* N.C.V – net calorific value

**Fig. 2** Schematic diagram of the pyrolysis unit

1 – grate; 2 – nozzle; 3 – regulating valve; 4 – pyrolysis gas; 5 – temperature sensor (Nickel-Chromium/Nickel-Alumel); 6 – pressure sensor; 7 – weight sensor; 8 – data logger; 9 – processing unit; 10 – mineral wool insulator

reactor base, while the pressure sensor has been at reactor base. The inert gas, nitrogen, has been allowed to flow at volumetric rate of 70 mL·s⁻¹. The 'K' type ((Nickel-Chromium/Nickel-Alumel) thermocouple has been used to measure the sample temperature. The weight sensor has been placed beneath the heating chamber separated from the mineral wool covering. The indirect heating has been provided by a heating element of 2 kW_e (Hertz, Germany). The grate has been made up of 0.7 mm stainless steel, whereas the heat resisting material – rock wool – has been used to separate reactor from the outer casing. Reactor core has been made of 1.5 mm welded carbon steel. The inner reactor diameter has been 110 mm; the reactor surface diameter – 210

mm. The schematic diagram of pilot size pyrolysis unit is illustrated in Fig. 2. Elemental composition of the raw material has been measured by CHNS analyser (vario MACRO cube, Germany). The calorific value of hardwood has been obtained using the bomb calorimeter at constant volume. The ultimate analysis of hardwood (Acacia) is shown in Table 1.

Results and discussion

To calculate the kinetic parameters of biomass pyrolysis, the concept of percolation is used. The process is exactly the same as making the Moka coffee in a Moka pot, except in place of kettle, a mathematical plane has been used as a perforated filter to

allow the hypothetical fluid to seep through the discreet boundaries. The plane used for demonstration is the thermogravimetric plane (TG), which is obtained by pyrolysis of G50 hardwood (Acacia) chips in a pilot-size reactor.

In order to correlate this physical event to the chemical process, the principle of lattice gas is used. The LBM is used as a mathematical interface to introduce the kinematics of fluid element. The D3Q19 (three-dimensional model with 19 lattice velocities) has been adopted to understand the mesoscopic process. To simplify the calculation, the boundaries are not fluidised with flow; therefore, the biomass nodes are intact throughout the process. The fraction of fluid on the outer surface of TG thermogram has a common mathematical solution, as it is obtained through multi-reaction model. In other words, the rate of displacement of fluid element is proportional to the rate of change of biomass fraction in a pyrolysis reactor. Since the volatile and water content flows through the porous wood chips, the physical phenomenon of fluid flow can be correlated to the chemical kinetics. The temperature and pressure variation at the bed are illustrated in Fig. 3. Both system properties vary exponentially, except pressure shows a sudden jump due to changing regime of the fixed bed with respect to superficial velocity of pyrolysis gas. The thermogravimetric behaviour of hardwood chip is illustrated in Fig. 4a. Certain notches or small peaks, which are more perceptible in TGA analyser, in the TG curve obtained from Industrial reactor (Fig. 4b and Fig. 9) show decomposition stages of hardwood. The fluid elements are generated through the MATLAB and the volume enclosed by the TG plane (Fig. 4b) is obtained with the help of the Monte-Carlo method. The numerical solution of the prosed LBM is determined by using

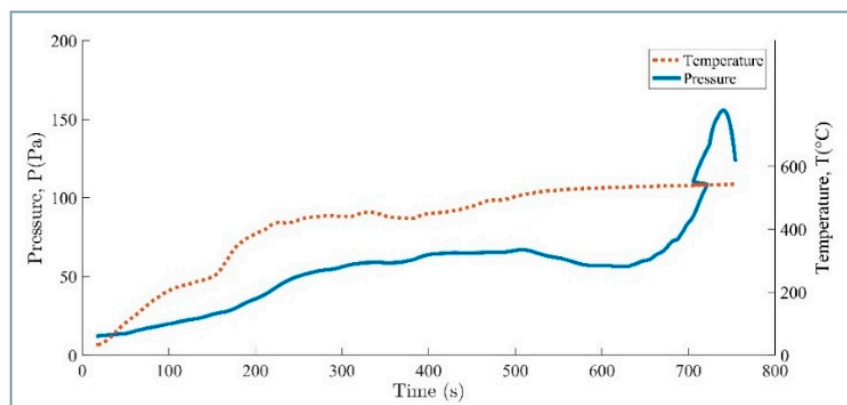
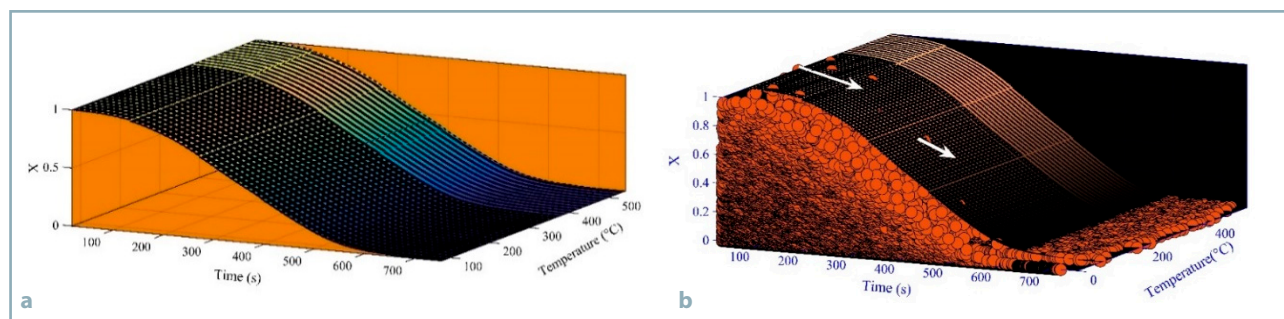
**Fig. 3** Temperature and pressure variation across the pyrolysis reactor

Table 2 Comparison of kinetic parameters obtained from different methodologies

| Parameters | LBM | | Monte Carlo (Dhaundiya et al., 2019) | Model-free (Wilk et al., 2017) | Model-fitting (Oluoti et al., 2014) |
|------------|---|---|---|---|---|
| | $n=1$ ($R^2 = 0.98$) | $n=2$ ($R^2 = 0.33$) | | | |
| \bar{E} | 190.49 kJ·mol ⁻¹ | 7.24 kJ·mol ⁻¹ | 35.92 kJ·mol ⁻¹ | 180 kJ·mol ⁻¹ | 95.41 kJ·mol ⁻¹ |
| \bar{A} | 1.93×10^{41} min ⁻¹ | 8.1×10^{25} M ⁻¹ ·min ⁻¹ | 1.06×10^4 min ⁻¹ | 1.15×10^{11} min ⁻¹ | 3.20×10^{12} min ⁻¹ |
| E_{\min} | 8.44 kJ·mol ⁻¹ | 4.22 kJ·mol ⁻¹ | 15 kJ·mol ⁻¹ | 125.29 kJ·mol ⁻¹ | 79.23 kJ·mol ⁻¹ |
| E_{\max} | 967 kJ·mol ⁻¹ | 63.24 kJ·mol ⁻¹ | 60 kJ·mol ⁻¹ | 226.75 kJ·mol ⁻¹ | 142.87 kJ·mol ⁻¹ |

Table 3 Modelling parameters related to thermokinetics of Hardwood pyrolysis

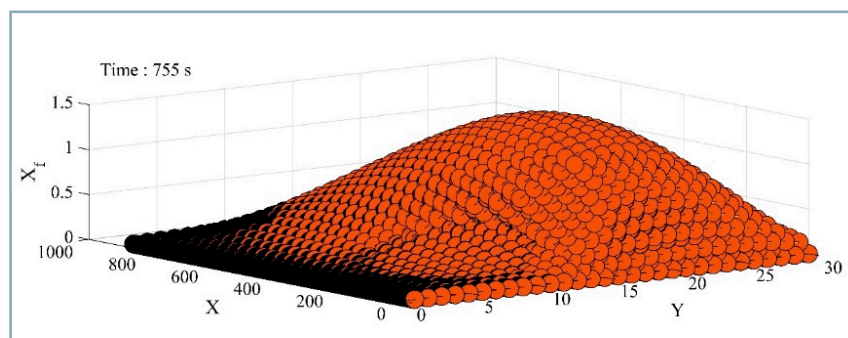
| Parameter | First order | Second order |
|-----------|---|---|
| E_s | 0.24–492.92 kJ·mol ⁻¹ | 2.40–61 kJ·mol ⁻¹ |
| E_w | 0.13–3.75 kJ·mol ⁻¹ | 1.44–6.1 kJ·mol ⁻¹ |
| A | 0.00375– 4.4×10^{57} min ⁻¹ | 0.01086– 5.43×10^{26} M ⁻¹ ·min ⁻¹ |

**Fig. 4** (a) Thermogravimetric (TG) plane for the G50 wood chip; (b) Percolation of fluid element across the thermogravimetric (TG) plane

the iterative method. The distribution functions are obtained for each node (i) and its summation provided the mass density of fluid element at each node. The velocity of fluid is derived with sum of product of distribution function and the lattice velocities. On the basis of obtained solution, the mass fraction of fluid element on the surface is shown in Fig. 5. The fraction of generated fluid passed through plane is found to be 91% of total generated fluid element. The resultant distribution is negatively skewed, inferring the majority of mass density of fluid element gets shifted

to the higher temperature regime. The velocity field in terms of orthographic view at different time scale is illustrated in Fig. 6. It shows that the volumetric influx of fluid element is monumentally high at onset of simulation ($t = 2$ s). As time proceeds, the ingress of fluid element through porous medium gets subdued. The white porosity indicates discontinuity of plane, which is preoccupied with air. The air is assumed to be stagnant, thus its effect on simulation is absent. The governing equation for remaining mass fraction of biomass is represented by

distributed activation energy model. The relevant parameters related to biomass pyrolysis are derived by inverse formulation ($g(\theta, E, A) = f^1(X_n)$). The heating rate is found to be 53.78 °C·min⁻¹, whereas the pre-exponential factor varies from 0.00375 min⁻¹ to $4.4e + 57$ min⁻¹ for the first order reaction. The activation energy varies from 8.44 kJ·mol⁻¹ to 947 kJ·mol⁻¹. On the other hand, its average value is estimated to 190.49 kJ·mol⁻¹. The results for the first order reactions are compared with the data obtained for same kind of hardwood (Dhaundiya et al., 2019; Wilk et al., 2017; Oluoti et al., 2014) and it is found that the variation of activation energies, derived through model-free and model-fitting methodologies, fall within the range of solution estimated by the proposed scheme. To verify the potential existence of other solutions, the scheme is applied to higher order reactions, and the range of solution for activation energy – E (kJ·mol⁻¹) – lies in the closed interval of $4.32 \leq E \leq 63.24$,

**Fig. 5** Distribution of mass fraction (X_f) on the TG surface

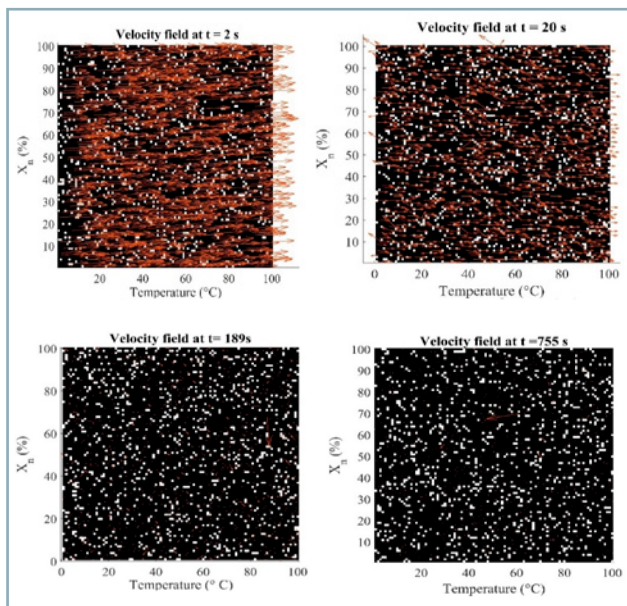


Fig. 6 Orthogonal projection of TG plane on the Y-Z plane (temperature scale: 1 scale unit = 5.4316 °C)

whereas the obtained average value is 7.322 kJ·mol⁻¹. The detailed parametric information is provided in Tables 2 and 3. In the DAEM, the double exponential term is approximated by using stepwise variation of activation energy with the step size of E_w . The range of central value (E_s), around which E varies, falls in the closed interval of 0.24–492.92 kJ·mol⁻¹, whereas the step-width (E_w) varies from 0.13 to 3.75 kJ·mol⁻¹. To understand the relative significance of double exponential term with respect to distribution function of activation energy ($f(E)$), the graphical plot is

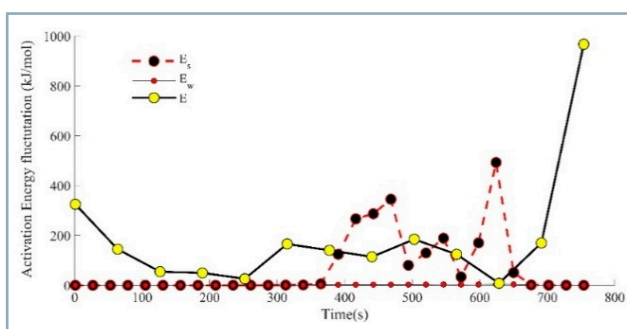


Fig. 7 Activation energy (E , E_s , E_w) variation with respect to time

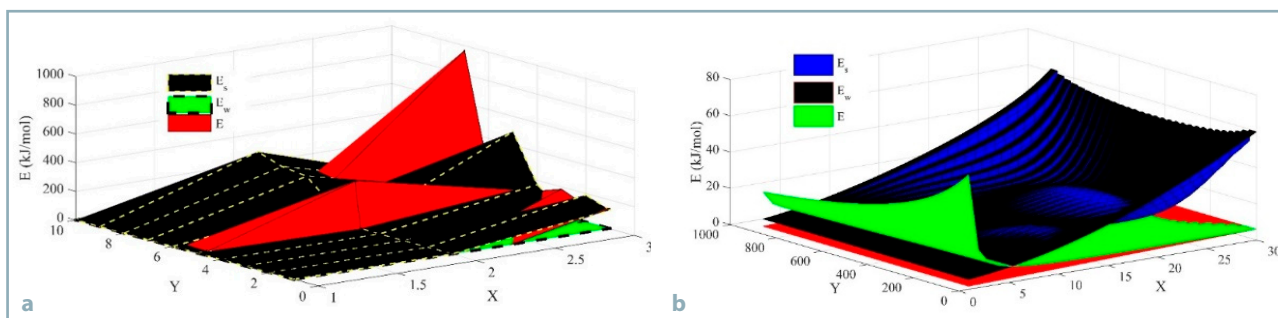


Fig. 8 (a) Relative variation of E with respect to E_s and E_w ($n = 1$); (b) Relative variation of E with respect to E_s and E_d ($n = 2$)

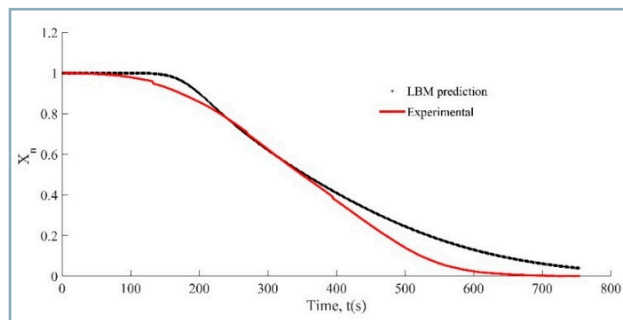


Fig. 9 Comparative sketch of predicted solution of the LBM ($n = 1$) and experimental result

drawn between activation energies and time (Fig. 7). The double exponential term has no significant role at onset of pyrolysis process. It merely affects the devolatilisation and char formation of biomass, whereas the attribute of mass-loss curve of biomass at the beginning is guided by density function of activation energy. Therefore, it can be concluded that the double exponential function plays a vital role in thermokinetics, when the activation energy reaches its local minima in its interval. It can be more clearly understood by the surface plot (Fig. 8a) that the surface gradient of E is relatively high in the beginning, whereas, with time, it decreases until it reaches the lowest point. Simultaneously, the temperature integral or double exponential function has its maximum gradient. Unlike the first order reaction, higher order reactions are predominately governed by the rate constant. An illustrative plot of activation energy variation across the plane is shown in Fig. 7b. It shows that the integrand is guided by the rate constant $\left(A \exp\left(-\frac{E}{RT}\right) \right)$

throughout the process, except at the beginning of the thermochemical conversion. The central value E_s varies from 13 to 61 kJ·mol⁻¹, while the step size E_w is in the range of 1.44–6.1 kJ·mol⁻¹. Mathematically, as the activation energies exceed E_s , the temperature integral will approach its global maxima; whereas, for all the values of E at neighbourhood of E_s , the temperature integral will vary between 0 and 1, but it is the other way round for higher order reactions. According to the thermokinetic behaviour, the rate constant depends on T and E and it attains its maximum value in the temperature range of 250–280 °C for hardwood pyrolysis, implying the temperature integral function has its significant effect in the given range for the first order reaction. Furthermore, it attains its local maxima at

280–290 °C, 420 °C and 473–490 °C, so the slowest reaction step has insignificant impacts on the distribution pattern of activation energies and vice versa. Pyrolysis of hardwood shows its major product yield at the temperature range of 250–280 °C, 314–350 °C and 437–455 °C, while pressure will vary between 50 and 75 Pa. To predict the LBM scheme graphically, a comparative plot is drawn which precisely correlates the simulated values with the experimental curves. The solution obtained for the second order reaction has the least consistency with the experimental data, implying the hardwood pyrolysis highly favours the first order reaction or the reactions which are very near to the first order reactions.

Conclusions

The proposed scheme is successfully implemented to pyrolysis problem of biomass. It is found that the obtained solution comes within the domain of solution derived from other kinetic models. The ingress of fluid element and dispersion of fluid element on the surface of the TG plane is assumed to be part of governing DAEM equation. The fluid mass distribution is estimated to be negatively skewed on the TG surface. The velocity field is obtained at a different time scale and the fluid influx is relatively high at the beginning, which gets subdued with the time. The derived fraction of fluid mass is assumed to be part of the DAEM equation, and based on this assumption, the kinetic parameters are determined. The range of activation lies in the range of 8.44–967 kJ·mol⁻¹. On the other hand, the solution is also derived for higher – order reactions to know chemical reaction pathway of hardwood pyrolysis. The activation energy for the second reaction varies in the domain of 4.22–63.24 kJ·mol⁻¹. The estimated value of the pre-exponential factor for the first reaction order is estimated to 1.93 × 1,041 min⁻¹. The rate of reaction attains its maximum value in the temperature range of 280–290 °C. It is to be noted that the inverse formulation requires that the function must not be surjective, else the function will not exist. It implies a kinetic parameter must be unique in nature.

Apart from the evaluation of the kinetic parameters based on a hypothetical fluid medium, the percolation concept can be implemented to the simulation of the gas flow in several kinds of power generation plants.

References

- BHATNAGAR, P. L. – GROSS, E. P. – KROOK, M. 1954. A model for collision processes in gases. I. Small amplitude processes in charged and neutral one-component systems. In *Physical Review*, vol. 94, no. 3, pp. 511–525.
- BROWN, M. E. 1988. *Introduction to Thermal Analysis: Techniques and Applications*. London and New York (Chapman and Hall), 1988.
- BURNHAM, A. K. 2017. *Introduction to chemical kinetics*. In *Global Chemical Kinetics of Fossil Fuels*, pp. 25–74.
- DHAUNDIYAL, A. – SINGH, S. B. 2019. Stochastic analysis of multi-reaction model for non-linear thermal history. In *Acta Technologica Agriculturae*, vol. 22, no. 3, pp. 91–97.
- DHAUNDIYAL, A. – SINGH, S. B. – ATSU, D. – DHAUNDIYAL, R. 2019. Application of Monte Carlo simulation for energy modeling. In *ACS Omega*, vol. 4, no. 3, pp. 4984–4990.
- DHAUNDIYAL, A. – SINGH, S. B. 2020. The generalisation of a multi-reaction model for polynomial ramping of temperature. In *J Therm Anal Calorim*. <https://doi.org/10.1007/s10973-020-09650-7>
- DHAUNDIYAL, A. – TEWARI, P. 2017. Kinetic parameters for the thermal decomposition of forest waste using distributed activation energy model (DAEM). In *Environmental and Climate Technologies*, vol. 19, no. 1, pp. 15–32.
- DHAUNDIYAL, A. – TOTH, L. 2019. Modelling of hardwood pyrolysis using the convex combination of the mass conversion points. In *Journal of Energy Resources Technology*, vol. 142, no. 6, pp. 061901–061910.
- DHAUNDIYAL, A. – TOTH, L. 2020. Modeling of Hardwood Pyrolysis Using the Convex Combination of the Mass Conversion Points. In *Journal of Energy Resources Technology, Transactions of the ASME*. doi: 10.1115/1.4045458.
- GALGANO, A. – DI BLASI, C. 2003. Modeling wood degradation by the unreacted-core-shrinking approximation. In *Industrial and Engineering Chemistry Research*, vol. 42, no. 10, pp. 2101–2111.
- GIUPPONI, G. – HARTING, J. – COVENEY, P. V. 2006. Emergence of rheological properties in lattice Boltzmann simulations of gyroid mesophases. In *Europhysics Letters*, vol. 73, no. 4, pp. 533–539.
- GUO, Z. – ZHAO, T. S. – SHI, Y. 2006. Physical symmetry, spatial accuracy, and relaxation time of the lattice Boltzmann equation for microgas flows. In *Journal of Applied Physics*, vol. 99, no. 7, p. 074903.
- HABICH, J. – ZEISER, T. – HAGER, G. – WELLEIN, G. 2011. Performance analysis and optimization strategies for a D3Q19 lattice Boltzmann kernel on nVIDIA GPUs using CUDA. In *Advances in Engineering Software*, vol. 42, no. 5, pp. 266–272.
- HARTING, J. – HERRMANN, H. J. – BEN-NAIM, E. 2008. Anomalous distribution functions in sheared suspensions. In *Europhysics Letters*, vol. 83, no. 3, p. 30001.
- HECHT, M. – HARTING, J. 2010. Implementation of on-site velocity boundary conditions for D3Q19 lattice Boltzmann simulations. In *Journal of Statistical Mechanics: Theory and Experiment*, vol. 2010, no. 1, p. 01018.
- HUANG, H. – KRAFCHYK, M. – LU, X. 2011. Forcing term in single-phase and Shan-Chen-type multiphase lattice Boltzmann models. In *Physical Review E - Statistical, Nonlinear, and Soft Matter Physics*, vol. 84, no. 4.
- KUTAY, M. E. – AYDILEK, A. H. – MASAD, E. 2006. Laboratory validation of lattice Boltzmann method for modeling pore-scale flow in granular materials. In *Computers and Geotechnics*, vol. 33, no. 8, pp. 381–395.
- LI, L. – MEI, R. – KLAUSNER, J. F. 2013. Boundary conditions for thermal lattice Boltzmann equation method. In *Journal of Computational Physics*, vol. 237, pp. 366–395.
- NEKOVEE, M. – CONEVEY, P. V. – CHEN, H. – BOGHOSIAN, B. M. 2000. Lattice-Boltzmann model for interacting amphiphilic fluids. In *Physical Review*, vol. E62, no. 6 B, pp. 8282–8294.
- OLUOTI, K. – DODDAPANENI, T. R. K. – RICHARDS, T. E. – KANAGASABAPATHI, D. 2014. Evaluation of the pyrolysis and gasification kinetics of tropical wood biomass. In *BioResources*, vol. 9, no. 2, pp. 2179–2190.
- SERIO, M. A. – HAMBLEN, D. G. – MARKHAM, J. R. – SOLOMON, P. R. 1987. Kinetics of volatile product evolution in coal pyrolysis: Experiment and theory. In *Energy and Fuels*, vol. 1, no. 2, pp. 138–152.
- WILK, M. – MAGDZIARZ, A. – GAJEK, M. – ZAJEMSKA, M. – JAYARAMAN, K. – GOKALP, I. 2017. Combustion and kinetic parameters estimation of torrefied pine, acacia and Miscanthus giganteus using experimental and modelling techniques. In *Bioresource Technology*, vol. 243, pp. 304–314.



Acta Technologica Agriculturae 2
Nitra, Slovaca Universitas Agriculturae Nitriae, 2020, pp. 81–86

RECYCLED GREEN PE COMPOSITES REINFORCED WITH WOVEN AND RANDOMLY ARRANGED SISAL FIBRES PROCESSED BY HOT COMPRESSION MOULDING

Bruno Dorneles de CASTRO*, Paulo Eustáquio de FARIA, Luciano Machado Gomes VIEIRA, Claudia Victoria CAMPOS RUBIO, Rômulo MAZIERO, Paulo César de Matos RODRIGUES, Juan Carlos CAMPOS RUBIO

Federal University of Minas Gerais, Brasil

Green plastics are constantly being used to minimize the negative impacts of the polymers made of fossil fuels such as petroleum. Non-renewable petroleum-based products are employed in wide range of human activities, yet plastic waste accumulation represents a serious issue for the environment (Mohd Rafee et al., 2019). On the other hand, the use of natural fibres in composite materials, such as sisal fibres, in substitution for synthetic fibres, has increased considerably. The aim of this study was to develop a low-cost manufacturing process of composites with reuse of polyethylene bags made of sugarcane ethanol (green polyethylene) reinforced with sisal fibres. The hot compression moulding (185 °C) was used to mould composite structural board. Tensile tests were conducted to evaluate the influence of the reinforcement configuration on the mechanical properties of the composites, considering two arrangements: woven fibres in (0°/90°) and randomly arranged. The results indicated that the use of woven sisal fibres in (0°/90°) as reinforcement of the green HDPE showed an increase in the tensile strength (33.30%) in contrast to the pure traditional HDPE. Randomly arranged sisal fibre-reinforced green HDPE composites showed higher modulus of elasticity than pure traditional HDPE (76.83%). Composites with woven sisal fibres showed higher values for tensile strength and ultimate strain, and lower modulus of elasticity than composites with randomly arranged sisal fibres. In addition, failure modes of the composites were observed. The results showed the viability of producing these composites by the developed equipment and the potential use of these materials as structural components.

Keywords: sustainability; biopolymers; waste plastic; natural fibre

In recent years, aligning composite materials production with sustainable guidelines has been the focus of many studies. The sustainable use of natural resources can be applied to various stages of a product's life cycle, since the extraction and manufacturing to disposal and recycling (Akinyemi et al., 2016). Plati (2019) argues that the concept of sustainability is based on a balance among the economic, environmental and social spheres and that this should be considered an important aspect for humanity, especially with regard to climate change on the planet, as over time.

Within this context, the reuse or the recycling of plastic waste is one of the ways to minimize the environmental impacts generated by the inappropriate disposal. From the environmental view, the economic aspect of this process is emphasized, since plastics have high added value. Thermoplastics, such as PE, are the most used for recycling and are widely applied in engineering (Ahmad and Luyt, 2012).

Polyethylene produced from sugarcane ethanol is called green polyethylene (green PE) because it is produced from renewable source. It is considered an innovative polymer that captures and fixes carbon dioxide from the atmosphere during its production and does not release it back to the environment during its life cycle, contributing to the

reduction of greenhouse gases (GHG), as shown in Fig. 1. In addition, green PE is recyclable within the same supply chain as traditional polyethylene (Guilhen et al., 2017).

Moreover, the use of natural fibres instead of synthetic fibres in composite materials has been widely investigated in the last decade. Natural fibres have advantages such as low weight and low cost, and have a renewable nature, they can decompose in a few months, unlike synthetic fibres, which usually decompose many years (Chattopadhyay et al., 2011).

As one of the main uses of natural fibres in terms of the reinforcement of plastics and rubbers stand out increasing quality and commercial application. Sisal fibre-reinforced composites have been more used recently in the automotive and aerospace industries (Choudhury, 2008). Fávoro et al. (2010) evaluated the composites made of post-consumed high-density polyethylene (HDPE) reinforced with short sisal fibres (10% in weight) and achieved improvements in the modulus of elasticity (approx. 16%) in contrast to pure HDPE. Zhao et al. (2014) investigated the mechanical properties of randomly arranged sisal fibre-reinforced HDPE composites and found an increase in the modulus of elasticity (88.9%) when added 20% of fibres in weight, which showed the applicability of these fibres. Table 1 shows the mechanical

Contact address: Bruno Dorneles de Castro, Federal University of Minas Gerais, Post-Graduate Programme in Mechanical Engineering, Brasil; e-mail: bdc2016@ufmg.br

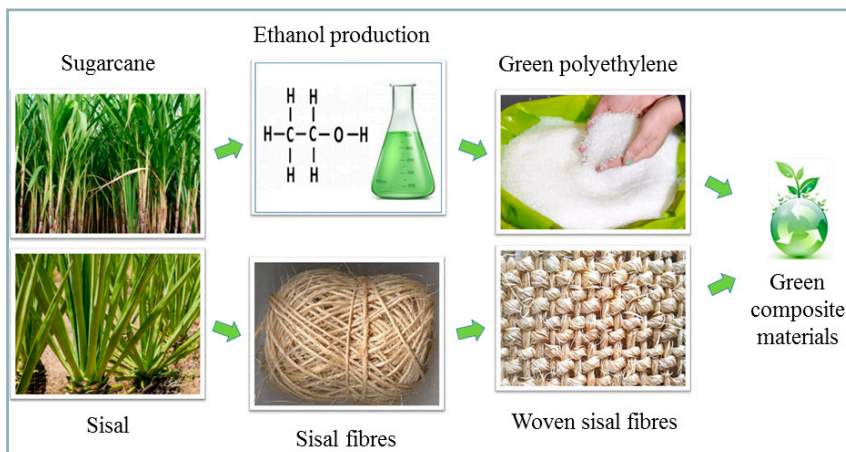


Fig. 1 Production of a woven sisal fibre-reinforced green polyethylene composite

Table 1 Mechanical properties of sisal fibre

| Density (kg·m ⁻³) | Diameter (µm) | Tensile strength (MPa) | Modulus of elasticity (GPa) | Ultimate strain (%) |
|-------------------------------|---------------|------------------------|-----------------------------|---------------------|
| 1,030–1,450 | 50–300 | 346–700 | 7–22 | 2.2–14 |

properties of sisal fibre according to Ibrahim et al. (2016).

In order to show a possible application of these composites in structural products, this work aimed to develop a low-cost manufacturing process of green composite materials using reused polyethylene bags and sisal fibres as reinforcement (Fig. 1). The values of tensile strength, modulus of elasticity and ultimate strain were obtained by tensile tests (ASTM D638, 2014).

Material and methods

High-density polyethylene (HDPE) obtained from reused polymeric bags, and sisal fibres were used for the production of composite boards. They were produced from traditional

and green (renewable source, made of sugarcane ethanol) discarded post-consumer HDPE.

Sisal fibres were purchased from the company Sisalsul Indústria e Comércio Ltda (SP, Brazil). Sisal production is concentrated in semi-arid regions, such as southern Bahia (Brazil), where the cultivation of the plant ensures the survival of several small farmers promoting the social and economic development of the region (Santos et al., 2014). There was no chemical treatment of the materials used in this study in order to strengthen the sustainable character of the composite material.

To evaluate the influence of sisal fibres orientation on the mechanical properties of composites, two arrangements were used: woven and randomly arranged sisal fibres (Fig. 2).

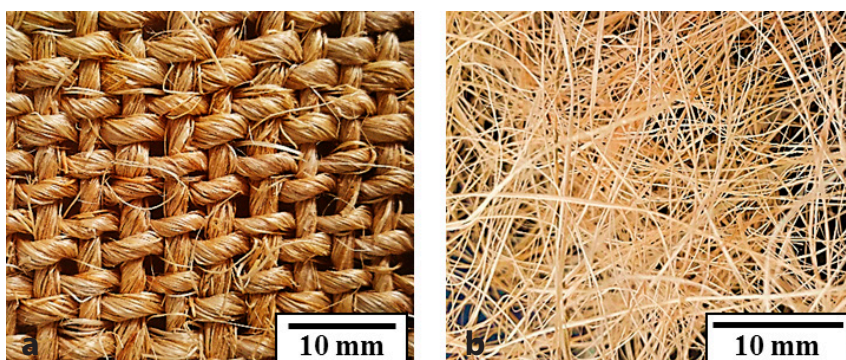


Fig. 2 (a) Woven sisal fibres at (0°/90°) and (b) randomly arranged sisal fibres

Woven sisal fibres were configured in plain weave, (0°/90°) configuration, type 530/1 yarns, with nearly 2 mm thickness and gaps between them of approx. 1 mm² weft yarns. In the random configuration, sisal fibres were arranged multi-directionally, assuring a better isotropic mechanical behaviour.

Composites were manufactured using the 70/30 mass ratio (matrix/fibre). The mass ratio was selected after preliminary experiments based on Ahmad and Luyt (2012). The boards produced using the 70/30 mass ratio proved to be more efficient in terms of the final thickness. Pure HDPE boards (without reinforcement) were also manufactured. In all experimental conditions, polymeric layers have been produced by stacking plastic films (from polyethylene bags), forming multi-layered plastics. For the standardisation of the same thickness of the boards, the value of the mass required for the pure HDPE board was determined using Eq. 1 as a function of the densities of the materials. An approximate density of 0.95 g·cm⁻³ was chosen for the HDPE (Guilhen et al., 2017).

$$m = \rho v, V_v = \frac{(\rho_{ct} + \rho_{ce})}{\rho_{ct}} \cdot 100 V_v = \frac{(\rho_{ct} + \rho_{ce})}{\rho_{ct}} \cdot 100 \quad (1)$$

where:

- m* – material mass (g)
- ρ – material density (g·cm⁻³)
- v* – material volume (cm³)

The composite board dimensions were 190 × 110 mm (length, width), and the total mass was nearly 105 g. Woven sisal fibre-reinforced HDPE composites were made of HDPE layers at the faces and fibres at the centre. In case of randomly arranged sisal reinforcement, fibres were interleaved into three major layers of plastic in order to allow the formation of intermolecular bonds between the reinforcement gaps and HDPE. Non-uniform regions of the bags were discarded to minimize variations in the properties of the produced composites.

Hot compression moulding

The composites were moulded into boards by hot compression moulding,

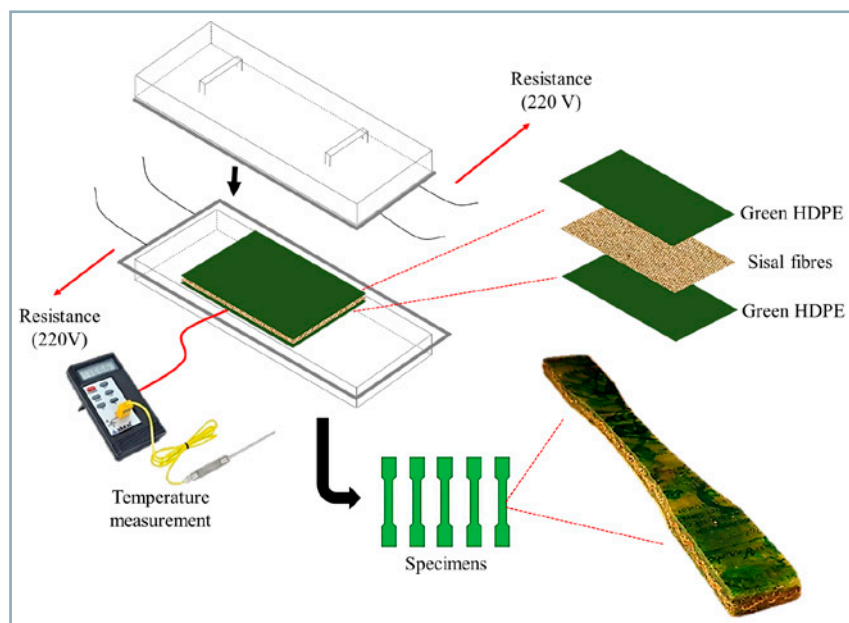


Fig. 3 Process of hot compression moulding to make sisal HDPE composites

as shown in Fig. 3; for these purposes, equipment specially developed for this study was utilized. It contained two electrical resistors (2,000 W of power), each attached within blocks of refractory material 50 mm thick and covered by metal sheets.

The composites were moulded between two aluminium boards with dimensions of 550 × 250 × 10 mm. In addition, an Armalon® (cover) protection was used to prevent chemical interactions between aluminium boards and composite materials. The pressure used to make the composites was approximately 5.46 kPa. It was calculated on the basis of the weight exerted by the upper block of the equipment and applied directly to the composite surface (board face). Preliminary experimental results indicated that lower working pressures were not effective for the purposes of the board moulding and compaction process.

The average temperature inside the mould was fixed at 185 °C. This temperature was selected on the basis of the exploratory testing and values provided in literature. Coutinho et al. (2003) stated that required temperature should exceed the HDPE melting point, which is approximately 135 °C. Composites heated to temperatures above 190 °C were polyethylene bags with visible degradation aspects. When temperatures reached the value above 200 °C, fibre degradation due

to material depolymerisation was verified. The total time necessary for manufacturing of one board was two hours.

Mechanical tests

Tensile tests were conducted utilizing a Shimadzu universal testing machine, model AG-X Plus. Specimens of pure HDPE, as well as reinforced composites, were tested in order to compare the influence of the reinforcement on the tensile properties of the new material.

According to the ASTM D638 (2014), the Type I specimen model for reinforced composites was used. Specimens with dimensions of 165 × 19 × 5 mm and narrow section width

of 13 mm were tested at 5 mm·min⁻¹ speed. The specimens were shaped using a jigsaw machine. Five specimens were obtained from each board and ten specimens were tested from each experimental condition. The edges of the board were not used for testing. The mean value of each property was calculated from the five central results.

Results and discussion

Composite manufacturing

The cooling process has direct influence on the homogeneity of composite faces. When the material is removed at high temperatures, there is a rapid cooling and consequent solidification, resulting in physical heterogeneities in the composite faces. Moreover, there can occur a deformation of the board due to stretching phenomenon, caused by the increased resistance of the material resultant from the alignment of the polymeric chains (Barros and Branciforti, 2018). Therefore, the composites remained inside the mould for one hour until a temperature of 100 °C was reached (below the average crystallisation temperature, estimated between 116 and 124 °C (Choudhury, 2008)). Once removed from the mould, the board was kept at room temperature (25 °C) until completely cooled. Fig. 4 shows that the manufacturing process used allows uniform flow between the gaps of the sisal fibres and enables a settled stiffness of the composite mechanical

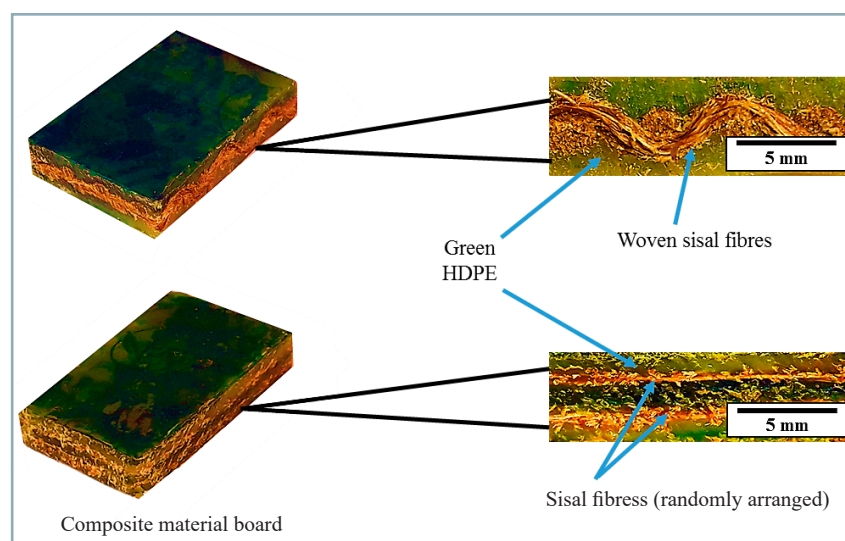


Fig. 4 Sisal fibre-reinforced green HDPE composite

structure. Lateral section of a tensile test specimen shows structure homogeneity and quality of the cuts (Fig. 4).

Mechanical tests

Table 2 shows the results of tensile tests for each experimental condition. Pure green HDPE showed higher tensile strength than pure traditional HDPE, indicating the possibility of replacing the fossil polymer with green polymer.

Fig. 5 shows the stress-strain curves of different types of materials tested. These curves show typical examples of each experimental condition, because they were very similar. Composites with woven sisal fibres achieved higher ultimate strain than composites with randomly arranged

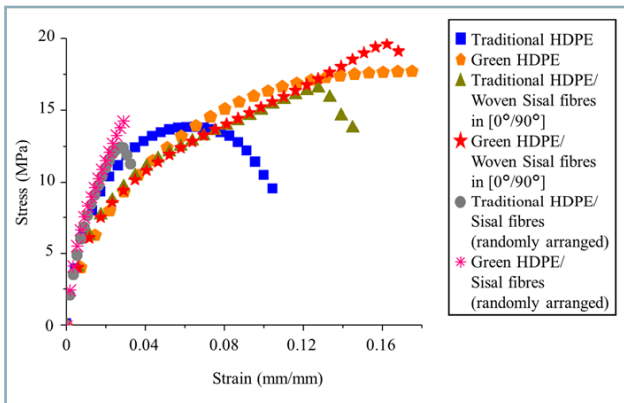


Fig. 5 Stress-strain curves for each condition

fibres, suggesting the influence of the reinforcement type on this mechanical property. Woven sisal fibre-reinforced HDPE composites demonstrated a quasi-linear behaviour in the plastic region, until reaching its ultimate strain.

The green HDPE composite reinforced with woven sisal fibres in (0°/90°) showed the highest tensile strength (Fig. 6) because of the influence of the relationship between fibre arrangement and direction of applied stress. Composites with randomly arranged sisal fibres showed lower tensile strength than other experimental arrangements, which can be explained by the load transfer mechanism.

Regarding the modulus of elasticity, composites with woven sisal fibres in (0°/90°) presented the lowest values from all experimental arrangements (Fig. 7), indicating a more ductile behaviour. Composites with randomly arranged sisal fibres had a larger contact surface with the matrix, improving the efficiency of interfacial adhesion, which ensures the transmission of mechanical loads (Jawaid et al., 2011).

Pure green HDPE specimens achieved higher ultimate strain than pure traditional HDPE (Fig. 8), indicating a more efficient process of alignment of the polymeric chains, which increased their resistance to mechanical stress applied in the direction of these chains (Barros and Branciforti, 2018). Composites with randomly arranged sisal fibres demonstrated high stiffness up to 2.5% in strain but ruptured after low plastic deformation.

The results show that although the woven sisal fibres in (0°/90°) had an increase in the composite tensile strength,

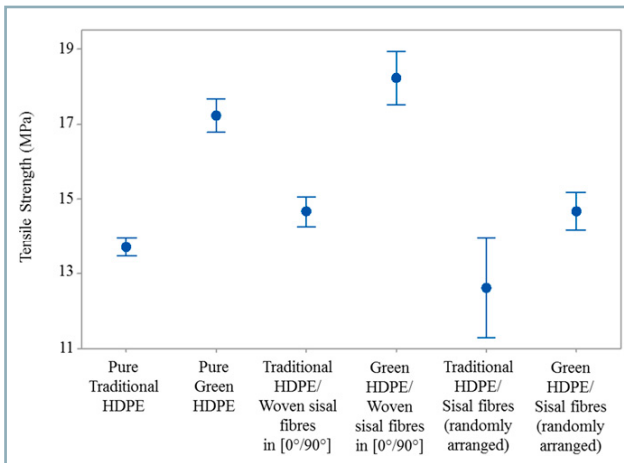


Fig. 6 Tensile strength of the specimens

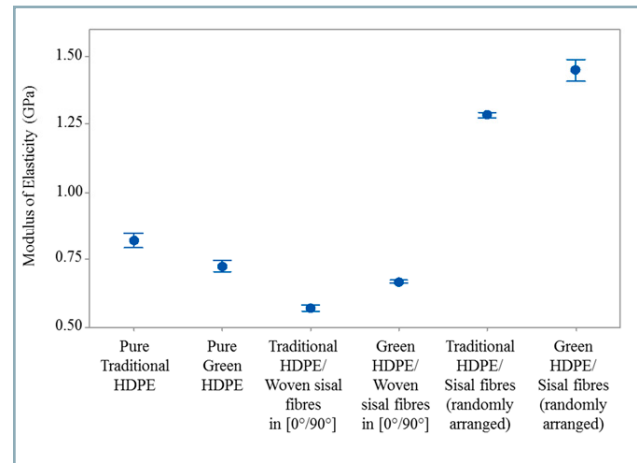


Fig. 7 Modulus of elasticity of the specimens

Table 2 Tensile tests results

| Experimental condition | Tensile strength (MPa) | Modulus of elasticity (GPa) | Ultimate strain (%) |
|---|------------------------|-----------------------------|---------------------|
| Pure Traditional HDPE | 13.72 ±0.56 | 0.82 ±0.06 | 6.12 ±0.66 |
| Pure Green HDPE | 17.22 ±1.13 | 0.73 ±0.05 | 18.10 ±1.93 |
| Traditional HDPE/Woven sisal fibres in (0°/90°) | 14.71 ±1.24 | 0.57 ±0.03 | 11.77 ±2.21 |
| Green HDPE/Woven sisal fibres in (0°/90°) | 18.29 ±1.84 | 0.67 ±0.01 | 15.65 ±0.57 |
| Traditional HDPE/Sisal fibres (randomly arranged) | 12.64 ±2.98 | 1.29 ±0.02 | 1.64 ±0.20 |
| Green HDPE/Sisal fibres (randomly arranged) | 14.70 ±1.13 | 1.45 ±0.09 | 2.84 ±0.35 |

*Five specimens were considered in the mean values

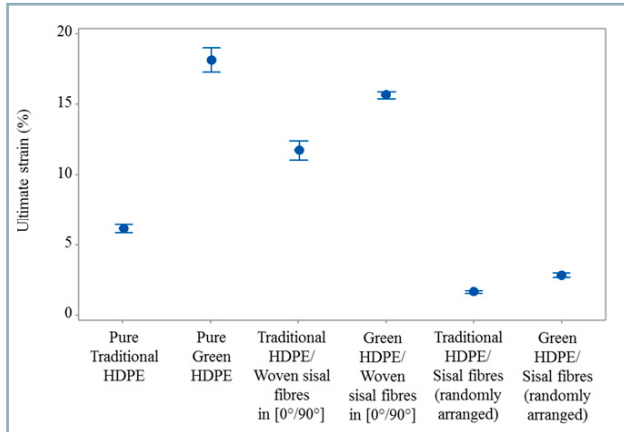


Fig. 8 Ultimate strain of the specimens

it caused the decrease in its stiffness. On the other hand, the randomly arranged sisal fibre-reinforced composites showed an opposite behaviour. The polyethylene was better included in the sisal fibre structure, resulting in a more compact and stiffer structure.

Figs. 9 and 10 show the main failure modes verified after tensile tests. A large plastic deformation in the matrix, as well as sisal fibres pull-out and delamination, were detected in woven sisal fibre-reinforced HDPE composites (Fig. 9). The results and the damage mechanisms signaled low adhesion in the interfacial zones of these composites. Plastic deformation was influenced by the alignment of the polymeric chains, which was caused by the material cooling during the manufacturing process (Mokhena and Luyt, 2014). In several cases, matrix breakage was also observed. Fibre pull-out and delamination was directly related to the interfacial adhesion failure (Jawaid et al., 2011).

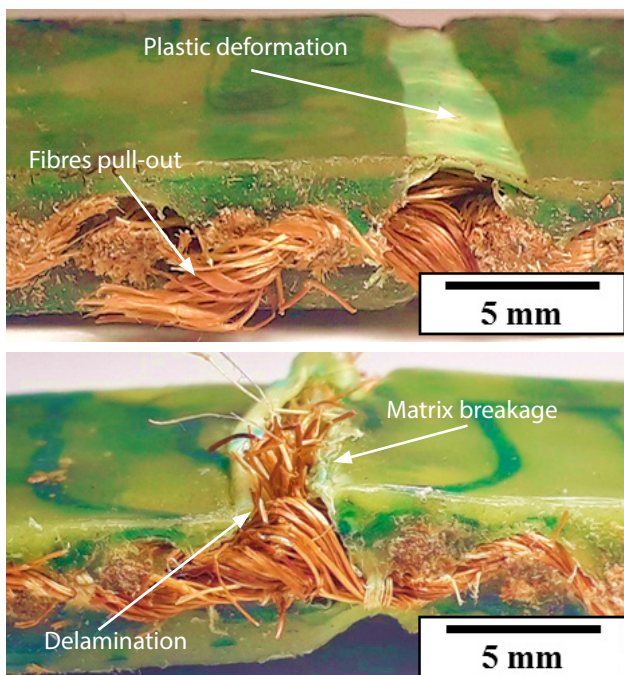


Fig. 9 Failure modes after tensile stress test of woven sisal fibre-reinforced green HDPE composites

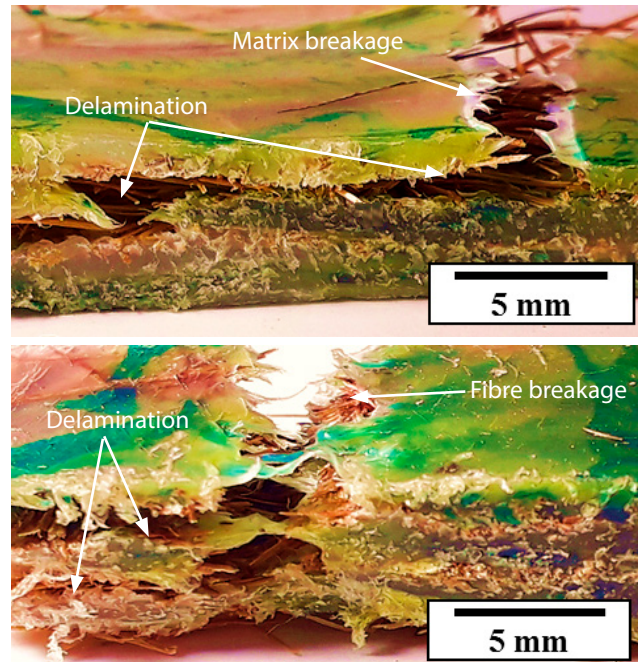


Fig. 10 Failure modes after tensile stress test of randomly arranged sisal fibre-reinforced green HDPE composites

In composites with randomly arranged sisal fibres, delamination was the predominant damage found (Fig. 10). Matrix and fibre breakage were also observed after tensile stress test. Sisal fibres have several hydroxyl groups in their chemical structure with a hydrophilic nature, and HDPE has also a hydrophobic nature, which negatively influences the load transfer between phases (Fig. 11), and neither fibres nor HDPE had been subjected to chemical treatment to improve the compatibilities and consequently the improvement of the mechanical properties, reaffirming the weak interfacial bond (Silva et al., 2013).

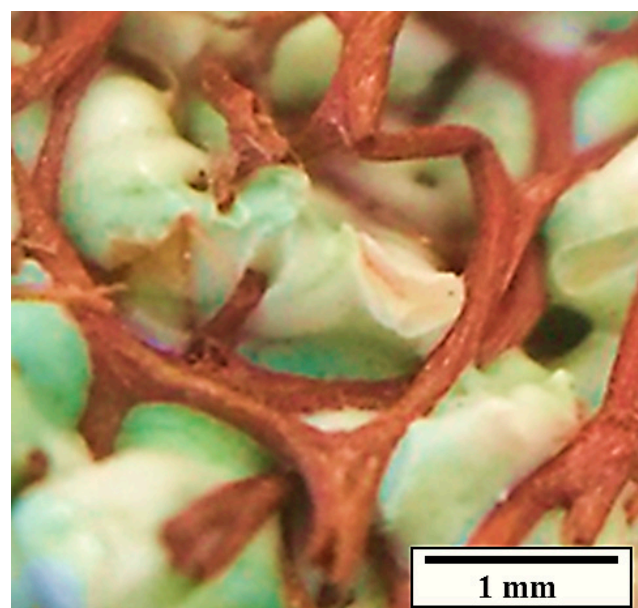


Fig. 11 Interfacial bonding of sisal HDPE composites

Conclusions

In this study, green composites were manufactured using an easier and low-cost hot compression moulding in contrast to traditional methods of composites moulding.

Woven sisal fibre-reinforced green HDPE composites achieved higher tensile strength and lower modulus of elasticity in comparison to pure HDPE specimens. On the other hand, randomly arranged sisal fibre-reinforced green HDPE composites had higher values for modulus of elasticity than pure HDPE, as well as composites with woven sisal fibres.

The results showed that the use of these materials in structural applications, such as drywall and insulated panels, is possible. In order to prevent any premature failure during use, the success of this application depends directly on the product requirements. However, the main reason to use recycled polymers and natural fibres (without chemical treatment) is due to the possibility to produce a sustainable material able to isolate thermal and acoustic variations.

Acknowledgments

This study was financed in part by the CNPq, FAPEMIG and Coordenação de Aperfeiçoamento de Pessoal de Nível Superior – Brazil (CAPES) – Finance Code 001. In addition, the authors thank the Center for Innovation and Technology in Composites (Citec) at the Federal University of São João del-Rei (UFSJ) and the Post-Graduate Programme in Mechanical Engineering and the Department of Production Engineering at the Federal University of Minas Gerais (UFMG), for the structure and the support provided.

References

- AHMAD, E. E. M. – LUYT, A. S. 2012. Effects of organic peroxide and polymer chain structure on mechanical and dynamic mechanical properties of sisal fiber reinforced polyethylene composites. In *Journal of Applied Polymer Science*, vol. 125, pp. 2216–2222.
- AKINYEMI, B. A. – OMONIYI, T. E. – ADEYEMO, M. O. 2016. Prospects of coir fibre as reinforcement in termite mound clay bricks. In *Acta Technologica Agriculturae*, vol. 19, no. 3, pp. 57–62.
- ASTM D638. 2014. Standard Test Method for Tensile Properties of Plastics. West Conshohocken, 13 pp.
- BARROS, R. M. – BRANCIFORTI, M. C. 2018. Correlation between molecular orientation, crystallinity and permeability of biaxially oriented linear low-density polyethylene films. In *Matéria (Rio de Janeiro)*, vol. 23, no. 1.
- CHATTOPADHYAY, S. K. – SINGH, S. – PRAMANIK, N. – NIYOGI, U. K. – KHANDAL, R. K. – UPPALURI, R. – GHOSHAL, A. K. 2011. Biodegradability studies on natural fibers reinforced polypropylene composites. In *Journal of Applied Polymer Science*, vol. 121, no. 4, pp. 2226–2232.
- CHOUDHURY, A. 2008. Isothermal crystallization and mechanical behavior of ionomer treated sisal/HDPE composites. In *Materials Science and Engineering A*, vol. 491, pp. 492–500.
- COUTINHO, F. M. – MELLO, I. L. – MARIA, L. C. S. 2003. Polyethylene: main types, properties and applications. In *Polímeros: Ciência e Tecnologia*, vol. 13, no. 1, pp. 1–13.
- FÁVARO, S. L. – GANZERLI, T. A. – DE CARVALHO NETO, A. G. V. – DA SILVA, O. R. R. F. – RADOVANOVIC, E. 2010. Chemical, morphological and mechanical analysis of sisal fiber-reinforced recycled high-density polyethylene composites. In *eXPRESS Polymer Letters*, vol. 4, no. 8, pp. 463–473.
- GUILHEN, A. – GADIOLI, R. – FERNANDES F. C. – WALDMAN, W. R. – PAOLI, M. A. D. 2017. High-density green polyethylene biocomposite reinforced with cellulose fibers and using lignin as antioxidant. In *Journal of Applied Polymer Science*, vol. 134, no. 35, pp. 45219–45228.
- IBRAHIM, I. D. – JAMIRU, T. – SADIKU, E. R. – KUPOLATI, W. K. – AGWUNCHA, S. C. – EKUNDAYO, G. 2016. Mechanical properties of sisal fibre-reinforced polymer composites: a review. In *Composite Interfaces*, vol. 23, no. 1, pp. 15–36.
- JAWAID, M. – ABDUL KHALIL, H. P. S. – ABU BAKAR, A. 2011. Woven hybrid composites: Tensile and flexural properties of oil palm-woven jute fibres based epoxy composites. In *Materials Science and Engineering A*, vol. 528, pp. 5190–5195.
- MOHD RAFEE, S. N. A. – LEE, Y. L. – JAMALLUDIN, M. R. – ABDUL RAZAK, N. – MAKHTAR, N. I. – ISMAIL, R. I. 2019. Effect of different ratios in biomaterials to banana peels on the weight loss of biodegradable pots. In *Acta Technologica Agriculturae*, vol. 22, no. 1, pp. 1–4.
- MOKHENA, T. C. – LUYT, A. S. 2014. Investigation of polyethylene/sisal whiskers nanocomposites prepared under different conditions. In *Polymer Composites*, vol. 35, no. 11, pp. 2221–2233.
- PLATI, C. 2019. Sustainability factors in pavements materials, design and preservation strategies: A literature review. In *Construction and Building Materials*, vol. 211, pp. 539–555.
- SANTOS, A. F. – MARTINS, C. Y. – SANTOS, P. O. – CORRÊA, E. B. – BARBOSA, H. R. – SANDOVAL, A. P. – OLIVEIRA, L. M. – SOUZA, J. T. – SOARES, A. C. 2014. Diazotrophic bacteria associated with sisal (*Agave sisalana* Perrine ex Engelm): potential for plant growth promotion. In *Plant and Soil*, vol. 385, pp. 37–48.
- SILVA, L. J. – CAMPOS RUBIO, J. C. – PANZERA, T. H. – BORGES, P. H. R. 2013. The effect of silica microparticles and maleic anhydride on the physic-mechanical properties of epoxy matrix phase. In *Science and Engineering of Composite Materials*, vol. 20, pp. 203–208.
- ZHAO, X. – LI, R. K. Y. – BAI, S.-L. 2014. Mechanical properties of sisal fiber reinforced high density polyethylene composites: Effect of fiber content, interfacial compatibilization, and manufacturing process. In *Composites: Part A*, vol. 65, pp. 169–174.



Acta Technologica Agriculturae 2
Nitra, Slovaca Universitas Agriculturae Nitriae, 2020, pp. 87–91

VERIFICATION OF THERMO-TECHNICAL CHARACTERISTICS OF SELECTED FLOOR CONSTRUCTIONS FOR DAIRY COWS (PILOT STUDY)

Michaela NÉMETHOVÁ*, Jana LENDELOVÁ, Veronika ŠRANKOVÁ, Miroslav ŽITŇÁK, Ľubomír BOTTO

Slovak University of Agriculture in Nitra, Slovakia

The purpose of this study was to theoretically and practically investigate the thermo-technical properties of two bedding surface materials under real farm conditions during the hot summer period. The study was focused on the research of cubicles with water mattresses and straw bedding for dairy cows. The results of thermal-technical calculations showed that straw belongs to the category of warm floors, the thermal effusivity value of cubicle with straw is $b = 173.55 \text{ W}\cdot\text{s}^{1/2}\cdot\text{m}^{-2}\cdot\text{K}^{-1}$; the heat transfer coefficient is $U = 0.36 \text{ W}\cdot\text{m}^{-2}\cdot\text{K}^{-1}$. Water mattress belongs to the category of cold floors with the thermal effusivity value $b = 572.46 \text{ W}\cdot\text{s}^{1/2}\cdot\text{m}^{-2}\cdot\text{K}^{-1}$ and the heat transfer coefficient $U = 4.504 \text{ W}\cdot\text{m}^{-2}\cdot\text{K}^{-1}$. On the basis of calculations, the results showed that U was 12.5 higher for water mattresses than for straw, and b was 3.3 times higher for water mattresses than for straw. Based on thermographic measurements under field conditions of dairy farm, it was observed that the surface temperature of the water mattresses after one hour of lying was lower by $4.95 \pm 1.88 \text{ }^\circ\text{C}$ in comparison to chopped straw. In practice, suitability of the material structure of water mattresses was verified on the basis of physical properties for summer period.

Keywords: water mattress; straw bedding; thermal conductivity; heat; dairy cows; summer period

Slovak climate conditions are intercontinental, however, the number of tropical days in summer gradually increases. The summer period is accompanied with multiple negative effects, which are associated with the risk of severe heat load. The term heat stress is used widely and rather loosely, and may refer to the climate, climatic effects on the cattle, or cattle productive or physiologic responses (West, 2003). Health problems arising from the heat stress have been described in numerous studies (Cook et al., 2007; West, 2003; Kadzere et al., 2002). It is necessary to be aware that a cow itself generates a large amount of metabolic heat and accumulates an additional amount of heat from radiant heat source. Heat production and accumulation coupled with cooling capacity due to environmental conditions causes a heat increase to a point, at which the body temperature of cow increases, food intake decreases, and production and reproduction parameters deteriorate (West, 2003). There are several solutions to this issue – cooling of air, body of dairy cows, and surrounding materials. The interaction between the environment and the dairy is critical for general welfare and production. There is a wide range of possibilities for dairy housing (Kull et al., 2017). The dairy cattle spend most of the time lying and the surface on which they lie has already been described by multiple researchers (Tucker et al., 2003; Lendelová et al., 2009; Kull et al., 2017) as affecting the dairy cows in several ways. Cattle at dairy usually lie on straw; sawdust; sand; mattresses filled with recycled material; mattresses filled with rubber; and water mattresses. Studies that led to the effectiveness determination of individual technical-material solutions have highlighted the different conclusions. Recent research has shown that

water mattresses are more preferred than mattresses filled with rubber (Wadsworth et al., 2015). The cattle with access to water filled mattresses spent a significantly lower amount of time lying and stood more in contrast to cows with access to sand beds and cattle kept at pasture (Margerison et al., 2014). The benefits of water mattresses lie in water incompressibility, which offers a nearly non-deformable bed and ability to co-ordinate the movement of mattress layers with the pressure of the joints during lying and reduce skin abrasions. The purpose of this study was to observe thermo-technical properties of two bedding materials during the hot summer period. The study was focused on the research of water mattresses and straw bedding.

Material and methods

This study was carried during the summer season in 2017. The dairy farm is located in a mild climate zone in Topoľčany region. The farm is located in a mild climate zone. One of the five naturally ventilated barns was selected for the purposes of the pilot study. The barn was an older reconstructed building designed for 176 Holstein dairy cows. Average milking yield per one dairy cow was 22.92 ± 2.85 litres per day. There were head to head cubicles with dimensions $4 \times 22 \text{ m}$ utilizing water mattresses on the left side and identical cubicles utilizing chopped straw on the right side. Water mattresses were cleaned once a day – in the morning during milking. Straw bedding was also changed once during milking. All alleys had grooved concrete surface.

Contact address: Michaela Némethová, Slovak University of Agriculture in Nitra, Faculty of Engineering, Slovakia, e-mail: xnemethova@is.uniag.sk

Thermal properties of straw were investigated in a previous research, in which the thermal properties of organic bedding were determined (Lendelová et al., 2016).

Theoretical calculation

The theoretical calculation was based on theoretical foundations of thermal conductivity in materials. Base information for calculations contains the STN 73 0540-2+Z1+Z2 (2019). Layers of stall base with materials were determined from the top to the bottom. Physical properties and formula for thermal effusivity calculation of all materials for every single layer were used from Chmúrny (2003).

General formula for floor thermal effusivity calculation is as follows:

$$b = \sqrt{c \cdot \lambda \cdot \rho}, \text{ W}\cdot\text{s}^{1/2}\cdot\text{m}^{-2}\cdot\text{K}^{-1} \quad (1)$$

where:

- c – specific heat capacity, $\text{J}\cdot\text{kg}^{-1}\cdot\text{K}^{-1}$
- ρ – bulk density, $\text{kg}\cdot\text{m}^{-3}$
- λ – coefficient of thermal conductivity, $\text{W}\cdot\text{m}^{-1}\cdot\text{K}^{-1}$

Two layer equivalent effusivity b^{**} ; three layer equivalent effusivity b^{***} , and multi-layer equivalent effusivity use non-dimensional coefficient $k_{x,y}$, where:

$$k_{x,y} = 2 \sum_{n=1}^{\infty} \left(\frac{x-1}{x+1} \right)^n \cdot e^{-(n^2 y)} \quad (2)$$

where:

- K – non-dimensional quantity characterizing the degree of influence of the floor layer competent on the heat exchange of the floor structure:

$$b^{**} = b_1(1 + K_{1,2}) \text{ and } b^{***} = b_1(1 + K_{1,2,3}) \quad (3)$$

where:

- b_1 – calculated on the basis of the top layer material properties

In addition, U – heat transfer coefficient – is calculated using formula by Chmúrny (2003).

$$U = \frac{1}{R}, \text{ W}\cdot\text{m}^{-2}\cdot\text{K}^{-1} \quad (4)$$

where:

$$R = \frac{d}{\lambda}, \text{ m}^2\cdot\text{K}\cdot\text{W}^{-1} \quad (5)$$

where:

- R – thermal resistance, $\text{m}^2\cdot\text{K}\cdot\text{W}^{-1}$
- d – thickness of layer, m
- λ – coefficient of thermal conductivity, $\text{W}\cdot\text{m}^{-1}\cdot\text{K}^{-1}$

Climate data

The climate data (air temperature and relative air humidity) were recorded by continuous measuring inside and outside of the barn using equipment COMET S-3121. For measurement of conditions during two hot summer months, 4 hours were selected (12:30–16:30) – the hottest hours of the day.

Thermographic measurements

The thermographic measurements were performed during two summer months. Measurements utilizing the thermocamera were always conducted when the outdoor temperature reached its peak – the period from 12:30 to 16:30. Thermograms of empty cubicles and cubicles after one hour of cow's lying (when the dynamics of temperature changes is already stabilized) were obtained using TP8S thermocamera with resolution 640×480 pixels.

Circular form was used for the same pixel area evaluation, recording thermocamera was placed at the top of the observed cubicle before each scanning. A new thermogram was scanned after the cow had lied down. To record the surface temperature, it was necessary that the cattle remained lying on the observed bedding types for a period of 60 to 70 minutes. The cow was disturbed from lying after this control time had passed, and the circle was immediately placed on the cubicle base where the animal has been lying (Figs. 1 and 2). Each thermogram was taken from the same height – lens of the thermocamera was always fixed at 1.80 m above the cubicle surface by a tripod. Tested cubicle surface could not be disturbed, either by thermocamera equipment or by human activity. Emissivity was set up for evaluated material. Selected samples did not include areas of straw and water mattresses fecated and/or urinated on, which would significantly change the physical properties of the observed surface. The program IS Guide IrAnalyser was used for thermogram scans evaluation.

Statistical analysis

Average surface temperature of empty cubicles and animal body prints was analysed utilizing ANOVA – one-way analysis

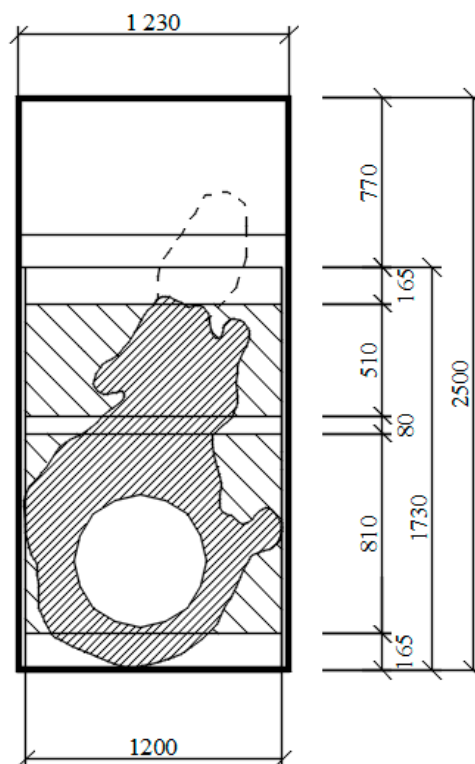


Fig. 1 Animal body print on the water mattress with auxiliary circle

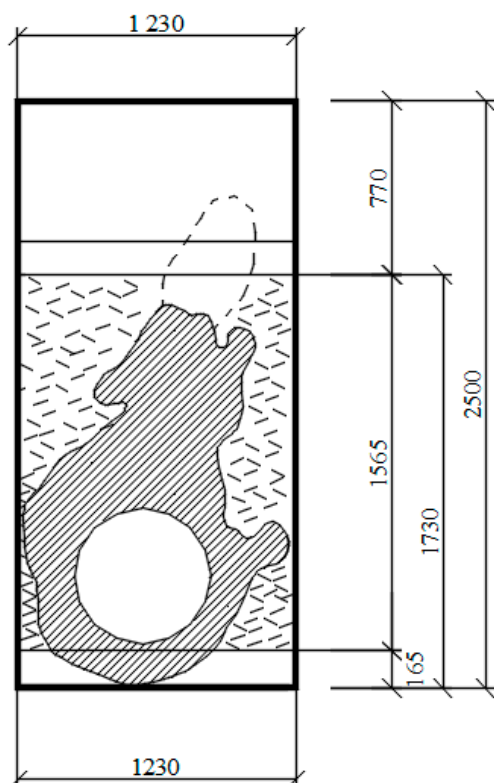


Fig. 2 Animal body print on the chopped straw with auxiliary circle

(STATISTICA 10, StatSoft CR s. r. o.). The factor was determined as a type of surface – water mattress and straw. There was also conducted a test of increasing the surface temperature before and after lying, in which the factor was temperature before and after lying. The significance of factors in ANOVA was performed by *T*-test. Differences between indoor and outdoor air temperature, as well as air relative humidity for summer months, were tested by means of independent samples *T*-test (STATISTICA 10, StatSoft CR s. r. o.).

Results and discussion

Thermo-technical calculations

Results of thermo-technical calculations are presented in Table 1.

Table 1 Results of thermo-technical stall base layer calculations

| Type of stall base | Number of layer | Material | <i>d</i> (m) | λ ($\text{W} \cdot \text{m}^{-2} \cdot \text{K}^{-1}$) | <i>b</i> ($\text{W} \cdot \text{s}^{1/2} \cdot \text{m}^{-2} \cdot \text{K}^{-1}$) | <i>U</i> ($\text{W} \cdot \text{m}^{-2} \cdot \text{K}^{-1}$) |
|----------------------------|-----------------|----------|--------------|--|--|---|
| Water mattress on concrete | 1 | rubber | 0.003 | 0.10 | 572.46 | 4.504 |
| | 2 | water | 0.035 | 0.60 | | |
| | 3 | rubber | 0.003 | 0.10 | | |
| | 4 | concrete | 0.150 | 1.43 | | |
| Straw on concrete | 1 | straw | 0.200 | 0.06 | 173.55 | 0.36 |
| | 2 | concrete | 0.150 | 1.22 | | |

$U_{wm, rwr} = 8.51 \text{ W} \cdot \text{m}^{-2} \cdot \text{K}^{-1}$ (rubber, water, rubber); $U_s = 0.34 \text{ W} \cdot \text{m}^{-2} \cdot \text{K}^{-1}$ (straw); $U_c = 9.53 \text{ W} \cdot \text{m}^{-2} \cdot \text{K}^{-1}$; $b_{(c)} = 1,882,02 \text{ W} \cdot \text{s}^{1/2} \cdot \text{m}^{-2} \cdot \text{K}^{-1}$ (concrete)

According to the calculations, straw showed more than 3 times lower thermal effusivity, indicating that it removes more than 3 times less heat from the cow's body in contrast to water mattress. Insulating properties of straw bedding with a thickness of 200 mm is better described by the heat transfer coefficient, which is approximately 12.5 times lower than for water mattress.

Climate data

Significant difference ($p < 0.05$) was observed between the outdoor and indoor air temperatures: it was lower in the stable. On the other hand, the relative air humidity in stable was significantly higher ($p < 0.05$) in comparison to the outdoor air humidity.

Table 2 Average outdoor and indoor data values during the monitoring period

| Climate parameters | |
|--|--------------------|
| Average air temperature ($^{\circ}\text{C}$) | |
| Outdoor | 35.41 ± 0.60 |
| Indoor | $32.55 \pm 0.53^*$ |
| Average relative air humidity (%) | |
| Outdoor | 27.37 ± 2.32 |
| Indoor | $34.43 \pm 3.50^*$ |

* $p < 0.05$

Thermographic measurements

Thermal calculations were tested by means of thermographic measurements under the farm conditions. These results are shown in Table 3.

Before the animal had lied down, water mattress surface temperature was found out lower than straw bedding surface temperature. After one hour of cow's lying, the difference in temperatures between materials was statistically significant ($p < 0.05$). The surface temperature of straw bedding was higher ($p < 0.05$) in contrast to water mattress temperature. The surface temperature of straw significantly increased ($p < 0.05$) after prolonged laying, whereas water mattress temperature did not show any significant increase.

Thermo-technical parameters necessary for calculation of the thermal effusivity *b*, and heat transfer coefficient *U*, coefficient of thermal conductivity λ , specific heat capacity *c*, bulk density ρ are different for bedded and no-bedded cubicles; this also affects their suitability and acceptability

Table 3 Average surface temperatures of the bedding types

| | Average surface temperature (°C) | | |
|-----------------------|----------------------------------|-------------|-------------|
| | before lying | after lying | difference |
| Straw | 32.77±1.76 | 35.88 ±0.38 | 3.11 ±1.94* |
| Water mattress | 29.67 ±1.13 | 30.93 ±0.82 | 1.26 ±1.42 |
| difference | 3.1 ±1.88* | 4.95 ±1.09* | |

* $p < 0.05$

for summer and winter. Considering the U (heat transfer coefficient), the smaller the value, the better the thermal insulation structure properties. It was observed that the most suitable material in terms of U was concrete ($U = 9.53 \text{ W}\cdot\text{m}^{-2}\cdot\text{K}^{-1}$), which allows the heat to dissipate from the animal body most efficiently in summer; however, it is disadvantageous in winter. All in all, it is a hard and formless material and thus unsuitable for the purposes of a surface for resting cows. Considering straw, U was 12.5 times lower than in water mattress, suggesting that chopped straw is more suitable bedding material for winter.

Similarly, in relation to evaluation of b – thermal effusivity – the higher the values, the faster the heat dissipation. Concrete is the most suitable material for lying in summer ($b = 1,882.02 \text{ W}\cdot\text{s}^{1/2}\cdot\text{m}^{-2}\cdot\text{K}^{-1}$) in this aspect. Water mattresses did not show high b when situated on the concrete stall base; however, this value was 3 times higher for water mattresses than for straw ($b = 173.55 \text{ W}\cdot\text{s}^{1/2}\cdot\text{m}^{-2}\cdot\text{K}^{-1}$). Straw provides the fastest adaptation of the cow contact body temperature in winter. The range between thermo-technical values was wide for steady state (U from 0.36 to $9.5 \text{ W}\cdot\text{m}^{-2}\cdot\text{K}^{-1}$; b from 173.55 to $1,882.02 \text{ W}\cdot\text{s}^{1/2}\cdot\text{m}^{-2}\cdot\text{K}^{-1}$), we evaluated the effect of the dynamics of changes in physical properties on the surface under field summer conditions. When the animals lie, there is a direct contact between the body and the stall base, which allows the heat exchange by the conductivity during each lying, which is 8–16 hours a day (Haley et al., 2000). Conductive cooling is one of the four ways of heat exchange available to cows to transfer the metabolic heat they produce to the environment. It involves the heat flow from the skin down a thermal gradient to a surface that has a lower temperature in summer (Ortiz et al., 2014). When a cow lies on water mattress, mattress surface temperature is cooler than the cow's skin, which allows transfer the heat from the body into the water inside the mattress (Lendelová et al., 2017). In practice, water mattress surface temperature provides a cooler lying surface before the cow lies on it. The initial straw surface temperature was higher than water mattress surface temperature and increased by $3.11 \pm 1.94 \text{ °C}$ after 1 hour of lying. The cow core body temperature is $38.59 \pm 0.48 \text{ °C}$ (Iwasaki et al., 2019); assuming the surface temperature of cows is approx. 35 °C , the temperature difference between the cow's body surface and water mattress surface is significantly higher after one hour of lying (4.1 °C) than in case of lying on the chopped straw (surface temperature of the straw is approx. 0.9 °C higher), the contact temperature area of which quickly adjusted. Water in mattresses has high thermal capacity and allows heat accumulation from air, ground and animals at slower rate than straw. Bastian et al. (2003) have proved that water temperature in mattresses can vary depending on time cows

spent lying on the mattress. During warm days, water-filled mattresses as a bedding surface can reduce the heat load with their local cooling when the cow rests on the mattress depending on the duration of its lying. Manninen et al. (2002) have found that straw cubicles were occupied significantly more frequently than sand cubicles during both winter and summer. Thanks to straw bedding, the time that cows spent lying increased, and cows preferred straw stalls to sand stalls (Norrington et al., 2008). There are only a few studies aimed at the conductive cooling efficiency evaluation during the summer period. Merely 20% of the cow's body surface is capable of heat exchange by conduction (Ortiz et al., 2014). Furthermore, Bastian et al. (2003) observed that only 19%. Measurements presented showed that, in some cases, the average body print surface temperature was slightly lower in contrast to the part unoccupied by the animal. It is possible that non-absorbent rubber surface creates a barrier for the emerging animal sweat, which can cause a print of micro-sweating. Its thermal respond can ultimately cause temperature drop accordingly to the wet surface, which is not perceptible by the human eye when working with a thermocamera. Sweating is a major, if not the most important, thermoregulatory mechanism used to dissipate excess body heat (Silanikove, 2000; Kadzere et al., 2002). There are two types of sweating that occur in dairy cows, both are appreciably involved in heat dissipation. The first type is insensible sweating – perspiration – that takes place constantly, unless the relative humidity is 100%. The other type – thermal sweating – occurs as a principle evaporative cooling mechanism of cow when ambient temperature rises. The heat required to convert water into vapour is referred to as the latent heat of vaporization. The proportion of metabolic heat that is dissipated from cow by evaporation increases with rising environmental temperature and a decreasing temperature gradient between the animal and air. Cattle showed appreciable increase in evaporative between 15 and 20 °C with rise in environmental temperature; the maximum rate of evaporative cooling was reached before 30 °C (Kadzere et al., 2002). Therefore, animal under heat stress are more sweating, what results in increased body fluid loss (Das et al., 2016). Heat loss by conductivity leads to increased water temperature in mattresses (Wadsworth et al., 2015; Bastian et al., 2003). Perano et al. (2015) investigated lowering of cow body temperature by means of cooling with circulating water in water mattress at 10 °C and 4.5 °C and found that rectal temperature of cows was lower by 0.3 °C when they were cooled with 4.5 °C circulating water in contrast to 10 °C circulating water; other variables taken into account did not show any significant difference between these two cooling temperatures. When cows were conductively cooled using 4.5 °C circulating water, rectal temperature decreased by 1.0 °C ; respiration rate decreased by 18 bpm; milk yield

increased by 5%; and DMI increased by 14% in comparison to the control herd. However, utilization of conductively cooled water mattresses is economically questionable in mild climate zone.

Conclusions

The purpose of this study was to theoretically and practically observe thermo-technical properties of two bedding materials during the hot summer period in mild climate of Slovakia under the field conditions. On the basis of theoretical evaluation of the thermo-technical properties of the design of cow cubicles, it was observed that elevated concrete stall base cubicles covered with water mattresses belong to the group of inadequately warm floors, while deepened concrete stall base cubicles filled with straw belong to the group of very warm floors with thermal effusivity lower than $b = 350 \text{ W}\cdot\text{s}^{1/2}\cdot\text{m}^{-2}\cdot\text{K}^{-1}$. Since this theoretical assessment in accordance with the standard calculations considers a constant state and takes into account neither climatic conditions nor dynamic changes in the cubicle surface, both types of cubicle surfaces have been investigated under field conditions.

Based on thermographic measurements under field conditions of dairy farm, the surface temperature of water mattresses was lower by $3.1 \pm 1.88 \text{ }^\circ\text{C}$ in comparison to the straw bedding before the cattle lied on these surfaces. The temperature difference measured after an hour of lying on water mattress was lower by $4.95 \pm 1.09 \text{ }^\circ\text{C}$ than on chopped straw. The straw surface temperature after an hour of lying is very close to the animal core temperature (average straw surface temperature was $35.88 \pm 0.38 \text{ }^\circ\text{C}$), which almost prevents the heat transfer from the cow body while lying during hot days. Higher temperature difference between animal body and water mattress surface creates a better environment for heat dissipation during hot summer days in Slovakia.

All in all, practical measurements should be emphasized, because it is better to take into account the values of thermal effusivity b from the point of view of physical calculations, since these values provide better description of the temporal development of surface temperatures during their occupation by cattle.

On the basis of aforementioned, emphasis is placed on other knowledge for verifying the water mattresses and chopped straw in practice according to the quality and state of cubicle, and different thermal-humidity conditions.

References

- BASTIAN, K. R. – GEBREMEDHIN, K. G. – SCOTT, N. R. 2003. A finite difference model to determine conduction heat loss to a water-filled mattress for dairy cows. In Transactions of the ASAE, vol. 46, no. 3, pp. 773–780.
- COOK, N. B. – MENTINK, R. L. – BENNETT, T. B. – BURG, K. 2007. The effect of heat stress and lameness on time budgets of lactating dairy cows. In Journal of Dairy Science, vol. 90, no. 4, pp. 1674–1682.
- DAS, R. – SAILO, L. – VERMA, N. – BHARTI, R. – SAIKIA, J. – IMTIWATI – KUMA, R. 2016. Impact of heat stress on health and performance of dairy animals. In A review. Veterinary World, vol. 9, no. 3, pp. 2.
- HALEY, D. B. – RUSHEN, J. – PASSILLÉ, de. M. A. 2000. Behavioural indicators of cow comfort: Activity and resting behaviour of dairy cows in two types of housing. In Canadian Journal of Animal Science, vol. 80, pp. 257–263.
- CHMÚRNÝ, I. 2003. Heat Protection of Buildings. Bratislava : Jaga Group, 2003. 214 pp. ISBN 80-88905-27-3 (In Slovak: Tepelná ochrana budov).
- IWASAKI, W. – ISHIDA, S. – KONDO, D. – ITO, Y. – TATENO, J. – TOMIOKA, M. 2019. Monitoring of the core body temperature of cows using implantable wireless thermometers. In Computers and Electronics in Agriculture, vol. 163, pp. 104849.
- KADZERE, C. T. – MURPHY, M. R. – SILANIKOVE, N. – MALTZ, E. 2002. Heat stress in lactating dairy cows: A review. In Livestock Production Science, vol. 77, no. 1, pp. 59–91.
- KULL, J. A. – INGLE, H. D. – BLACK, R. A. – EBERHART, N. L. – KRAWCZEL, P. D. 2017. Effects of bedding with recycled sand on lying behaviors, udder hygiene, and preference of lactating Holstein dairy cows. In Journal of Dairy Science, vol. 100, no. 9, pp. 7379–7389.
- LENDELOVÁ, J. 2004. Floor Constructions as an Important Phenomenon in Stables for Cattle and Pigs. Nitra : SUA. 184 pp. (dissertation thesis).
- LENDELOVÁ, J. – KARANDUŠOVSKÁ, I. – ŽITŇÁK, M. – BOĎO, Š. – MIHINA, Š. 2017. Effect of climatic conditions on differences in thermo-technical properties of organic bedding in laboratory testing. In Acta Technologica Agriculturae, vol. 20, no. 1, pp. 1–6.
- LENDELOVÁ, J. – POGAN, Š. – BOŽIKOVÁ, M. – PÁLEŠ, D. 2009. Simulation of heat conduction in natural and synthetic cow lying floors during wintertime. In Acta Technologica Agriculturae, vol. 12, no. 1, pp. 13–14.
- LENDELOVÁ, J. – ŽITŇÁK, M. – BOŠANSKÝ, M. – ŠIMKO, M. – PITERKA, P. 2016. Testing of property changes in recycled bedding for dairy cows. In Research of Agricultural Engineering, vol. 62, pp. 44–52.
- MANNINEN, E. – PASSILLÉ, de. A. M. – RUSHEN, J. – NORRING, M. – SALONIEMI, H. 2002. Preference of dairy cows kept in unheated buildings for different kind of cubicle flooring. In Applied Animal Behaviour Science, vol. 75, no. 4, pp. 281–292.
- MARGERISON, J. K. – LAU, J. – HEDLEY, M. J. – HORNE, D. J. – HANLY, J. A. – POWELL, N. – SHILTON, A. 2014. Lying and feeding behavior of dairy cows at pasture and housed in free stalls fitted with sand and water filled mats. In Occasional Report no. 27.
- NORRING, M. – MANNINEN, A. – PASSILLÉ, de. M. – RUSHEN, J. – MUNKSGAARD, L. – SALONIEMI, H. 2008. Effects of sand and straw bedding on the lying behavior, cleanliness, and hoof and hock injuries of dairy cows. In Journal of Dairy Science, vol. 91, no. 2, pp. 570–576.
- PERANO, M. K. – USACK, G. J. – ANGENENT, L. T. – GEBREMEDHIN, K. G. 2015. Production and physiological responses of heat-stressed lactating dairy cattle to conductive cooling. In Journal of Dairy Science, vol. 98, no. 8, pp. 5252–5261.
- ORTIZ, X. A. – SMITH, J. F. – ROJANO, F. – CHOI, C. Y. – BRUER, J. – STEELE, T. – SCHURING, N. – ALLEN, J. – COLLIER, R. J. 2014. Evaluation of conductive cooling of lactating dairy cows under controlled environmental conditions. In Journal of Dairy Science, vol. 98, no. 3, pp. 1759–1771.
- SILANIKOVE, N. 2000. Effects of heat stress on the welfare of extensively managed domestic animals. In Livestock Production Science, vol. 67, no. 1–2, pp. 1–18.
- STN 73 0540-2+Z1+Z2. 2019. Thermal protection of buildings. Thermal performance of buildings and components. Part 2: Functional requirements. (Slovak technical standard)
- TUCKER, C. B. – WEARY, D. M. – FRASER, D. 2003. Effects of three types of free-stall surfaces on preferences and stall usage by dairy cows. In Journal of Dairy Science, vol. 86, no. 2, pp. 521–529.
- WADSWORTH, B. A. – STONE, A. E. – CLARK, J. D. – RAY, D. L. – BEWLEY, J. M. 2015. Stall cleanliness and stall temperature of two different freestall bases. In Journal of Dairy Science, vol. 98, no. 6, pp. 4206–4210.
- WEST, J. W. 2003. Effects of heat-stress on production in dairy cattle. In Journal of Dairy Science, vol. 86, no. 6, pp. 2131–2144.



Acta Technologica Agriculturae 2
Nitra, Slovaca Universitas Agriculturae Nitriae, 2020, pp. 92–98

IMPROVED PROCEDURE FOR NATURAL CONVECTION GARLIC DRYING

Amor BOUHDJAR^{1*}, Hakim SEMAI¹, Amal BOUKADOUM¹, Sofiane ELMOKRETAR¹,
Azzedine MAZARI², Mohamed SEMIANI², Aissa AMARI¹

¹Renewable Energy Development Centre (CDER) Route de l'Observatoire Bouzaréah Algiers, Algeria

²Institut National de la Recherche Agronomique d'Alger (INRAA) Hassen Badi El Harrach Algiers, Algeria

Vegetable drying is an energy consuming procedure despite the fact that it is the most efficient way to preserve agricultural products. This study investigates a new way to dry good quality garlic at lower cost. Thin garlic layer was submitted to free convection airflow at air drying temperature of 40 °C, 50 °C, and 60 °C. Using the slope method, effective diffusivity coefficient was determined at each drying temperature during the first and second falling drying rate periods. Considering the former, it increased with increasing temperature. In relation to latter, it decreased with the temperature increase. However, at low drying temperatures, process keeps on going to very low moisture content; and it develops to an asymptotic value at high temperatures, indicating that shrinking at high temperature prevents evaporation of some residual moisture. Considered separately, these temperatures do not reflect the conditions met in solar drying, since in solar systems, air temperature increases during the day with increasing solar radiation. Therefore, characterization of garlic drying by means of step temperature varying – the first hour of drying at 40 °C; the second hour of drying at 50 °C, and the remaining time of drying at 60 °C – might better correspond with conditions under solar drying and result in better understanding of the process.

Keywords: free convection airflow; stepwise increasing temperature; solar drying; effective diffusivity

Throughout the world, garlic is widely used in cuisine. It is believed that it can also be used as an effective form of plant-based medicine in many ways and thanks to these properties, it is a very important commercial product.

The annual world production is approx. 27 million tons and this makes it the tenth most harvested vegetable in the world. It is predominantly produced in few places, yet it is transported all over the world. Considered under harvest form, the vegetable mass consists of more than two third of water. This would induce higher costs in transportation, storage and other handlings. Moreover, when the rest period (60–80 days) expires, the garlic sprouts rapidly emerge after dormancy. Consequently, nutritional value in the garlic is diminished, and due to withering of the stem and trunk, garlic quality is lowered (Amiri Chayjan et al., 2012).

Drying might be the best way to lower the additional costs by reducing the weight to less than one third of the initial weight. In addition, low moisture content reduces microbial and enzymatic changes throughout the storage period, hence, extending the shelf life of the product (Sacilik and Unal, 2005; Barrozo et al., 2001).

However, drying is a process involving phase change, therefore, it is a process that consumes much more energy. It is a complicated process including transient transfer of mass and heat with certain rate processes, which may result in modifications in product quality (Al-Neama and Farkas, 2016). In order to optimize the process, knowledge on the drying mechanisms is essential. Vegetable drying

is a complex phenomenon, which involves simultaneous actions of heat and mass transfer in the product. Understanding of such a phenomenon is based on a good knowledge of the balances between air and product, and control of the kinetics of the product drying and processing.

Multiple studies (Bozkir et al., 2019; Figiel, 2009; İlter et al., 2018; Younis et al., 2018; Thuwapanichayanan et al., 2014; Ruhanian and Movagharnejad, 2016; Ondro et al. 2017) considered different drying techniques, such as convective hot air, microwave drying, combined microwave convective drying, vacuum microwave drying, far infrared radiation drying assisted heat pump, combined drying. Amiri Chayjan et al. (2012) studied thin layer drying properties of garlic sheets under semi fluidized and fluidized bed conditions. The bed was submitted to convective air at different temperatures and velocities. They tested different empirical correlations in order to determine the diffusivity coefficient in the product. Sharma and Prasad (2004) undertook combined drying of garlic cloves, which consisted of continuous applying microwave of 10–40 W together with hot air at temperature of 40–70 °C and velocities of 1.0 and 2.0 m·s⁻¹. They observed diffusivity dependences on initial moisture content, air temperature and microwave power at given velocities. Pezzutti and Crapiste (1997) studied changes in garlic flavour during dehydration as a function of temperature. They noticed that, at high temperatures, there is a loss of flavour strength. Afriyie et al. (2009)

Contact address: Amor Bouhdjar, Renewable Energy Development Centre (CDER) Route de l'Observatoire Bouzaréah Algiers, Algeria, e-mail: a.bouhdjar@cder.dz; bouhdjar.amor@gmail.com

studied solar process drying in solar dryer. The efficiency of the proposed system is dependent on the local relative humidity. Furthermore, Afriyie et al. (2011) considered an improved configuration of a solar dryer and proposed several suggestions with respect to geographical regions. However, they did not investigate the characterization of the crop under evolving drying conditions. Certain properties of food, such as colour, structure, aroma compounds, and nutritional substances, are significantly influenced by high temperatures. Changes in these properties may negatively affect the product quality (Pezzutti and Crapiste, 1997).

Following an adequate drying procedure is a way to generate high quality dried garlic, in shorter drying time, with low energy consumption and better appearance. Drying kinetics are the most important information needed for dryer simulation and design.

Previous studies on drying kinetics of garlic have considered neither natural convective drying nor the effect of temperature variation during the drying process. These phenomena are often met in solar drying. This study intends to simulate drying under solar thermal drying process, which means varying temperature during the drying period and its consequences on the whole process.

Material and methods

Experimental setup

Experiments were conducted using a laboratory scale system. As shown in Fig. 1, the system consists primarily of a heat source, chimney, and perforated tray, on which the garlic slices with approx. 4.5 mm thickness are placed. Airflow is generated by buoyancy forces. Heat source is adjusted to the desired temperature. The air velocity is dependent on airflow temperature, chimney height and friction forces. Due to the decrease in friction forces caused by the slices during drying, the velocity tends to increase and the temperature diminishes. Subsequently, the heat source must be adjusted in order to maintain the desired temperature. Throughout the process, the velocity is increased since friction forces are diminished (they represent the only parameter that changes throughout the process). The air is heated while flowing through an electrical heater. The flowing air temperature is measured and controlled ahead of the garlic tray. The relative humidity is measured upstream of the sample tray. The air velocity is measured downstream. A digital anemometer – Prova AVM 3 – is used for these purposes; it has a resolution of 0.1 m·s⁻¹ and an accuracy of 3%. The temperature and relative humidity are measured using a digital combined probe CHY722 with an accuracy of 0.5 °C for the temperature, and 2.5% for the relative humidity. Denver instrument balance with accuracy of 0.01 g was used to measure the weight of samples.

The crosswise cut, i.e. slice cut normal to the main axis, was adopted. This configuration seems to give the highest drying rate according to Babetto et al. (2011). The same initial garlic mass was used in all runs. At least three runs were performed for every case to ensure identical conditions.

During drying, garlic samples were weighed every ten minutes. Although one might consider drying state is reached when three consecutive weighing measurements

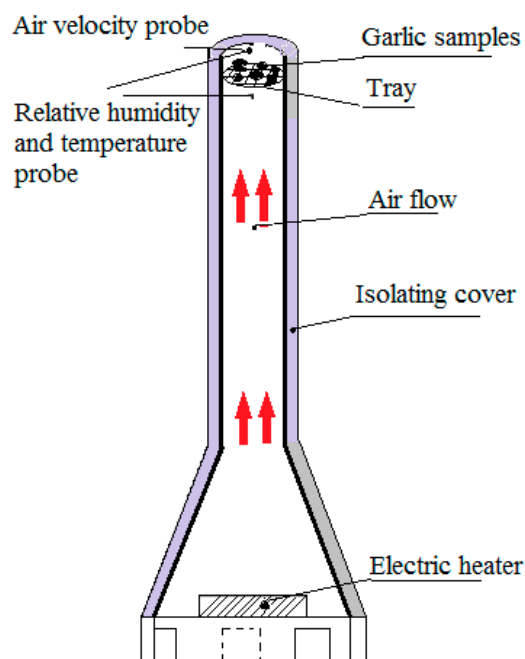


Fig. 1 Experimental setup for garlic drying

showed unchanged values, the process continued for a longer time for the purposes of analysis.

Since the paper considers the natural convection, only the temperature is adjusted. Three temperatures – 40 °C; 50 °C; 60 °C – are investigated in the individual experiments. Garlic samples were placed as one layer on 110 mm diameter circular tray located in the chimney (Fig. 1). The tray is 170 cm away from the heat source in order to avoid any IR rays influence.

Mathematical model and analytical solution

Moisture movement in food material during drying is due to a combination of different mechanisms, mainly liquid diffusion, capillary flow and vapour diffusion. These mechanisms can be lumped together into a diffusion-like equation (Crapiste et al., 1988). Considering a slab of the material of thickness 2l, through which water diffusion is predominantly taking place, and assuming that physical properties are uniform and constant over the product during the mass transfer phenomena, and assuming that the temperature is constant and uniform during phase change, a mass balance over a volume element yields the following equation:

$$\frac{\partial M}{\partial t} = \left[\frac{\partial}{\partial x} \left(D_{eff} \frac{\partial M}{\partial x} \right) \right] \quad (1)$$

where:

M – moisture content, kg water·kg dry matter⁻¹

x – mass transfer path, m

t – time, s

D_{eff} – effective moisture diffusivity coefficient, m²·s⁻¹

It should be noted that, although we assumed constant properties, the effective diffusivity coefficient (D_{eff}) varies

considerably with product structure, moisture content and temperature. Nevertheless, it can be estimated by an analysis of the drying data (moisture M vs. time t).

The appropriate initial and boundary conditions for one-dimensional transport are:

$$\begin{aligned} \frac{\partial M}{\partial x} &= 0 \quad t > 0 \quad x = 0 \\ M &= M_e \quad t > 0 \quad x = l \\ M &= M_i \quad t = 0 \quad 0 < x < l \end{aligned} \quad (2)$$

where:

l – half the sample thickness

M_i – initial moisture content

M_e – moisture content at equilibrium, which might be assimilated to the moisture content when the humidity ratio is at the limit of the material and the moisture of the air flowing over the material are equivalent

When internal mass transfer is the controlling mechanism, and one-dimensional transport with constant effective diffusivity is assumed, the solution of Eq. 1 for the total moisture content in a slab might be obtained.

Using the method of separation of variables and applying the initial and boundary conditions, the solution is given by:

$$MR = \frac{M - M_e}{M_i - M_e} = \frac{8}{\pi^2} \sum_{n=0}^{\infty} \frac{1}{(2n+1)^2} \exp\left[-D_{eff} \frac{(2n+1)^2 \pi^2 t}{4l^2}\right] \quad (3)$$

where:

MR – moisture content ratio

Dimensional analysis shows that only the first term is valuable and the others might be disregarded. This leads to:

$$MR = \frac{M - M_e}{M_i - M_e} = \frac{8}{\pi^2} \exp\left[-D_{eff} \frac{\pi^2 t}{4l^2}\right] \quad (4)$$

By inserting $K = \frac{\pi^2 D_{eff}}{4l^2}$ to Eq. 4, we get:

$$MR = \frac{8}{\pi^2} \exp(-Kt) \quad (5)$$

After taking the natural logarithm and rewriting, we get the following expression:

$$\ln(MR) = \ln\left(\frac{8}{\pi^2}\right) - Kt \quad (6)$$

where:

K – slope of the curve obtained from $\ln(MR)_{exp}$ versus t

The effective diffusivity coefficient – D_{eff} – can be determined as follows:

$$D_{eff} = \frac{K}{\pi^2} 4l^2 \quad (7)$$

Results and discussion

Experimental results

As it was mentioned, three temperatures were considered in this study i.e. 40 °C, 50 °C, and 60 °C. Fig. 2 shows the temperatures recorded during each experiment run. For varying temperature, three steps were considered corresponding to 40 °C during the first hour, 50 °C during the second hour and 60 °C for the remaining time. The motivation will be explained later. On the other hand, for each temperature, air velocity increases continuously because of the increase in the flow passage section. Fig. 3 shows the velocities recorded during the experiment. The velocity corresponding to the increments in varying temperature increases more steeply due to the change in temperature.

This is because the whole system is a chimney of different sectional areas at different heights, with some bends, expansions and contractions. With smooth wall

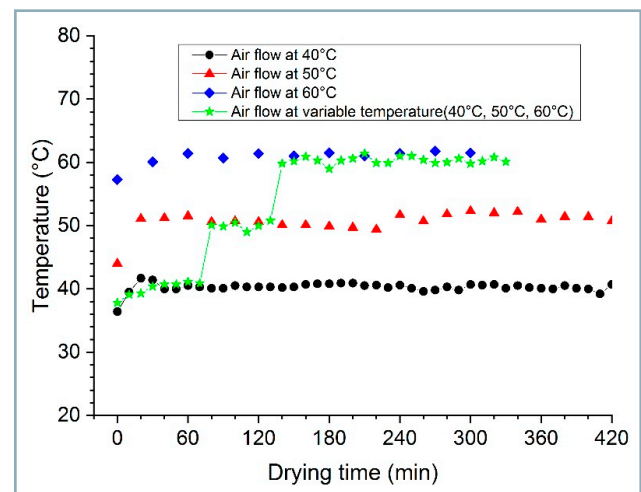


Fig. 2 Temperatures for the four tests undertaken during garlic drying

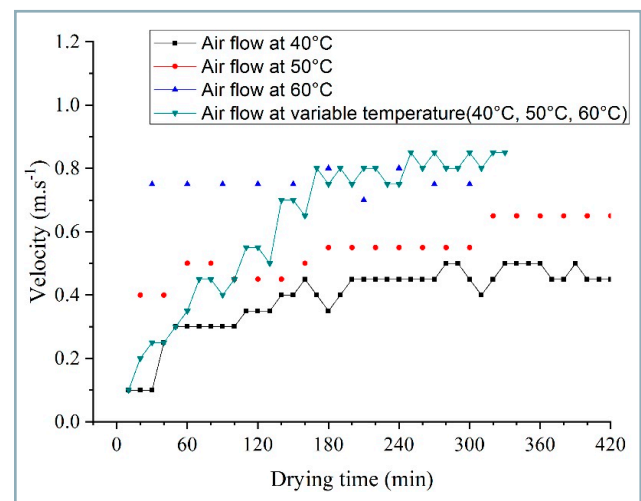


Fig. 3 Airflow velocities for different temperatures measured during the four garlic drying tests

surfaces, friction losses between the fluid and wall surfaces are negligible in contrast to the local losses from expansion, contraction and bending (Afonso and Oliveira, 2000).

On the basis of the relation between air density and temperature (Incropera and De Witt, 1996) and fundamental principle that buoyancy pressure head must be equal to the sum of all flow pressure losses between inlet and outlet, the underlying airflow equation is given by:

$$g\rho\beta(T_H - T_a)\Delta H = \sum K_i\rho\frac{v_i^2}{2} \quad (8)$$

where:

- T_H – airflow temperature, °C
- T_a – ambient temperature, °C
- v – airflow velocity, $\text{m}\cdot\text{s}^{-1}$
- g – acceleration due to gravity, $\text{m}\cdot\text{s}^{-2}$
- ρ – air density, $\text{kg}\cdot\text{m}^{-3}$
- β – expansion coefficient, $1/\text{T}$
- H – chimney height, m
- K – friction coefficient. The right side expresses all local losses

Considering only the passage area through the samples, tube section beyond the tray and continuity equation, Eq. 8 can be rewritten with respect to the outlet velocity as:

$$v_o = \frac{\sqrt{2g\beta(T_H - T_a)\Delta H}}{\sqrt{K_t + K_p\left(\frac{A_t}{A_p}\right)^2}} \quad (9)$$

where:

- A – passage area, m^2
- v_o – outlet airflow velocity, $\text{m}\cdot\text{s}^{-1}$

In this expression, the numerator expresses the driving force achieved by the chimney height and the temperature difference between the high temperature and ambient temperature enhancing the airflow. The denominator expresses the overall resistance due to friction through the passage area and the expansion beyond the tray. As the drying goes on, samples begin to shrink, increasing space between them, so the velocity gradually augments for further runs (Fig. 3). This is more evident in experiment run at varying temperature. For airflow at 40 °C, the velocity started at 0.1 $\text{m}\cdot\text{s}^{-1}$ and finished at approx. 0.4 $\text{m}\cdot\text{s}^{-1}$. For airflow at 50 °C, the velocity started at 0.4 $\text{m}\cdot\text{s}^{-1}$ and reached an average value of 0.6 $\text{m}\cdot\text{s}^{-1}$. Considering the airflow at 60 °C, the average velocity was approx. 0.8 $\text{m}\cdot\text{s}^{-1}$. For the airflow at varying temperature, the velocity followed the development of the driving force, i.e. mostly the temperature difference. Product moisture decreased with increasing air temperature. With increasing temperature, the drying time was reduced due to increased thermal gradients inside the material, and as a result, drying rate increased. It should be emphasized that the entire drying process takes place during the falling drying rate period.

Measurements showed that an increase in airflow temperature from 40 °C to 60 °C induced a decrease of the drying time of garlic slices. Consequently, the drying rate

increased with an increase in the drying air temperature (Fig. 6). However, Fig. 4 shows that, after certain drying time, samples exposed to the 40 °C airflow continue to yield some moisture, while drying rate is near zero for samples exposed to 60 °C airflow. According to several authors (Madamb et al., 1994; Ortiz-García-Carrasco et al., 2015), products exposed to high temperatures seem to shrink more and this phenomenon impacts mostly the product periphery. Consequently, the pores tend to close and decelerate water mobility and withhold some moisture as residual moisture although the airflow velocity is higher. On the other hand, with low temperature, drying process continues.

Therefore, when the samples were submitted to airflow at an increasing temperature – at 40 °C for the first hour, 50 °C at the second hour, and 60 °C for the remaining time – it was observed that the drying time is shorter compared to the previous cases when the temperature was constant during the whole run (Fig. 5). Moreover, the drying rate decreased steadily throughout the whole process for the constant temperatures.

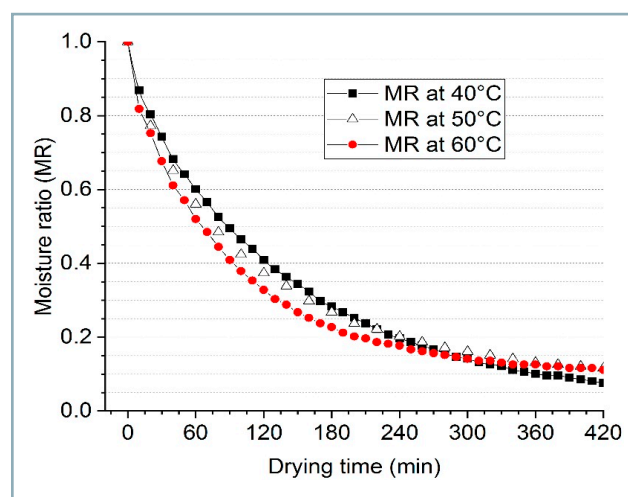


Fig. 4 Moisture content during drying at uniform temperatures

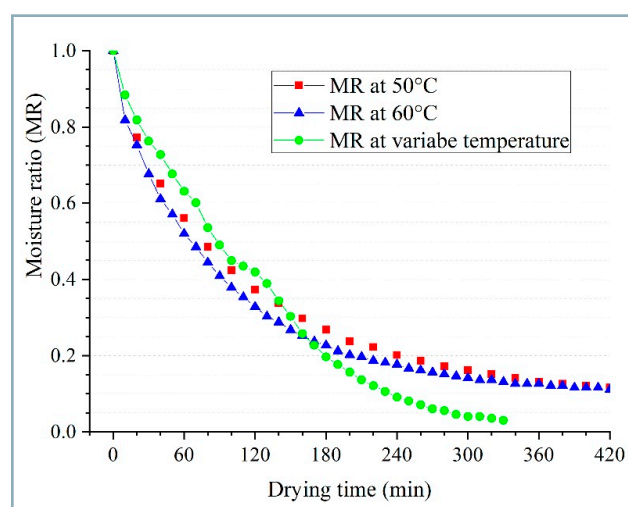


Fig. 5 Moisture content ratio during drying at varying temperature

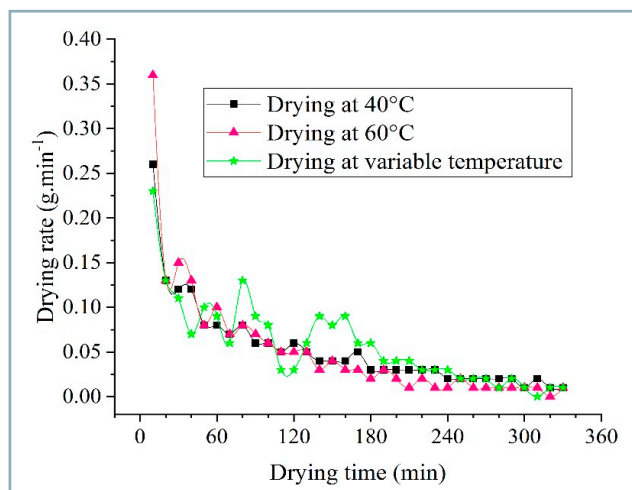


Fig. 6 Drying rate vs. time for drying under airflow at uniform and varying temperatures

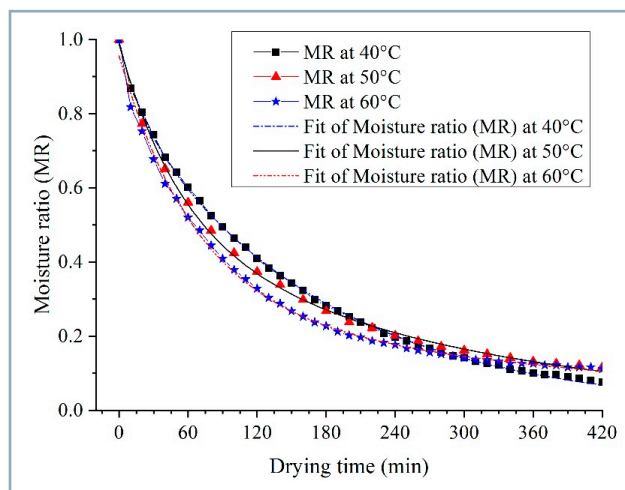


Fig. 7 Moisture content ratio during drying at uniform temperature and fitted model

Moisture content ratio obtained for samples submitted to a 60 °C airflow in 270 min was identical to moisture content obtained in 190 min at varying temperature airflow.

The analytical solution deduced previously considered several assumptions, which cannot be met in agricultural product drying.

Therefore, Ruhanian and Movagharnejad (2016) suggest semi-empirical solutions, five of which are used mostly in forced convection drying or other form of drying, but, to the authors' knowledge, have not been used in natural convection drying (Table 1).

Table 1 Mathematical expressions used to describe thin-layer drying kinetics

| Model name | Mathematical formulation |
|---------------------|--------------------------------------|
| Newton | $MR = \exp(-kt)$ |
| Henderson and Pabis | $MR = a \exp(-kt)$ |
| Logarithmic | $MR = a \exp(-kt) + c$ |
| Two term model | $MR = a \exp(-k_1t) + b \exp(-k_2t)$ |
| Page | $MR = \exp(-kt^n)$ |

Fig. 6 shows the deduced drying rates. It was observed that the process went steadily in decrease for uniform temperatures. On the other hand, for varying temperature, the drying rate seemed to jump at every increase in

temperature. This explains why there is a rapid decrease in moisture content (Fig. 5).

According to Madamb et al. (1994) and Ortiz-García-Carrasco et al. (2015), shrinking of agricultural products occurs when they are submitted to high temperatures drying process. High temperature tends to squeeze samples during shrinking. The pressure is mostly exercised on the outside of the product and closes the pores, not allowing the fluid to evaporate. This results in the reduced water effective diffusivity, implying that some residual moisture might have been preserved in the product dried at high temperature. On the contrary, product dried at low temperature keeps on drying as long as the outside air absorbs the extracted water (Fig. 4).

The experimental drying data were used to find out the most suitable model among the five different models proposed by Ruhanian and Movagharnejad (2016).

The most suitable fitness of the empirical model to the experimental data is gauged through the coefficient of determination (R^2) and the reduced chi-square (χ^2), which should be the highest coefficient of determination (R^2) and the lowest reduced chi-square (χ^2) (Table 2).

Accordingly, the two-term model, for which different constant values are generated, presents the highest coefficient of determination and the lowest reduced chi-square (Table 3, Fig. 7).

Table 2 Statistical results obtained for thin layer drying models for garlic slices under natural convection at different temperatures

| Model | T = 40 °C | | T = 50 °C | | T = 60 °C | |
|---------------------|-----------------|----------------|-----------------|----------------|-----------------|----------------|
| | χ^2 | R^2 | χ^2 | R^2 | χ^2 | R^2 |
| Newton | 9.62E-04 | 0.98351 | 0.00313 | 0.94463 | 0.00395 | 0.91622 |
| Henderson and Pabis | 3.19E-04 | 0.99453 | 0.00189 | 0.96657 | 0.00208 | 0.95591 |
| Logarithmic | 1.55E-04 | 0.99734 | 2.83E-04 | 0.99499 | 1.82E-04 | 0.99615 |
| Two-term | 2.63E-05 | 0.99958 | 8.57E-05 | 0.99849 | 1.24E-04 | 0.99738 |
| Page | 3.65E-05 | 0.99924 | 9.08E-05 | 0.99745 | 2.64E-04 | 0.99261 |

Table 3 Constants and coefficients for the best-fitted model (two-term model)

| Temperature | <i>a</i> | <i>k</i> ₁ | <i>b</i> | <i>k</i> ₂ | χ ² | R ² |
|-------------|----------|-----------------------|----------|-----------------------|----------------|----------------|
| T = 40 | 0.84535 | 0.00599157 | 0.14864 | 0.05346113 | 2.63E-05 | 0.99955 |
| T = 50 | 0.7988 | 0.01092964 | 0.16866 | 0.00084564 | 8.57E-05 | 0.99849 |
| T = 60 | 0.81 | 0.01228058 | 0.136412 | 0.00054955 | 1.24E-04 | 0.99738 |

Effective diffusivity coefficient determination

Adopting the slope method (Madamb et al., 1996; Caccavale et al., 2016), the curve of ln(MR) versus drying time generates the effective diffusivity coefficient through the fitted linear relation to these curves.

$$\ln(MR) = \ln\left(\frac{8}{\pi^2}\right) - \frac{D_{eff}\pi^2}{4l^2}t \quad (10)$$

So from the plot of ln(MR), we get:

$$D_{eff} = \frac{Slope \cdot 4l^2}{\pi^2} \quad (11)$$

A close look at Figs. 4 and 6 shows that nearly 75% of the moisture is extracted during the first falling drying rate period and the remaining moisture is extracted during the second falling drying rate period. In order to generate the fitting function, we will consider the process taking place following the two periods. For each, we deduced an effective diffusivity coefficient.

By adopting the aforementioned method, the effective diffusivity coefficients for each temperature were obtained as given in Table 4.

The effective diffusivity coefficient increased with the increase in temperature and consequent slight increase in airflow velocity even though it never reached 1 m·s⁻¹. On the other hand, in the second falling drying rate period, the

effective diffusivity coefficient decreased with increasing temperature (Table 5).

Fig. 4 indicates that, at 40 °C, the drying process continued beyond the point where it has almost stopped for 60 °C.

Therefore, the decrease in effective diffusivity might be the consequence of pore restriction at the periphery of samples during the second falling drying rate period.

To minimize the effect of shrinking, samples were dried under hot air at increasing temperature. During the first period of one hour, the temperature was fixed at 40 °C, during the second period of one hour, the temperature was fixed at 50 °C, and during the remaining time of drying, the temperature was fixed at 60 °C (Fig. 5). During this process, the effective diffusivity kept on increasing with every increase in temperature (Table 6).

The effective diffusivity coefficient value obtained during each period nearly corresponds to the one obtained during the first falling drying rate period of the corresponding uniform temperature.

Therefore, the shrinking, which occurred when the temperature was ramped up, did not have the same impact when the temperature was increased during the same process. Moreover, the drying time was reduced. The moisture content ratio obtained in 200 min under varying temperature was reached in 250 min when drying at 60 °C and in 300 min when drying at 50 °C (Fig. 4).

Table 4 Effective diffusivity coefficients at different temperatures during the first falling drying rate period

| Temperature | Effective diffusivity coefficient (m ² ·s ⁻¹) | R ² |
|-------------|--|----------------|
| 40 °C | 8.98211E-10 | 0.99774 |
| 50 °C | 9.46134E-10 | 0.99328 |
| 60 °C | 10.0912E-10 | 0.99742 |

Table 5 Effective diffusivity coefficients at different temperatures during the second falling drying rate period

| Temperature | Effective diffusivity coefficient (m ² ·s ⁻¹) | R ² |
|-------------|--|----------------|
| 40 °C | 4.7627E-10 | 0.99892 |
| 50 °C | 3.08954E-10 | 0.9913 |
| 60 °C | 2.99015E-10 | 0.99614 |

Table 6 Effective diffusivity coefficients during drying process at varying temperatures

| Period | Effective diffusivity | R ² |
|----------------------------|-----------------------|----------------|
| First period (T = 40 °C) | 8.9958E-10 | 0.99602 |
| Second period (T = 50 °C) | 8.78125E-10 | 0.96105 |
| Remaining time (T = 60 °C) | 10.7678E-10 | 0.99904 |

Conclusions

This study was undertaken to investigate the behaviour of thin layer garlic drying under free convection airflow. Investigating three temperatures with lower negative impact on final product quality, it came out that air velocity was relatively low. Application of increasing stepwise airflow temperature made samples dry in shorter time. This procedure implemented the first falling drying rate period behaviour for every step temperature. This finding was confirmed by the determination of the effective diffusivity coefficient generated for both uniform and stepwise increased temperatures during the first falling drying rate period. This new procedure lets the garlic dry in shorter time, resulting in lower energy consumption and making it more economically viable. This procedure can be used in modelling of solar energy systems and can contribute to shorter drying time and to get good product quality, since the operating temperatures are lower than 60 °C.

Acknowledgments

This work was supported by the Directorate General for Scientific Research and Technological Development, Algiers Algeria.

References

- AFONSO, C. – OLIVEIRA, A. 2000. Solar chimneys: simulation and experiment. In *Energy and Buildings*, vol. 32, pp. 71–79.
- AFRIYIE, J. K. – NAZHA, M. A. A. – RAJAKARUNA, H. – FORSON, F. K. 2009. Experimental investigations of a chimney dependent solar crop dryer. In *Renewable Energy*, vol. 34, pp. 217–222.
- AFRIYIE, J. K. – RAJAKARUNA, H. – NAZHA, M. A. A. – FORSON, F. K. 2011. Simulation and optimisation of the ventilation in a chimney-dependent solar crop dryer. In *Solar Energy*, vol. 85, pp. 1560–1573.
- AL-NEAMA, M. A. – FARKAS, I. 2016. Energy analysis of active solar drying system connected with photovoltaic modules. In *Energy and Environment*, pp. 187–196.
- AMIRI CHAYJAN, R. – SALARI, K. – SHADIDI, B. 2012. Modeling some drying characteristics of garlic sheets under semi fluidized and fluidized bed conditions. In *Research in Agricultural Engineering*, vol. 58, pp. 73–82.
- BABETTO, A. C. – FREIRE, F. B. – BARRAZO, M. A. S. – FREIRE, J. T. 2011. Drying of garlic slices: Kinetics and nonlinearity measures for selecting the best equilibrium moisture content equation. In *Journal of Food Engineering*, vol. 107, pp. 347–352.
- BARROZO, M. A. S. – SOUZA, A. M. – COSTA, S. M. – MURATA, V. V. 2001. Simultaneous heat and mass transfer between air and soybean seeds in a concurrent moving bed. In *International Journal of Food Science and Technology*, vol. 36, pp. 393–399.
- BOZKIR, H. – RAYAMN ERGÜN, A. – TEKGÜL, Y. – BAYSAL, T. 2019. Ultrasound as pretreatment for drying garlic slices in microwave and convective dryer. In *Food Science and Biotechnology*, vol. 28, pp. 347–354.
- CACCAVALE, P. – De BONIS, M. V. – RUOCCO, G. 2016. Conjugate heat and mass transfer in drying: a modeling review. In *Journal of Food Engineering*, vol. 176, pp. 28–35.
- CRAPISTE, G. H. – WHITAKER, S. – ROTSTEIN, E. 1988. Drying of cellular material – I. A mass transfer theory. In *Chemical Engineering Science*, vol. 43, pp. 2919–2928.
- FIGIEL, A. 2009. Drying kinetics and quality of vacuum microwave dehydrated garlic cloves and slices. In *Journal of Food Engineering*, vol. 94, pp. 98–104.
- İLTER, I. – AKYIL, S. – DEVSEREN, E. – OKUT, D. – KOÇ, M. – KAYMAK ERTEKIN, F. 2018. Microwave and hot air drying of garlic puree: drying kinetics and quality characteristics. In *Heat and Mass Transfer*, vol. 54 pp. 2101–2212.
- INCROPERA, F. P. – De WITT, D. P. 1996. *Introduction to heat transfer*. 3rd ed. New York/Chichester/Brisbane/Toronto/Singapore : John Wiley and Sons.
- MADAMB, P. S. – DRISCOLL, R. H. – BUCKLE, K. A. 1994. Shrinkage, density and porosity of garlic during drying. In *Journal of Food Engineering*, vol. 23, pp. 309–319.
- MADAMB, P. S. – DRISCOLL, R. H. – BUCKLE, K. A. 1996. The thin layer drying characteristics of garlic slices. *Journal of Food Engineering*, vol. 29, pp. 75–97.
- ONDRO, T. – HÚLAN, T. – VITÁZEK, I. 2017. Non-isothermal kinetic analysis of the dehydroxylation of kaolinite in dynamic air atmosphere. In *Acta Technologica Agriculturae*, vol. 20, no. 2, pp. 52–55.
- ORTIZ-GARCÍA-CARRASCO, B. – YAÑEZ-MOTA, E. – PACHECO-AGUIRRE, F. M. – RUIZ-ESPINOSA, H. – GARCÍA-ALVARADO, M. A. – CORTÉS-ZAVALETA, O. – RUIZ-LOPÉZ, I. I. 2015. Drying of shrinkable food products: Appraisal of deformation behavior and moisture diffusivity estimation under isotropic shrinkage. In *Journal of Food Engineering*, vol. 144, pp. 138–147.
- PEZZUTTI, A. – CRAPISTE, G. H. 1997. Sorptional equilibrium and drying characteristics of garlic. In *Journal of Food Engineering*, vol. 31, pp. 113–123.
- RUHANIAN, S. – MOVAGHARNEJAD, K. 2016. Mathematical modeling and experimental analysis of potato thin-layer drying in an infrared-convective dryer. In *Engineering in Agriculture, Environment and Food*, vol. 9, pp. 84–91.
- SACILIK, K. – UNAL, G. 2005. Dehydration characteristics of Kastamonu garlic slices. In *Biosystems Engineering*, vol. 92, pp. 207–215.
- SHARMA, G. P. – PRASAD, S. 2004. Effective moisture diffusivity of garlic cloves undergoing microwave convective drying. In *Journal of Food Engineering*, vol. 65, pp. 609–617.
- THUWAPANICHAYANAN, R. – PRACHAYAWARAKORN, S. – SOPONRONNARIT, S. 2014. Heat and moisture transport behavior and quality of chopped garlic undergoing different drying methods. In *Journal of Food Engineering*, vol. 136, pp. 34–41.
- YOUNIS, M. C. – ABDELKARIM, D. – ZEIN EL-ABDEIN, A. 2018. Kinetics and mathematical modeling of infrared thin-layer drying of garlic slices. In *Saudi Journal of Biological Sciences*, vol. 25, pp. 332–338.



Acta Technologica Agriculturae 2
Nitra, Slovaca Universitas Agriculturae Nitriae, 2020, pp. 99–104

THE UTILIZATION OF MUSHROOM WASTE SUBSTRATE IN PRODUCING VERMICOMPOST: THE DECOMPOSER CAPACITY OF *LUMBRICUS RUBELLUS*, *EISENIA FETIDA* AND *EUDRILUS EUGENIAE*

Agus Mulyadi PURNAWANTO¹, Yugi R. AHADIYAT^{2*}, Achmad IQBAL², TAMAD²

¹Universitas Muhammadiyah Purwokerto, Indonesia

²Universitas Jenderal Soedirman, Purwokerto, Indonesia

The objective of this study was to determine the capacity of *Lumbricus rubellus*, *Eisenia fetida* and *Eudrilus eugeniae* earthworms in vermicompost production utilizing mushroom waste substrate based on weight; number and weight loss of earthworms; temperature; pH; moisture content of media; and C/N ratio. The results showed that, by using 42 g of *E. eugeniae*, *E. fetida* and *L. rubellus* earthworms, there was an increase in weight of earthworms and vermicompost by more than 300% and 75%, respectively. In general, these three species of earthworms were able to produce vermicompost in compliance with quality standards, showing C/N ratio lower than 20.

Keywords: earthworms; mushroom waste substrate; vermicompost

Demand for mushrooms as a protein source is steadily increasing (Mukherjee and Nandi, 2004). Over the past 35 years, mushroom production increased 25-fold, from approx. 1 billion kg in 1978 to 27 billion kg in 2012 (Royse, 2014). Increased mushroom production results in an increase in the amount of waste substrate (Hanafi et al., 2018) – approx. 5 kg per mushroom substrate (Zisopoulos et al., 2016). The major components of mushroom waste substrate are sawdust; banana leaves; peanut shells; corn leaves and husk; sugarcane leaves; wheat straw; cotton waste; or paper waste (Jordan et al., 2008; Sendi et al., 2013), which are degraded during the process of mushroom production (Roy et al., 2015).

Mushroom waste substrate can be converted into valuable material by composting (Garg et al., 2006). This process is simple, economically valuable and safe for human health and environment as a waste management technology (Kovačić et al., 2019). Composting can be performed utilizing e.g. earthworms – this is known as vermicomposting (Suthar and Singh, 2008). Earthworms break down and degrade the waste by ingesting the organic materials, i.e. plant litter, soil organic matter and mineral soil particles (Bath et al., 2017; Vidal et al., 2019). Contents of plant nutrients, hormones, beneficial enzymes and microbes in vermicompost is higher in contrast to conventional compost (Bajal et al., 2019). However, the process of vermicomposting is very dependent on the type of substrate and species of earthworm used (Sinha, 2009; A'ali et al., 2017). Usually, mushroom waste substrate with sawdust is treated using certain species of earthworm, such as *Lumbricus rubellus*, *Lumbricus terrestris*, *Eisenia fetida*, *Eisenia andrei* and *Eudrilus eugeniae* (Tajbakhsh et al., 2008; Izyan et al., 2009; Suparno et al., 2013).

Numerous researchers have dealt with vermicomposting of various types of substrate using different earthworm species. Chaulagin et al. (2017) reported that a mixture of cow manure and sawdust in vermicomposting increase the weight and number of worms of *Eisenia foetida* species. Use of *Lumbricus rubellus* in composting of mushroom waste substrate mixed with goat manure resulted in vermicompost with a high content of N, P, K (Bakar et al., 2012; Jamaludin et al., 2012) and low C/N ratio (Jamaludin et al., 2012).

Addition of nutrient solution containing protein, fat, cellulose, phosphorus and microbes to mushroom waste substrate can increase both the earthworm growth and vermicompost (Tran, 2016). Based on the existing studies, earthworms are often used as decomposer in vermicomposting process (Safdar and Kor, 2014). However, the description of earthworms in production of vermicompost on the basis of the mushroom waste substrate has not yet been thoroughly investigated. Therefore, the aim is to observe the capacity of *Lumbricus rubellus*, *Eisenia fetida* and *Eudrilus eugeniae* as decomposers in vermicompost production using mushroom waste substrate.

Material and methods

The study was conducted in Karangsoka village, Kembaran subdistrict, Banyumas district, central Java, Indonesia in February to April 2018. Randomized complete block design (RCBD) with four different substrate treatments by 42 g, 84 g, 126 g, and 168 g of earthworms of *Lumbricus rubellus*, *Eisenia fetida* and *Eudrilus eugeniae* species was tested with four replications. Mushroom waste substrate was obtained

Contact address: Yugi R. Ahadiyat, Universitas Jenderal Soedirman, Laboratory of Agroecology, Department of Agrotechnology, Faculty of Agriculture, Purwokerto 53123, Indonesia, e-mail: ahadiyat.yugi@unsoed.ac.id

from oyster mushroom farmers “Agro Jamur Pabuaran” in Baturraden subdistrict, Banyumas district, Central Java, Indonesia. Mushroom waste as compost material was stored for 7 days after harvest. The earthworms with age of approx. 2.5 months were obtained from Sumbang subdistrict, Banyumas district, Central Java, Indonesia.

Preparation for cultivation of earthworms

Firstly, mushroom waste substrate for cultivating earthworms was taken from the plastic bag, crushed to a smaller size and then filtered using a sieve with a diameter of 50 mm. A total of 42 kg of mushroom waste substrate (with $\pm 70\%$ moisture content and C/N ratio of 48.54) was put into a plastic container for the purposes of vermi bed. Subsequently, the acclimatization process was carried out for each vermi bed and nitrogen nutrition of approx. 67.5 g was added to each. It was then evenly mixed and kept to meet the requirements for composting, i.e. temperature $< 30^\circ\text{C}$ (Manaf et al., 2009) and C/N ratio approx. 20–30 (FAO, 2015). After completion of acclimatization process, six 40 cm long pipes with a diameter of 3.81 cm were put in each container and 28 holes with a diameter of 5 mm each were made on sides in order to facilitate air circulation. Pipes were put vertically to the bottom of the container. In addition, thermometer was placed in the middle of the vermi bed in a vertical position below the surface (± 20 cm) and the container was kept closed.

Cultivation of earthworms

Acclimatization of earthworms was carried out after reaching the standard vermi bed conditions, i.e. temperature of 29°C ; pH of 7; and C/N ratio of 24 as a result of prior preparations. Finally, ten earthworms were put on the vermi bed surface within 48 hours for acclimatization process to observe the earthworms response. The vermi bed proved to be appropriate, as the earthworms stayed inside. Therefore, the process of cultivation could begin, and 42–168 g of earthworms of *Lumbricus rubellus*, *Eisenia fetida*, and *Eudrilus eugeniae* species were put in vermi bed, depending on the treatment.

During the vermicomposting process, the vermi bed moisture content was maintained at approx. 70% by spraying water using a hand sprayer and manual reversing was performed every two weeks in order to ensure good degradation of material at both the top and bottom. Earthworms were taken from compost after the compost C/N ratio was relatively constant by removing the vermi bed and spreading it to separate and collect the earthworms.

Analysis method

Temperature, pH and moisture content of the media were monitored using an alcohol thermometer, pH meter and hygrometer, respectively, on a daily basis from the very start of the experiment until the last day of experiment. The weight of earthworms was counted before their application to vermi bed and at the end of the experiment using a Mini Pesa digital scale TB-01 model and their number was manually counted in the same manner. Vermicompost weight was measured at the end of the experiment utilizing Excellent ACS-A Portable digital scale. Total organic carbon content was determined using partial oxidation method;

total nitrogen was determined by means of a Kjeldahl method. Total organic carbon and nitrogen contents, as well as C/N ratio, were calculated every 15 days for 75 days of the experiment.

Statistical analysis

Variance analysis ($\alpha = 0.05$) was employed to examine the differences in observed variables of different treatments. If the observed differences were significant, the results were processed using Duncan's Multiple Range Test (DMRT) with $\alpha = 0.05$.

Results and discussion

Weight and number of earthworms

The number and weight of *L. rubellus*, *E. fetida* and *E. eugeniae* earthworms in mushroom waste substrate showed significant changes at the end of composting (Table 1). The initial weight of 168 g of earthworms resulted in high weight, but low enhancement percentage. Low initial weight of 42 g of earthworms had the opposite effect (Table 1). The biggest earthworm population at the end of composting was obtained by cultivating *E. fetida* – it increased by 73.26%. The highest enhancement percentage was obtained by *E. eugeniae* – initial population of 42 earthworms increased by 345.82%, ending with 187 earthworms.

Higher earthworm population in culture media resulted in the lower earthworm weight percentage. Safdar and Kor (2014) reported that, under ideal conditions, earthworms are able to consume the amount exceeding their body weight each day; however, they commonly consume the amount equal to approx. half of their body weight per day. However, the amount of food supplied to earthworms must be controlled to avoid worm mortality (Vodounnou et al., 2016; Musyoka et al., 2019). Getachew et al. (2018) reported that 50 kg of earthworms is able to consume 375 kg of feed within one month during the breeding process. Therefore, food must be added before it is completely consumed during the earthworm cultivation process in order to gain the maximum population growth. If no food is added to the container, earthworm population growth is inhibited.

Weight of vermicompost

The vermicompost weight produced in each treatment ranged from 27.8 to 30.6 g with weight loss percentage of 27.2–33.8% (Table 2). Vermicompost production is very dependent on the earthworm species used (Kostecka et al., 2018) and the type of substrate used for feeding of earthworms (Saikrithika et al., 2015). *E. eugeniae*, *E. fetida* and *L. rubellus* earthworm species are epigeic or litter dweller group earthworms and play a critical role in the decomposition of organic matter into vermicompost (Gomez-Brandon et al., 2012; Chatelain and Mathieu, 2017; Ramesh et al., 2018). Therefore, the earthworms will produce the same amount of vermicompost in weight as is the original weight of mushroom waste substrate in the pre-treatment. The increasing earthworm population resulted in reduction of the vermicompost weight due to the fact that the substrate was not only converted into vermicompost but

Table 1 Weight and number of *E. eugeniae*, *E. fetida* and *L. rubellus* earthworms in vermicomposting

| Treatment | Weight of earthworms | | | Number of earthworms | | |
|--------------------------|----------------------|----------------|--------------|----------------------|------------|--------------|
| | at initial (g) | at the end (g) | increase (%) | at initial | at the end | increase (%) |
| 42 g <i>E. eugeniae</i> | 42 | 183.5 a | 336.90 e | 42 | 187 a | 345.82 f |
| 84 g <i>E. eugeniae</i> | 84 | 269.9 b | 221.28 bcd | 84 | 275 cd | 227.84 d |
| 126 g <i>E. eugeniae</i> | 126 | 362.0 c | 187.30 abc | 126 | 369 f | 193.16 bc |
| 168 g <i>E. eugeniae</i> | 168 | 457.8 d | 172.47 a | 168 | 467 gh | 178.03bc |
| 42 g <i>E. fetida</i> | 42 | 184.3 a | 338.69 e | 88 | 236 bc | 168.43bc |
| 84 g <i>E. fetida</i> | 84 | 272.8 b | 224.70 cd | 175 | 350 ef | 99.82 a |
| 126 g <i>E. fetida</i> | 126 | 368.5 c | 192.46 abcd | 263 | 472 h | 79.63 a |
| 168 g <i>E. fetida</i> | 168 | 473.0 d | 181.55 ab | 350 | 606 j | 73.26 a |
| 42 g <i>L. rubellus</i> | 42 | 187.5 a | 346.43 e | 53 | 213 ab | 302.02 e |
| 84 g <i>L. rubellus</i> | 84 | 277.8 b | 230.65 d | 105 | 316 de | 200.60 cd |
| 126 g <i>L. rubellus</i> | 126 | 377.5 c | 199.60 abcd | 158 | 429 g | 171.50 bc |
| 168 g <i>L. rubellus</i> | 168 | 490.0 d | 191.64 abcd | 210 | 557 i | 165.13 b |

In the same column, the number followed by the same letter indicates no significant difference according to the DMRT at $\alpha = 0.05$ and each letter indicates the enhancement: the first letter of the alphabet suggests the smaller increase and the last of the alphabet letter suggests the greater increase

also served for the growth and development of earthworms. In order to multiply the vermicompost production, substrate addition must be performed in line with the earthworm population increase. High rate of earthworm growth and reproduction must be supported by optimal feeding (Siddique et al., 2005; Klok, 2007; Chauhan and Singh, 2013).

During composting, the temperature, pH and moisture in vermi bed were in ranges 27–28 °C, 6.4–6.7 and 68.5–70.3%, respectively (Table 3). It was a suitable living environment for observed earthworms. The favourable conditions are: 15–30 °C for temperature (Manaf et al., 2009); 4.3–8.3 for pH (Singh et al., 2005); and 59.5–71.9% for moisture content (Parvaresh et al., 2004; Palsania et al., 2008).

Total organic carbon (TOC)

Different initial weight of earthworms used showed the same pattern of decrease in TOC by approx. 40–44% in all treatments (Fig. 1). Gougoulas et al. (2014) reported that certain amount of carbon is used as a microbial energy source in the decomposition process and is released in the form of CO₂, while the rest of it is assimilated to a microbial biomass form. Decreasing level of TOC is caused by the activity of respiration and assimilation of microorganisms and earthworms that can convert organic C into CO₂ (Suthar and Gairola, 2014). The addition of *E. eugeniae* showed that decrease in TOC was more rapid in contrast to treatments with *L. rubellus* and *E. fetida*; this is due to the fact that

Table 2 Development of mushroom waste substrate weight treated using *E. eugeniae*, *E. fetida* and *L. rubellus* earthworms

| Treatment | Weight of vermicompost (× 1,000 g) | Loss of weight (%) |
|--------------------------|------------------------------------|--------------------|
| 42 g <i>E. eugeniae</i> | 30.6 a | 27.2 a |
| 84 g <i>E. eugeniae</i> | 29.7 a | 29.2 a |
| 126 g <i>E. eugeniae</i> | 28.9 a | 31.1 a |
| 168 g <i>E. eugeniae</i> | 28.3 a | 32.5 a |
| 42 g <i>E. fetida</i> | 29.3 a | 30.2 a |
| 84 g <i>E. fetida</i> | 28.9 a | 31.3 a |
| 126 g <i>E. fetida</i> | 28.3 a | 32.5 a |
| 168 g <i>E. fetida</i> | 27.8 a | 33.8 a |
| 42 g <i>L. rubellus</i> | 29.2 a | 30.5 a |
| 84 g <i>L. rubellus</i> | 28.9 a | 31.3 a |
| 126 g <i>L. rubellus</i> | 27.9 a | 33.5 a |
| 168 g <i>L. rubellus</i> | 28.1 a | 33.1 a |

In the same column, the number followed by the same letter indicates no significant difference in weight reduction according to the DMRT at $\alpha = 0.05$. The initial weight of mushroom waste substrate was 42 kg

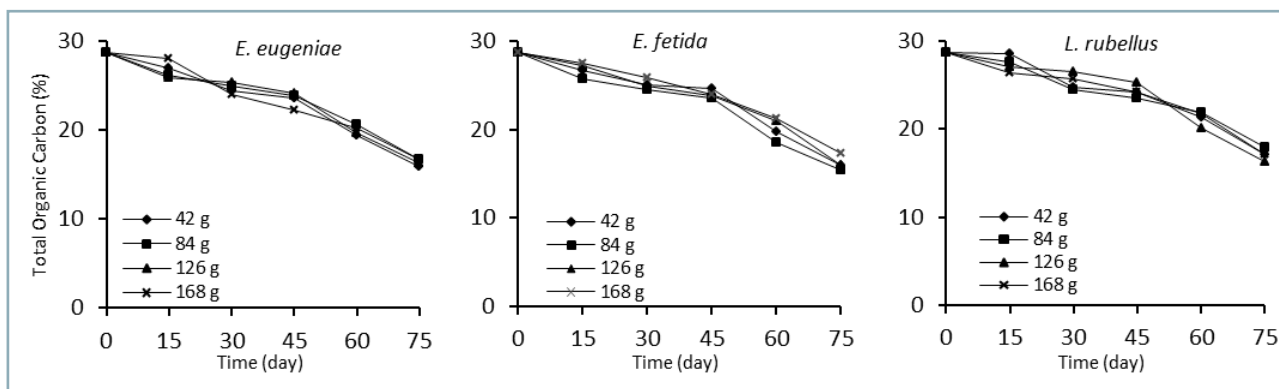


Fig. 1 Total organic carbon in substrates treated using *E. eugeniae*, *E. fetida* and *L. rubellus* earthworms

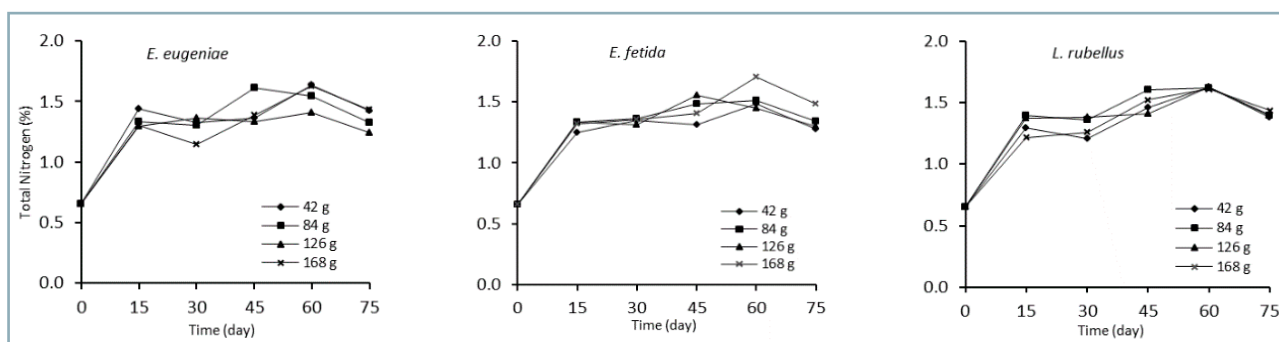


Fig. 2 Total nitrogen in substrate treated using *E. eugeniae*, *E. fetida* and *L. rubellus* earthworms

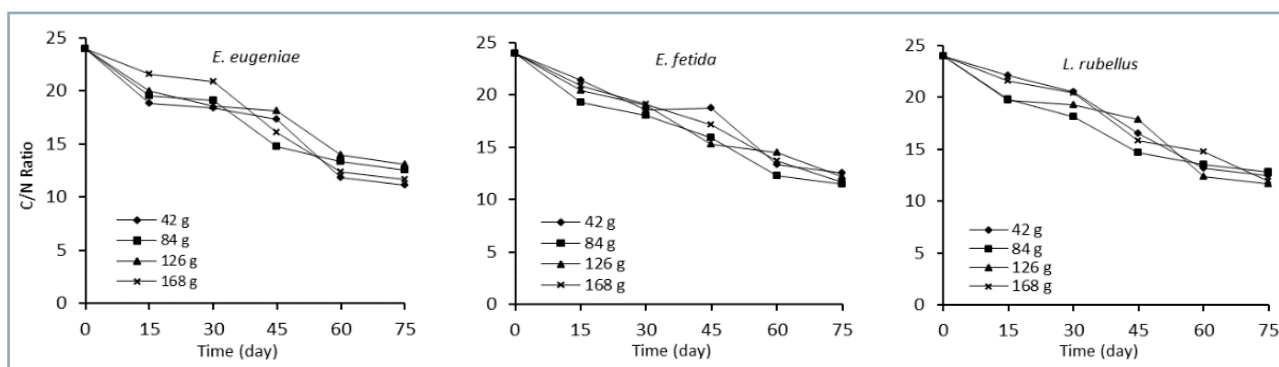


Fig. 3 C/N ratio in vermicomposts treated using *E. eugeniae*, *E. fetida* and *L. rubellus* earthworms

E. eugeniae earthworm species is larger, and grows and multiplies more rapidly. Earthworm species with larger body are able to decompose larger amounts of organic matter in vermicomposting (Prabha et al., 2015).

Total nitrogen (TN)

The TN content in vermicompost showed increasing tendency with fluctuations (Fig. 2). The fluctuation of TN content occurs due to varying activity of microorganisms and earthworms. The increase in TN can be in form of mucus, enzymes, or excretion of nitrogen-containing material; on the contrary, reduction in TN occurs due to consumption of microorganisms and earthworms themselves (Lim et al., 2012). In addition, earthworm mortality can also result in increase in TN, because the earthworm body consists of

45–65% of protein, which is a source of organic nitrogen (Lourdumary and Uma, 2012).

C/N ratio

The C/N ratio is one of vermicompost maturity indicator. The C/N ratio under 20 indicates that the compost is mature. If the C/N ratio is equal to or lower than 15, it indicates that compost is of a high agronomic value (Suthar, 2009). The C/N ratio of all treated specimens decreased at the end of composting due to decrements in TOC content and increments in TN content. The highest reduction of C/N ratio occurred in treatment using *E. fetida* – 11.97; the final C/N ratio in composts treated using *E. eugeniae* and *L. rubellus* was 12.13 and 12.22, respectively.

Vermicomposts produced by treating the substrates by means of *E. eugeniae*, *E. fetida* and *L. rubellus* earthworm

Table 3 Temperature, pH and humidity of media during vermicomposting of mushroom waste substrate treated using *E. eugeniae*, *E. fetida* and *L. rubellus* earthworms

| Treatment | Temperature (°C) | pH | Humidity (%) |
|--------------------------|------------------|-----|--------------|
| 42 g <i>E. eugeniae</i> | 27 | 6.5 | 68.7 |
| 84 g <i>E. eugeniae</i> | 27 | 6.5 | 68.5 |
| 126 g <i>E. eugeniae</i> | 27 | 6.5 | 69.3 |
| 168 g <i>E. eugeniae</i> | 28 | 6.5 | 68.1 |
| 42 g <i>E. fetida</i> | 27 | 6.4 | 70.0 |
| 84 g <i>E. fetida</i> | 28 | 6.7 | 70.1 |
| 126 g <i>E. fetida</i> | 28 | 6.7 | 70.3 |
| 168 g <i>E. fetida</i> | 27 | 6.4 | 70.2 |
| 42 g <i>L. rubellus</i> | 28 | 6.5 | 69.2 |
| 84 g <i>L. rubellus</i> | 27 | 6.5 | 69.5 |
| 126 g <i>L. rubellus</i> | 27 | 6.5 | 68.7 |
| 168 g <i>L. rubellus</i> | 27 | 6.4 | 69.0 |

species were in compliance with mature or stable compost criteria given by the FAO (2015), indicating that observed earthworm species have the potential to serve as decomposers in the production of mushroom waste substrate vermicompost.

Conclusion

The process of mushroom waste substrate vermicomposting using *E. eugeniae*, *E. fetida* and *L. rubellus* showed that earthworm species *E. eugeniae*, *E. fetida* and *L. rubellus* with original weight of 42 g were able to increase their weight percentage by 336.90, 338.69 and 346.4, respectively, in the observed substrate. The *E. eugeniae* earthworm population showed the highest increase – by 345.82%. Considering the criteria for vermicompost quality standards determined by the FAO, all the three earthworm species were able to produce appropriate vermicompost with *E. fetida* showing the best results (11.97).

Acknowledgement

The author would like to thank the Directorate General of Research and Development, Ministry of Research, Technology and Higher Education for the doctoral research grant to support this research.

References

A'ALI, R. – JAFARPOUR, M. – KAZEMI, E. – PESSARAKLI, M. 2017. Effects of raw materials on vermicompost qualities. In *Journal of Plant Nutrition*, vol. 40, no. 11, pp. 1635–1643.

BAJAL, S. – SUBEDI, S. – BARAL, S. 2019. Utilization of agricultural wastes as substrates for vermicomposting. In *IOSR Journal of Agriculture and Veterinary Science (IOSR-JAVS)*, vol. 12, no. 8, pp. 79–84.

BAKAR, A. A. – MAHMOOD, N. Z. – ABDULLAH, N. – TAHA, R. M. 2012. Bioconversion of biomass residue from the cultivation of pea sprouts on spent *Pleurotus sajor-caju* compost employing *Lumbricus rubellus*. In *Maejo International Journal of Science and Technology*, vol. 6, no. 3, pp. 461–469.

BATH, S. A. – SINGH, J. – VIG, A. P. 2017. Earthworms as organic waste managers and biofertilizer producers. In *Waste and Biomass Valorization*, vol. 9, no. 7, pp. 1073–1086.

CHATELAIN, M. – MATHIEU, J. 2017. How good are epigeic earthworms at dispersing? An investigation to compare epigeic to endogeic and anecic groups. In *Soil Biology and Biochemistry*, vol. 111, pp. 115–123.

CHAUHAN, H. K. – SINGH, K. 2013. Effect of tertiary combinations of animal dung with agrowastes on the growth and development of earthworm *Eisenia fetida* during organic waste management. In *International Journal of Recycling of Organic Waste in Agriculture*, vol. 2, no. 11, 7 pp.

CHAULAGIN, A. – MAHARJAN, B. – PATHAK, R. – PIYA, S. – CHIMORAYA, S. – SHRESTA, I. – GAUCHAN, D. P. – LAMICHHANE, J. 2017. Effect of feeding materials on yield, quality of vermicompost, multiplication and reproduction of *Eisenia foetida*. In *Journal of Science, Engineering and Technology*, vol. 13, no. 2, pp. 15–25.

FOOD AND AGRICULTURE ORGANIZATION. 2015. *Farmer's Compost Handbook: Experiences in Latin America*. Santiago: Food and Agriculture Organization of the United Nations Regional Office for Latin America and the Caribbean.

GARG, P. – GUPTA, A. – SATYA, S. 2006. Vermicomposting of different types of waste using *Eisenia fetida*: A comparative study. In *Bioresource Technology*, vol. 97, no. 3, pp. 391–395.

GETACHEW, Z. – ADISU, T. – ABEBLE, L. – ANBESSA, B. 2018. Vermicompost potential of common earthworm (*Eudrilus eugeniae*) and red wiggler (*Eisenia fetida*) earthworm on the decomposition of various organic wastes. In *International Journal of Plant and Soil Science*, vol. 24, no. 3, pp. 1–13.

GOMEZ-BRANDON, M. – LORES, M. – DOMINGUEZ, J. 2012. Species-specific effects of epigeic earthworms on microbial community structure during first stages of decomposition of organic matter. In *PLoS ONE*, vol. 7, no. 2, pp. e31895.

GOUGOULIAS, C. – CLARK, J. M. – SHAW, L. J. 2014. The role of soil microbes in the global carbon cycle: tracking the below-ground microbial processing of plant-derived carbon for manipulating carbon dynamics in agricultural systems. In *Journal of the Science of Food and Agriculture*, vol. 94, no. 12, pp. 2362–2371.

HANAFI, F. H. M. – REZANIA, S. – MAT TAIB, S. – MD DIN, M. F. – YAMAUCHI, M. – SAKAMOTO, M. – HARA, H. – PARK, J. – EBRAHIMI, S. S. 2018. Environmentally sustainable applications of agro-based

- spent mushroom substrate (SMS): an overview. In *Journal of Material Cycles and Waste Management*, vol. 20, no. 3, pp. 1383–1396.
- IZYAN, N. N. – JAMALUDIN, A. A. – MAHMOOD, N. Z. 2009. Potential of spent mushroom substrate in vermicomposting. In *Dynamic Soil, Dynamic Plant*, vol. 3, no. 2, pp. 87–90.
- JAMALUDIN, A. A. – MAMOOD, N. Z. – ABDULLAH, N. 2012. Waste recycling: Feasibility of saw dust based spent mushroom substrate and goat manure in vermicomposting. In *Sains Malaysiana*, vol. 41, no. 11, pp. 1445–1450.
- JORDAN, S. N. – MULLEN, G. J. – MURPHY, M. C. 2008. Composition variability of spent mushroom compost in Ireland. In *Bioresource Technology*, vol. 99, no. 2, pp. 411–418.
- KLOK, C. 2007. Effects of earthworm density on growth, development, and reproduction in *Lumbricus rubellus* (Hoffm) and possible consequences for the intrinsic rate of population increase. In *Soil Biology and Biochemistry*, vol. 39, pp. 2401–2407.
- KOSTECKA, J. – GARCZYNSKA, M. – PODOLAK, A. – PACZKA, G. – KANIUCZAK, J. 2018. Kitchen organic waste as material for vermiculture and source of nutrients for plants. In *Journal of Ecological Engineering*, vol. 19, no. 6, pp. 267–274.
- KOVAČIĆ, D. – KRALIK, D. – JOVIČIĆ, D. – SPAJIĆ, R. 2019. An assessment of anaerobic thermophilic co-digestion of dairy cattle manure and separated tomato greenhouse waste in lab-scale reactors. In *Acta Technologica Agriculturae*, vol. 22, no. 2, pp. 38–42.
- LIM, S. I. – WU, T. Y. – SIM, E. Y. S. – LIM, P. N. – CLARKE, C. 2012. Biotransformation of rice husk into organic fertilizer through vermicomposting. In *Ecological Engineering*, vol. 41, pp. 60–64.
- LOURDUMARY, A. J. B. – UMA, K. 2012. Nutritional evaluation of earthworm powder (*Lampito mauritii*). In *Journal of Applied Pharmaceutical Science*, vol. 3, no. 3, pp. 82–84.
- MANAF, L. A. – JUSOH, M. L. C. – ISMAIL, M. K. Y. T. H. T. – HARUN, R. – JUAHIR, H. 2009. Influences of bedding material in vermicomposting process. In *International Journal of Biology*, vol. 1, no. 1, pp. 81–91.
- MUKHERJEE, R. – NANDI, B. 2004. Improvement of in vitro digestibility through biological treatment of water hyacinth biomass by two *Pleurotus* species. In *International Biodeterioration and Biodegradation*, vol. 53, pp. 7–12.
- MUSYOKA, S. N. – LITI, D. M. – OGELLO, E. – WAIDBACHER, H. 2019. Utilization of the earthworm, *Eisenia fetida* (Savigny, 1826) as an alternative protein source in fish feeds processing: A review. In *Aquaculture Research*, vol. 50, pp. 2301–2315.
- PALSANIA, J. – SHARMA, R. – SRIVASTANA, J. K. – SHARMA, D. 2008. Effect of moisture content variation over kinetic reaction rate during vermicomposting process. In *Applied Ecology and Environmental Research*, vol. 6, no. 2, pp. 49–61.
- PARVARESH, A. – MOVAHEDIAN, H. – HAMIDIAN, L. 2004. Vermistabilization of municipal wastewater sludge with *Eisenia fetida*. In *Iranian Journal of Environmental Health Science and Engineering*, vol. 1, no. 2, pp. 43–50.
- PRABHA, M. L. – NAGALAKSHMI, N. – PRIYA, M. S. 2015. Analysis of nutrient contents in vermicompost. In *European Journal of Molecular Biology and Biochemistry*, vol. 2, no. 1, pp. 42–48.
- RAMESH, R. – SELVARAJ, Y. – KANNAIYAN, S. 2018. Influence of substrate size on vermicomposting of pre-processed mixed vegetable waste. In *International Journal of Advances in Science Engineering and Technology*, vol. 6, no. 2, pp. 5–10.
- ROY, S. – BARMAN, S. – CHAKRABORTY, U. – CHAKRABORTY, B. 2015. Evaluation of spent mushroom substrate as biofertilizer for growth improvement of *Capsicum annum* L. In *Journal of Applied Biology and Biotechnology*, vol. 3, no. 3, pp. 22–27.
- ROYSE, D. J. 2014. A Global perspective on the high five: *Agaricus*, *Pleurotus*, *Lentinula*, *Auricularia* and *Flammulina*. In *Proceedings of the 8th International Conference on Mushroom Biology and Mushroom Products (ICMBMP8)*.
- SAFDAR, A. H. A. – KOR, N. M. 2014. Vermicompost and vermiculture: structure, benefits and usage. In *International Journal of Advanced Biological and Biomedical Research*, vol. 2, no. 3, pp. 775–782.
- SAIKRITHIKA, S. – SANTHIYA, K. R. – GAYATHRI, V. K. 2015. Effects of different substrates on vermicomposting using *Eudrilus eugeniae* on the growth of *Vinca rosea*. In *International Journal of Scientific and Research Publications*, vol. 5, no. 9, pp. 1–11.
- SENDI, H. – MOHAMED, M.T.M. – ANWAR, M. P. – SAUD, H. M. 2013. Spent mushroom waste as a media replacement for peat moss in Kai-lan (*Brassica oleracea* var. *alboglabra*) production. In *The Scientific World Journal*, pp. 1–8.
- SIDDIQUE, J. – KAN, A. A. – HUSSAIN, I. – AKHTER, S. 2005. Growth and reproduction of earthworm (*Eisenia fetida*) in different organic media. In *Pakistan Journal of Zoology*, vol. 37, no. 3, pp. 211–214.
- SINGH, N. B. – KHARE, A. K. – BHARGAVA, D. S. – BHATTACHARYA, S. 2005. Effect of initial substrate pH on vermicomposting using *Perionyx excavatus*. In *Applied Ecology and Environmental Research*, vol. 4, no. 1, pp. 85–97.
- SINHA, R. K. 2009. Earthworms vermicompost: A powerful crop nutrient over the conventional compost and protective soil conditioner against the destructive chemical fertilizers for food safety and security. In *Journal of Agricultural and Environment Science*, vol. 5, pp. 14–55.
- SUPARNO – PRASETYA, B. – TALKAH, A. – SOEMARNO. 2013. The Study of vermicomposting optimization of organic waste. In *International Journal of Advances in Engineering and Technology*, vol. 6, no. 4, pp. 1505–1511.
- SUTHAR, S. 2009. Vermicomposting of vegetable-market solid waste using *Eisenia fetida*: Impact of bulking material on earthworm growth and decomposition rate. In *Ecological Engineering*, vol. 35, pp. 914–920.
- SUTHAR, S. – GAIROLA, S. 2014. Nutrient recovery from urban forest leaf litter waste solids using *Eisenia fetida*. In *Ecological Engineering*, vol. 71, pp. 660–666.
- SUTHAR, S. – SINGH, S. 2008. Vermicomposting of domestic waste by using two epigeic earthworms (*Perionyx excavatus* and *Perionyx sansibaricus*). In *Journal of Environment Science and Technology*, vol. 5, no. 1, pp. 99–106.
- TAJBAKHSH, J. – ABDOLI, M. A. – GOLTAPPEH, E. M. – ALAHDADI, I. – MALAKOUTI, M. J. 2008. Recycling of spent mushroom compost using earthworms *Eisenia fetida* and *Eisenia andrei*. In *Environmentalist*, vol. 28, no. 4, pp. 476–482.
- TRAN, H. 2016. Vermicomposting of spent mushroom compost using *Perionyx excavatus* and artificial nutrient compound. In *International Journal of Environmental and Agriculture Research*, vol. 2, no. 6, pp. 101–109.
- VIDAL, A. – WATTEAU, F. – REMUSAT, L. – MUELLER, C. W. – NGUYEN TU, T. T. – BUEGGER, F. – DERENNE, S. – QUENEA, K. 2019. Earthworm cast formation and development: A shift from plant litter to mineral associated organic matter. In *Frontiers in Environmental Science*, vol. 7, no. 55, pp. 1–15.
- VODOUNNOU, D. S. J. V. – KPOGUE, D. N. S. – TOSSAVI, C. E. – MENNSAH, G. A. – FIOGBE, E. D. 2016. Effect of animal waste and vegetable compost on production and growth of earthworm (*Eisenia fetida*) during vermiculture. In *International Journal of Recycling of Organic Waste in Agriculture*, vol. 5, pp. 87–92.
- ZISOPOULOS, F. K. – ramirez, H. A. B. – van der GOOT, A. J. – BOOM, R. M. 2016. A resource efficiency assessment of the industrial mushroom production chain: The influence of data variability. In *Journal of Cleaner Production*, vol. 126, pp. 394–408.

